# High Pressure Raman Scattering studies on Mid-chain Hydrocarbons, Perfluorocarbons and Temperature dependent Brillouin Scattering studies on $ABO_4$ Tungstates and $AgGaS_2$

A Thesis
Submitted for the Degree of
***Doctor of Philosophy***

By

**G. Kavitha**

Light Scattering Laboratory

Chemistry and Physics of Materials Unit

Jawaharlal Nehru Centre for Advanced Scientific Research

Bangalore – 560 064, India.

February 2008.

# Declaration

I hereby declare that the thesis entitled "***High Pressure Raman Scattering studies on Mid-chain Hydrocarbons, Perfluorocarbons and Temperature dependent Brillouin Scattering studies on $ABO_4$ Tungstates and $AgGaS_2$***" is an authentic record of research work carried out by me under the supervision of Prof. Chandrabhas Narayana at Light Scattering Laboratory, Chemistry and Physics of Materials Unit, Jawaharlal Nehru Centre for Advanced Scientific Research, Bangalore, India. The thesis has not previously formed the basis for the award of any degree, diploma, associateship or fellowship.

G. Kavitha

**Jawaharlal Nehru Centre for Advanced Scientific Research**
**Jakkur, Bangalore 560064**
**India**

Chandrabhas Narayana,
Associate Professor,
Phone: 91 80 2208 2810,
Fax : 91 80 2208 2766,
Email : cbhas@jncasr.ac.in

## Certificate

February, 13th 2008

Certified that the work described in this thesis embodied **"*High Pressure Raman Scattering studies on Mid-chain Hydrocarbons, Perfluorocarbons and Temperature dependent Brillouin Scattering studies on $ABO_4$ Tungstates and $AgGaS_2$*"** has been carried out by Ms. G. Kavitha under my supervision at the Light Scattering Laboratory, Chemistry and Physics of Materials Unit, Jawaharlal Nehru Centre for Advanced Scientific Research, Bangalore, India.

Prof. Chandrabhas Narayana

# Acknowledgements

Many people walk in and out of our lives each day and most of them touch our lives one way or other. This is perhaps one of the occasions when I can express gratitude to all of them, who, over the years, have directly or indirectly been a part of my growth both as a researcher and as a composed person.

First of all I had been very lucky to work under excellent guidance of Prof. Chandrabhas Narayana. At this time, I would like to thank him for giving me freedom in workplace, the support, abundant scientific inputs during discussions, constructive criticism helped me to become a more composed scientist. Due to his excellent guidance and advice, I have emerged as a better candidate personally and professionally.

I wish to express my warm and sincere gratitude to Prof. C.N.R. Rao, FRS, for being a constant source of inspiration. His never subsiding enthusiasm and high spirit was a continuous source of motivation to carry out high quality science.

I would like to acknowledge my thanks and regards to Prof. Ajay. K. Sood, Physics Department, Indian Institute Science for allowing me to use his lab for literature survey. He is also one of the person to inspire me towards science.

I would like to acknowledge and thank Prof. Jayaraman, Bell Laboratory, New Jerssey. for providing good quality single crystal for the experiment.

I am very much thankful to Prof. R. K. Sharma, Solid State Physics Laboratory, New Delhi. for Laue diffraction measurement and fruitful discussions.

I would express my sincere thanks to Prof. Balasubramaniam Sundaram and Dr. Krishnan, for providing me Molecular Dynamic Simulations and Knowledge.

I would like to take an opportunity to thank my collaborators Vivek Chand, Dr. Govinda raj (JNCASR), Mandal, Prof. Sreenivasa Natarajan (SSCU, IISc), T. Ahmed, Prof. A. K. Ganguly, IIT Delhi, for encouraging discussions.

I have also been very fortunate to attend excellent courses here at JNCASR. I would like to thank all the CPMU and TSU faculties for excellent fundamental lecture during course work.

I would like to express my immense pleasure to thank my lab mates. Dr. Murugavel, Dr. Motin Sheik, Dr. Nashiour Rehman, Gopal, Pavan, Partha, Deepika, Sonia, vibha, shruthi, Chandra sekar for constructive scientific and non-scientific interaction and an enjoyable stay during the course of my Ph.D.

Very special thanks to my Ph.D batchmates, BSc, MSc, IISc, JNC friends for their constant encouragement and mental support throughout my academic career.

I would like to acknowledge Technical, Administrative and Academic Staffs for their help during my stay here and I would like to express my special thanks to Mr. Arockianathan who helped me in work shop for designing experimental parts.

At last but not the least, I would like to express my deep sense of gratitude to my dearest parents for their blessings and support throughout my life. No amount of words would be enough to thank my family members.

Most importantly, I must express my deepest appreciation to my husband Mohan for his encouragement, help and enthusiasm during my final stage of Ph.D.

# Synopsis

The present thesis uses two optical probes, namely, Raman and Brillouin spectroscopy to study the physical properties of material. In order to understand the systems we have used the two thermodynamic quantities, pressure and temperature. There is a lot of interest in the study of mid chain alkanes and perfluroalkanes in their condensed phase. This information is readily usable when one makes hybrid molecules out of these as well as when one tries to understand the interactions of these molecules in various environment. Tungstate with scheelite structure has been the main focus of recent spectroscopic studies at low temperature and high pressure, because of the identification of several phase transitions in these compounds. It might help to determine the factors involved in structure stability. Further the influence of cation on the crystal structure can help in modeling the effect of impurities on the physical properties. The I-III-$VI_2$ Chalcopyrite Structure compounds have quite similar physical properties as the binary II-VI analogs with the cubic (zinc blende) structure. The temperature induced changes in optical properties of these materials will be useful for designing optical devices with these compounds.

Chapter 1 describes the relevant introduction for the present work. Chapter 2 describes the designing of low cost Raman spectrometers for high pressure studies and experimental details about low temperature Brillouin spectroscopy. Chapter 3 describes the pressure induced phase transition of mid chain alkanes in the condensed phase. These alkanes undergo order-disorder transition accompanied with dampening of methyl end group. Compared to n-heptane and n-hexane, the behavior of n-pentane with pressure is different due to its small size and crystal structure. The solid-solid transition pressure is inversely proportional to the chain-length. Chapter 4 describes the observation of liquid-solid transition as well as solid-solid transitions in the condensed phase of mid-chain perfluorocarbons. Both perfluorohexane and perfluoroheptane undergoes two types of solid-solid transition 1.conformational disorder transition due to reversal of the helical pitch and 2.disorder-order transition due to all-trans conformation. Chapter 5 describes the temperature dependent structural transition of $PbWO_4$ and $BaWO_4$. The sound velocity and elastic behavior of these compounds will be useful in designing acousto-

optic devices. Chapter 6 describes the temperature induced elastic moduli behavior of $AgGaS_2$. The changes in elastic behavior have been coupled with change in refractive index of the material. Beyond particular temperature, there is a transition from semi-conductor to semi-insulator.

# Publications

1. **G. Kavitha** and Chandrabhas Narayana ***Journal of Physcial Chemistry. B***, Vol. 110, 8777, (2006).

2. **G. Kavitha** and Chandrabhas Narayana, ***Journal of Physical Chemistry B***, 111, 7003-7008 (2007).

3. **G. Kavitha** and Chandrabhas Narayana ***Journal of Physical Chemistru B,*** 111, 14130-14135, (2007).

4. **G. Kavitha**, S.R.C. Vivek, A. Govindaraj and Chandrabhas Narayana, ***Proceedings Indian Academy of Sciences (Chemical Science)*** 115, 689-694, (2003).

5. **G. Kavitha** and Chandrabhas Narayana ***Journal of Physcial chemistry B***. (submitted)

6. **G. Kavitha**, Nandhini Garg, S.M. Sharma and Chandrabhas Narayana ***Physical Review B*** (submitted)

7. **G. Kavitha** and Chandrabhas Narayana ***Physical Review B*** (submitted)

8. Mandal, **G. Kavitha**, Chandrabhas Narayana and S. Natarajan ***Journal of Solid State Chemistry*** 177, 2198-2204 (2004).

9. Tokeer Ahmad, **Gnanasundaram Kavitha**, Chandrabhas Narayana and Ashok K. Ganguli. ***Journal of Materials Research*** 20, 1415 - 1421 (2005).

10. Neena Susan John, G. U. Kulkarni, Ayan Datta, Swapan K. Pati, F. Komori, **G. Kavitha**, Chandrabhas Narayana and M. K. Sanyal ***Journal of Physical Chemistry C (Letter)*** 111, 1868-1870 (2007).

**Dedicated to**

**Appa, Amma and Mohan**

# Content

# CHAPTER - I

# Introduction

### 1.1.Raman Spectroscopy

When a monochromatic beam of light interact with solid, opaque or transparent substance the scattered energy will consist almost entirely of radiation of incident frequency (Rayleigh Scattering), but in addition certain discrete frequencies above and below that of incident beam will be scattered, which is referred to as Raman Scattering. The monochromatic radiation of frequency υ consisting of a stream of particles called photons having energy hυ, where 'h' is planck's constant. These photons can undergo 'collisions' with molecules, however it may happen that energy is exchanged between photon and molecule during such collision which are referred to as inelastic scattering.

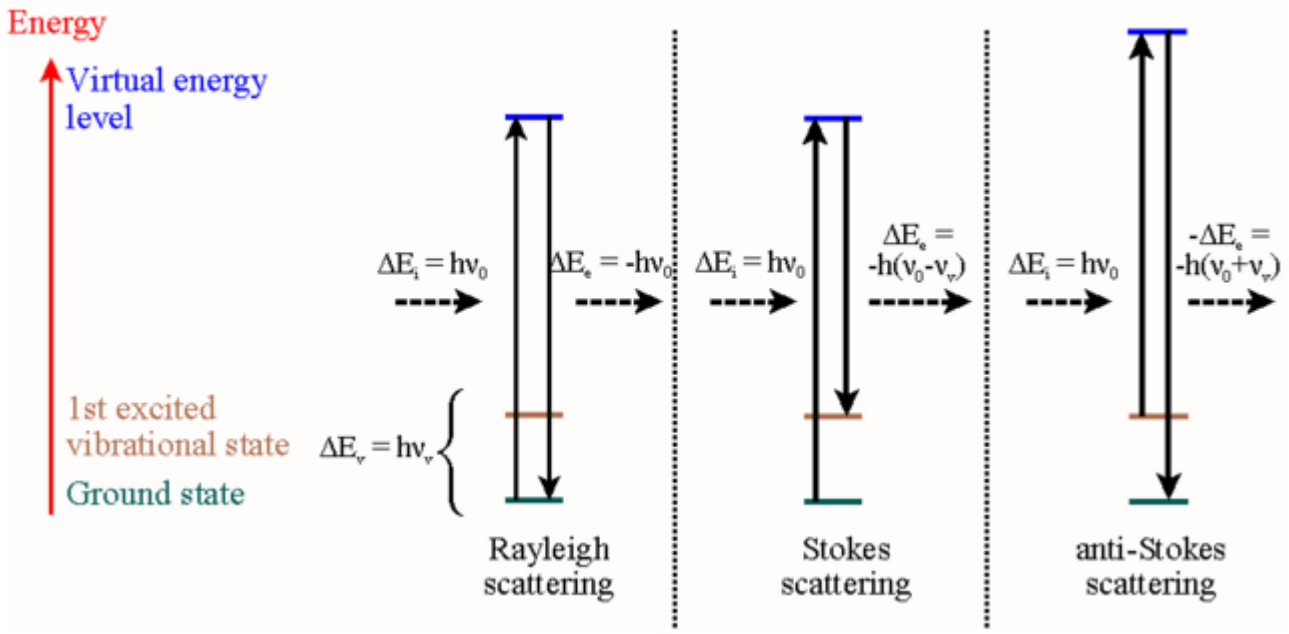


Figure 1.1 Schematic representation of Raman scattering process.

The molecule can gain or lose amounts of energy only in accordance with quantal laws. i.e, its energy change ΔE (joules) must be the difference in energy between two of its allowed states which is equivalent to the change in the vibrational energy level of the molecules. If the molecule gains energy ΔE the scattered radiation will have a frequency $\upsilon_0$-υ which is called Stokes Raman scattering and the molecule loses energy

$\Delta E$, the resultant scattered radiation will have a frequency $\upsilon_0+\upsilon$ which is anti-Stokes Raman scattering. Figure 1.1. shows the schematic representation of Raman scattering process. Since Stokes Raman scattering is due to creation of excited state, this process is generally more intense than anti-Stokes Raman scattering. Thus in Raman spectroscopy [1], the Raman spectra shows the vibrational frequency $\Delta\upsilon$ as a shift from incident frequency ($\upsilon_0$). The vibrations of the material occur depending only on the kinds of chemical bonding connecting nuclei and the space group of the crystal lattice. Group theoretical [2] calculations have made life simple. By using symmetry considerations alone one may predict the number of fundamental vibrational mode, their observation in the infrared and Raman spectra, and the way in which the various bonds and inter bond angles contribute to the molecular vibrations possessing a particular molecular symmetry. The independent vibrational motion of atoms in the unit cell is expressed as a normal mode of vibration. The quantized vibrational energy corresponding to each normal modes are called phonons. Since each atom can move in three directions (x,y,z), a N-atom molecule has 3N degrees of freedom. Out of these 3N, six degrees of freedom originating from translational and rotational degrees of freedom for a nonlinear molecule. Thus the net vibrational degrees of freedom (normal modes) are 3N-6. In the case of linear molecules, it is 3N-5, since two rotational degrees of freedom perpendicular to the molecular axis are degenerate in energy.

In the classical picture, when a molecule is illuminated by an electromagnetic (EM) wave, the electric field $\vec{E}$ associated with EM wave induces a dipole moment ($\vec{P}$) in the molecule which is related to the polarizability ($\alpha$) of the molecule [3-4]. The Polarizability ($\alpha$) is function of molecular vibration (vibrational coordinate q). So for a molecular vibration to be Raman active, ($d\alpha/dq$) should be non zero at $\vec{q}=0$.

**1.2. Brillouin spectroscopy**

Brillouin light scattering is generally refered to as inelastic scattering of an incident optical wave field by thermally excited elastic waves in a sample. The first theoretical study of the light scattering by thermal phonons was done by Mandelstam in 1918 [5-7]. L. Brillouin predicted independently light scattering from thermally excited

acoustic waves [8]. Later Gross [9] gave the experimental confirmation of such a prediction in liquids and crystals.

### 1.2.1. Principles of Brillouin Scattering

A sound wave of wave vector $\boldsymbol{q}$ and frequency $\omega$ propagating through a medium of dielectric constant ($\varepsilon$) sets up a modulation in $\varepsilon$ from which light may be scattered. Incident light of wave vector $k_i$ and frequency $\omega_i$ is scattered into a state $k_s$ such that $\mathbf{k_s} - \mathbf{k_i} = \pm \boldsymbol{q}$ where + sign refers to anti Stokes process and the – sign refers to Stokes process.

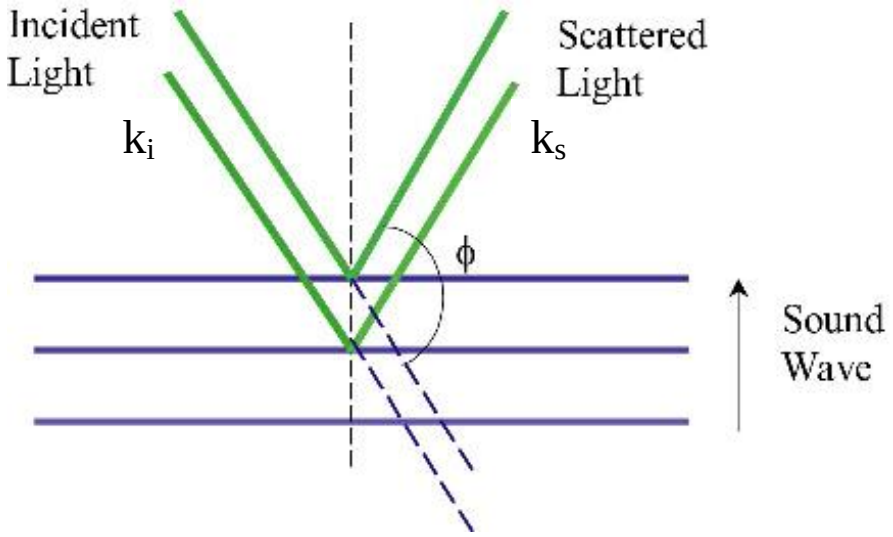


Figure 1.2. Interaction of the sound waves with light.

Correspondingly, the frequencies are related by $\omega_s - \omega_i = \pm \omega_B$. Since the velocity of sound $\mathbf{v_B}$ is very much less than that the velocity of light **c**, one can write as $|\mathbf{k_s}| = |\mathbf{k_i}|$ and so $|\boldsymbol{q}| = 2|\mathbf{k_s}|\sin\Phi/2$ where $\Phi$ is the angle between $k_s$ and $k_i$ (see figure 1.2) known as the scattering angle [10-11]. Since $|\boldsymbol{q}| = 0$ in the Brillouin scattering, we look at the phonons near the centre of the Brillouin zone. The expression for $|\boldsymbol{q}|$ does not apply to an optically anisotropic medium where the refractive index for the scattered light is different from that for the incident light.

### 1.2.2. Elasto–optical scattering mechanism

In the case of transparent solid, most of the scattered light emanates from the refracted beam in a region well away from the surface, and the kinematics conditions relating wave vector and frequency shift of the light pertain to bulk acoustic wave scattering [12-13]. The scattering in this case is mediated by the elasto – optic scattering mechanism, in which dynamic fluctuations in the strain field bring about fluctuations in the dielectric constant and these in turn translate into fluctuations in the refractive index. These fluctuating optical inhomogeneities result in inelastic scattering of the light as it passes through the solid. The phonons present inside a solid move with very small amplitudes creating fluctuation in the dielectric constant of the solid. This would act as a diffraction grating for an incident light. The fluctuation in dielectric constant of the solid is not static. Hence the diffraction grating appears to be moving, creating a Doppler shift in the diffracted light. Therefore Brillouin scattering can be explained as a combination of Bragg's reflection and Doppler shift.

### 1.2.3. Mathematical expression for Brillouin scattering

Brillouin scattering can be viewed as a Bragg's reflection of the incident wave by the diffraction grating created by thermal phonons. According to Bragg's law, the grating spacing 'd' can be expressed in terms of Bragg's angle ($\varphi/2$) and wavelength of the laser light inside solid $\lambda = \lambda_0/n$, where $\lambda_0$ is the laser wavelength in vacuum and 'n' is the index of refraction in the solid.

$$2d \sin(\varphi/2) = \lambda_o / n$$

The moving grating shifts the incident light with a Doppler shift, leading to scattered photons with a shifted frequency ($\Delta\nu$). Brillouin spectrum gives frequency ($\Delta\nu$) of any thermal phonons. The wave vector associated with the thermal phonons can be determined from the experiment geometry. For the scattering angle $\boldsymbol{\varphi}$, the sound velocity of phonon is given by the expression

$$V = \lambda_o \Delta\nu / (2 n \sin \varphi/2)$$

In the case of Back Scattering geometry, $\varphi = \pi$ and the above equation becomes

$$V_l = \lambda_o \Delta\nu / (2 n)$$

### 1.2.4. Ripple mechanism

Unlike the elasto-optic effect, the ripple mechanism does not occur in the bulk but at the surface of the specimen [14-16]. The phonons present at the surface of the sample move in thermal equilibrium with very small amplitudes creating corrugation on the surface, which can diffract incident light.

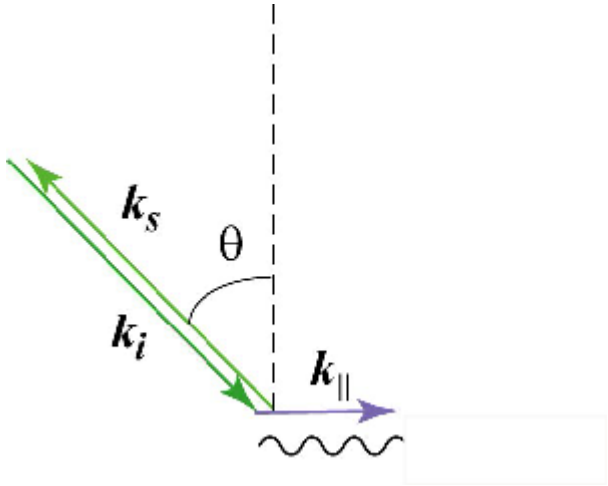


Figure1.3. Kinetics of a light scattering from a surface

The moving corrugating surface Doppler shifts the incident light, giving scattered photons with shifted frequencies. For backscattering geometry as shown in figure 1.3, the phase velocity ($V_{SAW}$) of surface acoustic wave can be written as

$$V_{SAW} = \lambda_o \Delta\nu / (2n \sin \theta)$$

where θ is the angle between the incident beam and the surface normal.

### 1.2.5. Difference between Raman and Brillouin Spectroscopy

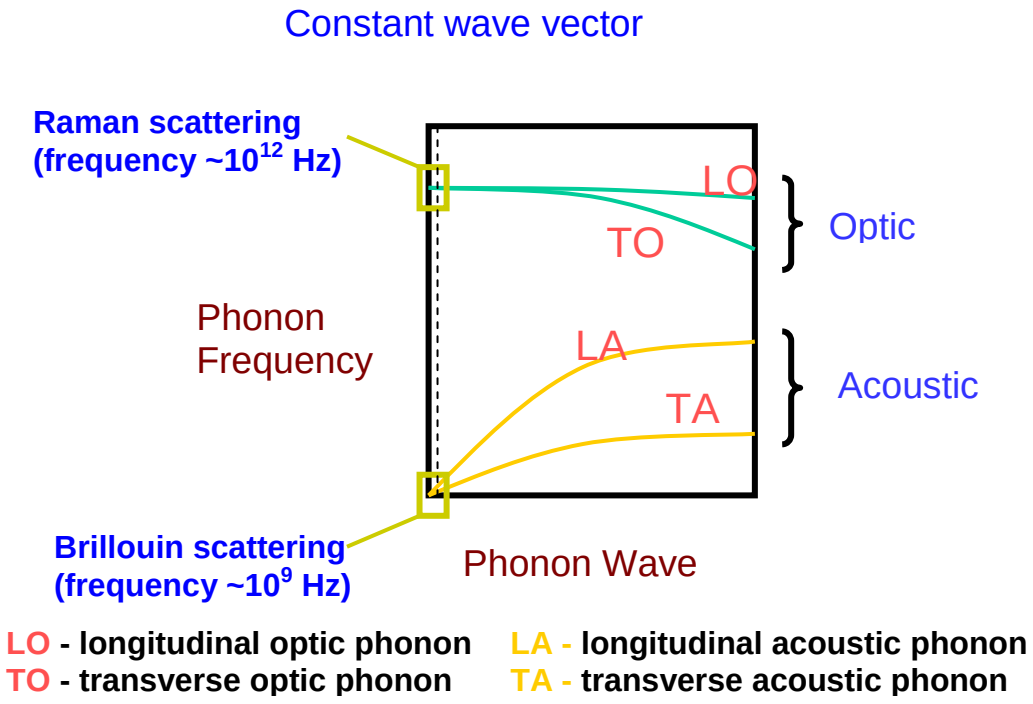


Figure1.4. Schematic representation of phonon dispersion relation

As shown in figure 1.4, the Raman spectroscopy deals with optic phonons which occur in the frequency range 10 to 4000 $cm^{-1}$ [17]. From Raman spectroscopy, one can get the information about atomic and molecular vibrational energy levels, molecular geometries, chemical bonds, interactions of molecules, identify the constituent of the sample and amount of material in the sample. But on the other hand, Brillouin spectroscopy deals with acoustic phonon which occur in the frequency range from 0.1 $cm^{-1}$ to 5 $cm^{-1}$. Using Brillouin spectroscopy, one can determine acoustic phonon velocities hence the elastic constants and the optical constants of the material of interest [18]. In both the spectroscopy, the peak width gives the phonon lifetime

## 1.3. Effect of High Pressure

The most important factors affecting inter - and intra – atomic distances in solids and molecular solids are temperature, pressure and geometrical configuration.

Temperature changes volume and excitations of the materials but in comparison pressure changes only volume. Pressure is a stronger perturbant compared to temperature. For example, the volume change in Si from 0 K to melting is only 1.8% but the volume change is 5% for a pressure of 10 GPa. Pressure is an experimental parameter that can be tuned over a wide range to probe the properties of condensed matter system. The electronic, structural and vibrational properties of materials under pressure are areas of great interest. By varying the pressure, we can obtain insight into the interaction between atoms and molecules. These investigations have resulted in new findings in structure, bonding and dynamics in solids, liquids and gases as well as allowing the creation and recovery of new materials. In general, the response of materials under high pressure is either occurrence of phase transformations or just compression with consequent changes in the physical properties. Pressure induced phase transformation leads to phases of higher density. Due to increasing repulsive inter atomic potentials, the diffusion – controlled phase transition is highly reduced. So all the phase transformation due to high pressure is displacive which can be characterized by change in symmetry. This will be useful to find the intermediate phase of the materials under pressure where it is not stable at ambient conditions. Especially for molecular solids, the inter–molecular bonds are weaker than intra – molecular bonds. The application of hydrostatic pressure, primarily reduces the distances between the end – group, non – bonded atoms which enhances the repulsive forces in the system and on further application of the pressure, in order to overcome the repulsive forces, the system has to rearrange itself by bond breaking, bond making or coordination change as a result new phase of system emerges. In crystals, the close packing is achieved mainly due to coordination change; this can be sterically hindered due to the strong intra–molecular interaction in the molecular solids [19-21]. The close packing in molecular solids are achieved by change in conformational order which will minimize the free energy of the molecular arrangements. The above close packing geometry plays an important role in organic molecules which is explained in this thesis.

### 1.3.1. Pressure Units

Pressure is defined as force per unit area. The most common unit used to describe pressure is Pascal (Pa). **1 Pa = 1 N/m$^2$** [22]**,** where N (Newton) is the name of the unit for force. One Pascal (Pa), if expressed in terms of the SI base units, is equal to (kg $m^{-1}s^{-2}$). It is also common practice to use non-SI units to measure pressure, namely, atmospheres, bars. 1 bar = $10^5$ Pa = 0.9 atm. It is important to know the extent of pressure experienced by material in nature. The pressure at the center of earth is equal to 360 GPa (360 x $10^9$ Pa), and the pressure experienced in the deepest part of the ocean is 140 GPa. Many of the planets like Jupiter have pressure greater than 9000 GPa (9 TPa) in the center of it. 90% of the materials transform to their densest form upon application of pressure around 30 GPa. Hence very few studies are seen above these pressures.

### 1.3.2. Methods for generating High Pressure

In order to apply pressure on the materials under investigation, one can adopt two methods [23-24].

1. **Static pressure** – As the name suggests the material is held under constant pressure. The system remains in equilibrium; hence there is no change in temperature. Such pressures are applied by mechanical methods. Eg., Anvil cells. Maximum pressure achieved are 300 to 500 GPa.
2. **Dynamic pressure** – In the case of dynamic pressure, the material is exposed to a mechanical stress for a very short duration and source of pressure is removed. It is equivalent to striking the material with hammer. Since it is non-equilibrium situation, the temperature of the sample also changes. It is possible to achieve pressure increase of 2.5 TPa in such cases. E.g, such experiments are shock loading by gas gun.

In this present case, we have applied only static pressure using Diamond Anvil Cell on materials at room temperature.

.

## 1.4. Phase Transitions

One can classify the phase transitions into two categories. i) Phase transitions for which none of the phases is distinguished by intrinsically different properties: they are characterized by a change of order, structure, or symmetry in the material, eg., evaporation and solidification of a liquid, melting and sublimation of solid, and separation of mixture of liquids. ii) Transitions where one of the phases has a new physical property; it can also be associated with a change in symmetry or structure. Eg., ferromagnetic/paramagnetic, ferroelectric/paraelectric, and superconducting phase transitions

### 1.4.1. Phase transitions related to structural transitions

Many substances in the solid state undergo a phase transition associated with a change in structure. During the transition, the arrangement of atoms is modified and leading to a change in the symmetry of the crystal. These are structural transitions. This change is induced by changes in atomic position in the system. Structural Phase transition in solids may be classified into three categories [26-28]:

1. **Displacive transitions** proceed through a small distortion of the bonds (dilatational or rotational). The atomic displacements are very low (0.01-0.1Å) and the specific heat is low (a few J/g). eg., transformation of quartz (at 843 K), tridymite (at 433 K) and crystobalite (at 523 K).

2. **Reconstructive transitions** proceed through the breaking of the primary or secondary bonds. They imply large atomic displacements with 10-20% of distortion in the lattice. An example is the aragonite ($P_{nma}$) to calcite (R3c) transition in $CaCO_3$ (at 723 K).

3. **Order- disorder transition** in which the order of the system changes.

Three principal types of disordering transitions may be distinguished as:

i) **Positional disordering** in a solid arises either when atoms or ions occupy inappropriate sublattice positions, or when more positions are available for the atoms than are necessary. Eg., CuZn [29].

ii) **Orientational disordering** which may be static or dynamic where the ions or the basic units occupying the lattice sites containing more than one atom. In such a

situation, more than one distinguishable orientation becomes possible for ions in the lattice. Eg., orientaional disorder in molecular solids [30-32].

iii) **Disordering associated with electronic and nuclear spin states**. By virtue of the presence of unpaired electrons or spins, atoms or ions behave as tiny magnets and impart magnetic field to the lattice when present in a parallelly ordered state. As the temperature increases, these elementary magnets on the lattice flip over to other orientations where the materials become disordered.

### 1.4.2. Phase Transitions related with no change in structure

Phase transitions in which the appearance of a new property is not correlated with any modification of the crystal structure of the material are classified under this category; It is thus not associated with a change in symmetry. Most of such phase transitions involve the properties of the electrons of a solid. For example, In the case of ferromagnetic, superconducting and metal/insulator transitions. Magnetism encountered in crystalline solids and metallic glasses.

### 1.4.3. Order of Phase Transitions

A solid undergoes a phase transition when a particular phase of the solid becomes unstable under a given set of thermodynamic conditions[33]. The variation in free energy at the transition is associated with structural or compositional changes. During a phase transiton, thermodynamic quantities like entropy, volume, heat capacity and so on undergo discontinuous changes. More generally, the physicist P. Ehrenfest proposed a classification of phase transitions based on the thermodynamic potentials [34]. They are as follows.

**(i) First order Transition:** The transition is said to be first order when the first derivative of the free energy G is discontinuous given by equation

$$S = -(\partial G/\partial T)_P \qquad V = (\partial G/\partial P)_T \qquad H = \partial(G/T)/\partial(1/T)$$

Where S is entropy, V is volume and H is enthalpy.

**(ii) Second order Transitions** in which the thermodynamic potentials and their first order derivatives are continuous, while some second derivatives with respect to state

variables are reduced to zero or approach infinite at the transition. The thermodynamic variables related to second derivative of Gibbs free energy are as follows.

$$C_P = (\partial^2 G/\partial T^2)_P = -T\,(\partial S/\partial T), \quad \kappa_T = -(\partial^2 G/\partial P^2)_T = -(1/V)\,(\partial V/\partial P)_T$$

where $C_P$ is the specific heat at constant pressure, $\kappa_T$ is the compressibility at constant temperature. For these transitions, we continuously pass from one phase to another phase without being able to realize the coexistence of the two phases. These different thermodynamic behaviors can be demonstrated experimentally by directly or indirectly studying the thermodynamic behavior of characteristic physical quantities in the vicinity of the transition.

### 1.4.4. Significance of Raman scattering for probing Phase Transitions

The Raman spectra will give the information like the peak position (ω), full width half maximum (Γ) and the intensity (A). The normal mode frequency (ω) is one of the main parameter to probe phase transitions. The appearance and disappearance of the Raman mode or the change in slope (dω/dP) signifies a phase transition. Since ω is sensitive to symmetry and environment of the system, any changes would influence the behavior of ω. First order transition is observed when there are discontinuity in (ω) near the transition pressure or temperature. During a second order transition, there is a gradual slope change (dω/dP) near the phase transition. Broadening of the mode in the spectra is due to the contribution of all wave vector phonons which signifies a disordered phase. On the contrary sharp bands in the spectra are due to the contribution of only zone centre phonons. This signifies an ordered phase.

## 1.5. Materials under Investigation

### 1.5.1. Saturated Hydrocarbons – Alkanes

Compounds that contain only carbon and hydrogen are known as **hydrocarbons**. The hydrocarbons with out double or triple bonds are called saturated hydrocarbons and they are known as alkanes. The medium chain alkanes studied in the thesis are shown in figure 1.5

(a) (b) (c)

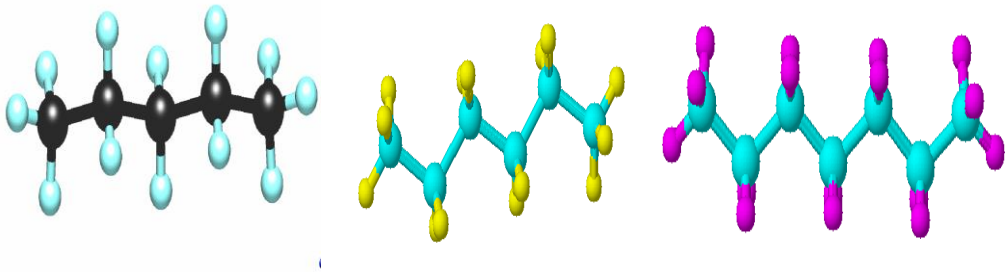

**Figure 1.5.** Shows the molecular structure of (a) n-pentane, (b) n-hexane, (c) n-heptane

The n-alkanes are all **straight-chain hydrocarbons**, in which the carbon atoms form a chain that runs from one end of the molecule to the other. The generic formula for these compounds can be understood by assuming that they contain chains of $CH_2$ groups with an additional hydrogen atom capping either end of the chain. Thus, for every *n* carbon atoms there must be $2n + 2$ hydrogen atoms: $C_nH_{2n+2}$. Straight-chain structures are "normal paraffins", branch-chain structures are "isoparaffins", and ring-type structures are "cycloparaffins".

Hydrocarbon chains are among the most important structural units in chemistry. Knowledge of their detailed form and rotational isomerism is of practical interest to chemists in many areas of research. Extensive studies have been made of the structure of chains and the conformational enthalpy differences are well known in the liquid phase. An electron diffraction investigation of the gaseous hydrocarbons n-butane through n-heptane was initiated several years ago. Detailed accounts have already been published of the complete diffraction analysis of n-butane [35] and of the average bond lengths and bond angles in vapor molecules of higher alkanes [36]. The distribution between trans and gauche conformations and about the steric interactions have been reported earlier [37]. An accurate determination of the conformational energies of *n*-pentane has become a mandatory step for, among others, a sound interpretation of its ionization, [38] electron momentum [39] infrared or Raman spectra [40], due to the impact of the conformation on orbital energies [38,39] electron density distributions [39]

and molecular vibrations [40]. A high-level theoretical study of the conformational equilibrium of n-pentane has been done by Salam and coworkers [41]. The number of rotational isomers and their energy difference for n-butane, n-pentane, n-hexane and n-heptane in the liquid as well as solid phase has been extensively studied by Sheppard and co-workders [42]. IR or Raman techniques are used in conventional analysis to provide information on the chemical composition of bulk organic materials. They can also give information on molecular conformation [43] or alignment [44], glass transition [45] and the effects of pressure [46]. The effect of pressure is important in perturbing the distribution of conformers. The Snyder *etal* is clearly explains the effect of pressure on conformer equilibria on liquid n-hexane [47]. The pressure induced liquid-solid transition of n-pentane [48], n-hexane [49] and n-heptane [50] has been reported earlier. In the present work, we have studied the pressure induced solid-solid transition of n-pentane, n-hexane and n-heptane as well as their conformer populations at different physical states.

### 1.5.2. Perfluorocarbons (PFCs)

Perfluoro carbons are similar to alkanes with all the hydrogen replaced by fluorine. Perfluorocarbon (PFC) is one of the constituent of global warming green house gases. Natural geological emissions have been responsible for the PFCs that have accumulated in the atmosphere over a very long time. However, the largest current source is aluminum production, releasing $CF_4$ and $C_2F_6$ as by-products. With a phase – out of ozone depleting substances, PFCs have been introduced into several specialized applications. The low volume level of use is associated with the fact that PFCs are relatively expensive products and are only selected if they are absolutely necessary for performance, system efficiency or safety. The manufacturing cost of PFCs is related to high material costs and processes that have limited scope for scale – up. The industrial use is mainly linked to electronic industry [51], as PFCs offer a unique combination of properties. They are inert, good dielectrics, non-flammable, non-toxic and compatible with a broad range of materials. Semiconductor manufacturing processes utilizes PFC gases as a fluorine source for chemical vapor deposition chamber cleaning and

specialized plasma etching [52]. PFC liquids $C_5F_{12}$ and $C_6F_{14}$ are traditionally used as direct contact immersion cooling liquid for high power electronics, mainly as replacement for CFC – 133, with required good dielectric characteristic at optimum material compatibility and thermal stability. $C_3F_8$ has been developed as an inert agent for a number of specialty refrigerant formulations.

**(i) Perfluorohexane ($C_6F_{14}$) and perfluroheptane ($C_7F_{16}$).**

Perfluorohexane is used in one formulation of the electronic cooling liquid/insulator fluorinert for low temperature applications due to its low boiling point of 56 ºC and melting point of -90 °C. It is odorless and colorless. It is used as a solvent and a coolant. In medical imaging, it is used as a contrast agent. Perfluorohexane on the other hand is considered chemically and biologically inert. It is unusual in that perfluorohexane absorbs oxygen higher than found in normal air. This means that animals can be submerged in a bath of perfluorohexane without drowning, as there is sufficient oxygen available in the solvent to allow respiration to continue. This has led to the experimental use of perfluorohexane in treating burn victims, as their lungs can be filled with either perfluorohexane vapor or in extreme cases liquid perfluorohexane, allowing breathing to continue without the problems normally seen with pulmonary edima that sometimes occur when the inside of the lungs have been burnt e.g. by inhalation of hot smoke [53].

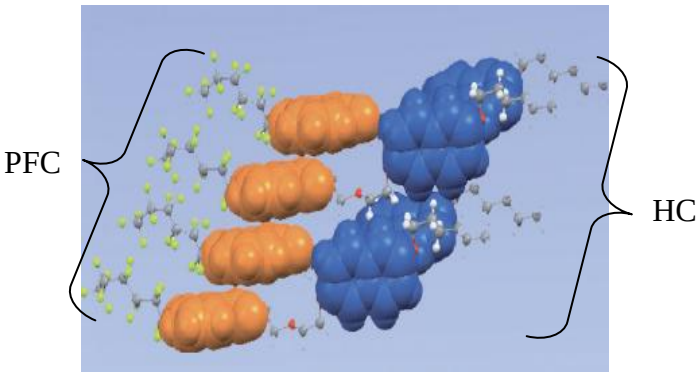


Figure 1.6. Segregated assemblies in bridged electron-rich and electron-poor p-conjugated moieties [54]

In organic-based devices such as photovoltaic cells, electron-rich conjugated molecules like PFC and electron-poor conjugated molecules like hydrocarbon (HC) need to be assembled into segregated structures for efficient charge separation and charge-carrier transport (see figure 1.6) [54]. Due to the large number of above applications of perfluorocarbons, it is interesting to study their interaction of molecules as well as their conformational properties when they densely packed. The existence of conformational equilibria in the gaseous and in the liquid states of n-perfluorobutane, n-perfluorohexane and n-perfluorooctane and in some solid phases of the latter, using IR and Raman spectroscopy have been explained earlier [55]. The structure of the isomers present in the different physical states of n-$C_4F_{10}$, n-$C_6F_{14}$ and n-$C_8F_{18}$ is discussed by Rey-Lafon and coworkers [55-56]. The quantitative intensity measurement of perfluropentane, perfluorohexane and perfluoroheptane were made on appropriately chosen pairs of lines belonging to different isomers as a function of temperature in the liquid phase [57, 58]. In the present work, we have studied the pressure induced solid-solid transitions of perfluorohexane as well as perfluoroheptane and their stable conformer populations at every solid-solid transitions.

### 1.5.3. Tungstates and Molybdates

The tungstates and molybdates are almost always categorized in one group. The minerals they contain are chemically similar to each other. These minerals are heavy, soft, and brittle. The tungstates and molybdates are compounds of one or more metallic elements and the tungstate radical ($BO_4$, B=W, Mo).

#### (i) Importance of $ABO_4$ compounds

The $ABO_4$ type compounds (A=Ca, Ba, Bi, Sr, Pb, Cd…), (B=W, Mo, V) have been widely investigated because of their geological relevance. Figure 1.7 shows the crystal structure of $ABO_4$ elements. Apart from this, these materials are important host material for laser [59-61]. The tungstate and molybdates are easily doped with rare-earth ions and are available in the form of large single crystals. $CaMoO_4$ and $CaWO_4$ are two of series of isostructural divalent metal molybdates and tungstates, known generically as

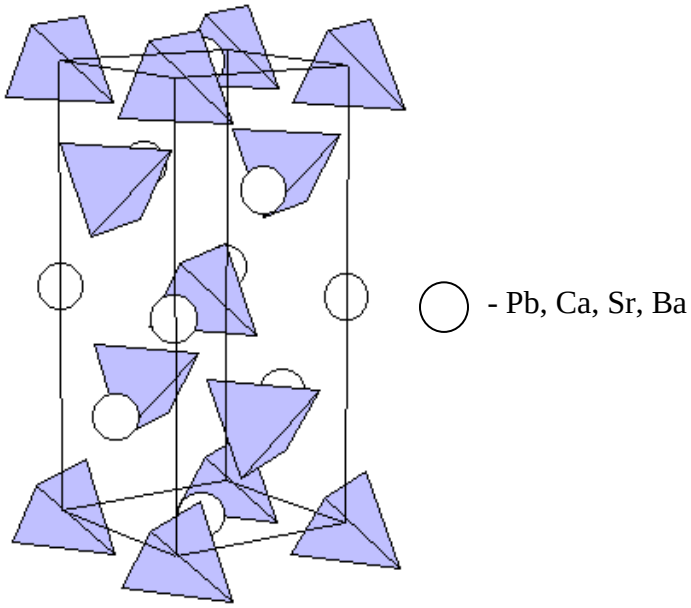


Figure 1.7. Schematic representation of $ABO_4$ crystal structure

scheelites [62]. These are important host materials for a variety of inorganic phosphor and host crystal for studying electronic energy transfer between rare earth ions. These doped crystals are the subject of much current optical maser study. The triple molybdates like $Gd_2(MoO_4)_3$ and $Tb_2(MoO_4)_3$ are key materials for improper ferroelectrics [63].

**(ii) Barium Tungstate ($BaWO_4$)**

The development of high-power solid–state lasers [64-66] emitting in different spectral regions is of current interest for laser physics. One of the ways to solve this problem is by Stimulated Raman scattering (SRS) conversion of radiation from near – IR lasers. The well – suited materials for SRS active media are the most efficient $Ba(NO_3)_2$ and $KGd(WO_4)_2$ crystals. These crystals have very high SRS gain $g$ = 6 cm $GW^{-1}$ for potassium gadolinium tungstate and 11 cm $GW^{-1}$ for Barium Nitrate having the pumping wavelength at 1.06 μm. The SRS conversion of trains of single – mode, single frequency, self – phase – conjugated pulses from a Nd – YAG laser in a Barium nitrate has the average power and pulse energy up to 5 W and ~ 30 mJ, respectively [67-68].

The SRS conversion efficiency is 15% - 30%. Being hygroscopic and poor mechanical and thermal parameters, the $Ba(NO_3)_2$ crystals cannot be useful for SRS. Although $KGd(WO_4)_2$ have no such disadvantages, their radiation resistance is low and they have low SRS transition cross section. These limitations severely prevent the development of high – power solid – state Raman lasers. So the search for new SRS – active media with good mechanical and thermal properties and a high radiation resistance becomes urgent. One of the highly efficient $BaWO_4$ crystal having $g \geq 8.5$ cm $GW^{-1}$ will satisfy the above requirement for SRS transition. The Raman line width of $BaWO_4$ is larger than $Ba(NO_3)_2$, but the peak value of the Raman cross section for the $BaWO_4$ is almost same that of Barium nitrate. Crystal structure of $CaMoO_4$, $SrMoO_4$, $SrWO_4$ and $BaWO_4$ has been refined by neutron diffraction data [69]. High pressure x-ray and lattice dynamic studies on $BaWO_4$ have been reported earlier [70-71]. We have carried out temperature dependent Brillouin studies on $BaWO_4$ to study the electronic properties of this system across the low temperature transition.

**(iii) Lead Tungstate ($PbWO_4$)**

Lead Tungstate is one of the most prominent crystal for dense, fast and radiation – hard materials for high quality $\gamma$ - ray detectors at high energies. It has a maximum emission at 420 – 440 nm. $PbWO_4$ is very dense with a density of $\rho$ - 8.2 $g/cm^3$. it has a refractive index of 2.2 – 2.3 and is non – hygroscopic. The radiation hardness will be determined by crystal quality on various conditions of crystal growth. The crystal structure of lead tungstate, $PbWO_4$, is tetragonal, scheelite type, space group $I4_1/a$. This compound, due to the difference in the vapor pressure of the two raw oxides, $WO_3$ and PbO, used in the crystal growth, is frequently subjected to lead deficiency [72]. It has been reported by one group that lead vacancies can order in a crystal structure derived from the scheelite type, but of lower symmetry and described by the space group *P4*/*nnc* or *P4*. Futher the influence of cation on the crystal structure can help in modeling the effect of impurities on the physical properties. The introduction of cationic impurities in the host crystal can achieve the laser light emission at desired frequencies. The scheelite materials like $PbMoO_4$ and $PbWO_4$ are promising materials for acousto – optic

applications and cyogenic phonon scintillation detectors [73]. Pressure induced x-ray as well as lattice dynamic studies on $PbWO_4$ have been explained earlier [74-75]. Temperature dependent Brillouin studies on $PbWO_4$ were carried out to study the effect of Pb vacancies and its contribution in the structural and physical properties of the system.

### 1.5.4. Chalcopyrite crystal structure – $AgGaS_2$

A large number of recent studies in non-linear optics have been devoted to compounds of the II-VI or III-V families with sphalerite structure, showing their large non-linear susceptibility. Unfortunately they are optically isotropic and consequently not phase matchable. The chalcopyrite structure compounds I-III-$VI_2$ belongs to the ternary semiconductors and have quite similar physical properties as the binary analogs [76]. The presence of third atomic component as well as the non cubic structure widens the possible range of application in the solar cells, solar energy conversion, light emitting diode (LED) and various non-linear devices. In addition, the chalcopyrite, being uniaxial, is birefringent and hence allows phase-matching possibilities which are not available in the isotropic binary compounds. The silver thiogallate $AgGaS_2$, which is one of the typical chalcopyrite representatives, attracts much attention as a perspective nonlinear optical material in the infrared region [77] because it has a direct band gap [78] in the blue region at 2.75 eV and the large non-linear optical coefficient [79]. Its structural parameter, lattice vibrational modes [80-83] and elastic properties [84-85], electronic band structure [86] as well as linear and nonlinear optical properties [79] have been the subject of many studies. The chalcopyrite structure is a super structure of zinc-blende. It is described by the space group $I\bar{4}2d$. The primitive unit cell includes two formula units. Figure 1.8. shows the crystal structure of $AgGaS_2$. The crystallographic tetragonal body-centered unit cell consists of four molecules and contains 16 atoms [87] (see figure 1.8).

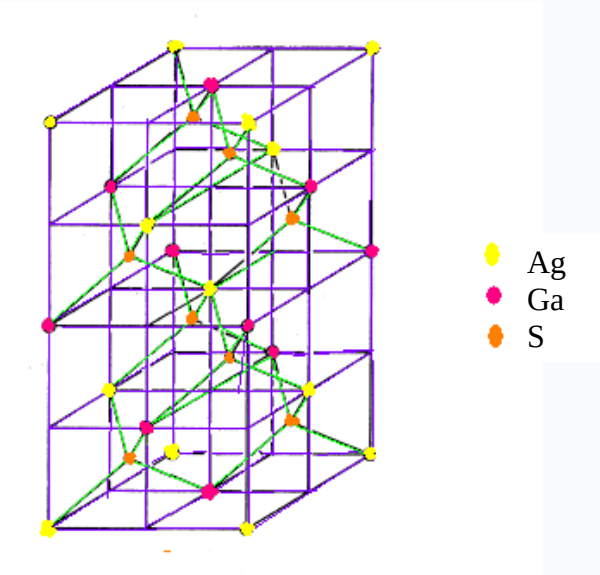


Figure 1.8. a) Schematic representation of $AgGaS_2$ crystal structure.

The chalcopyrites most often exhibit a tetragonal compression along *c* axis, i.e., $c<2a$. The presence of two different cations from different columns of the periodic table gives rise to two anion-cation bonds, Ag-S and Ga-S. The respective bond lengths Ga-S and Ag-S in $AgGaS_2$ are 2.276 and 2.556 A°[88] respectively. It is interesting to look at the mechanical stability of $AgGaS_2$ at lower temperature and we have carried out Brillouin studies to look into this aspect.

## 1.6. Bibliography


[1]. Raman. C.V. and Krishnan K.S, A new type of secondary radiation, Nature **121**, 501, (1928).

[2]. Albert Cotton. F. Chemical Applications of Group Theory, A wiley-interscience publication, 1990.

[3] Long D.A. The Raman Effect: A unified Treatmetn of the Theory of Raman Scattering by Molecules, John Wiley & Sons Ltd, 2002

[4]. Banwell C.N. Fundamentals of Molecular Spectroscopy, Tata McGraw-Hill Publishing Company Limited, 1994.

[5]. Fabelinskii, I. L. *Molecular Scattering of Light*. New York, Plenum (1968).

[6]. Landau, L. D., E. M. Lifshits and L. P. Pitaevskii. *Electrodynamics of continuous media*. Pergamon, Oxford, (1984).

[7]. Mandelstam L.I. "Light scatteirng by inhomogeneous media", *Zh. Russ. Fiz-Khim. Ova*. **58**, 381 (1926) (in Russian)

[8]. Brillouin L., Diffusion de la lumiere et des rayonnes X par un corps transparent homogene; influence del'agitation thermique. *Ann. Phys*. (Paris) 17, 88 (1922).

[9]. Gross, E. "Change of wave-length of light due to elastic heat waves at scattering in liquids". *Nature* **126** (201) 400 (1930).

[10]. Brillouin. L. Ann. Phys. (Paris) **17**, 88 (1922).

[11]. Benedek. G. B, Fritsch. K, Phys. Rev. **149**, 647 (1966).

[12]. Hayes, W. and R. Loudon. *Scattering of Light by Crystals*. New York, Wiley. (1978)

[13]. Grimsditch, M. "Brillouin Scattering". *Handbook of Elastic Properties of Solids, Liquids, and Gases*. Volume I: *Dynamic Methods for Measuring the Elastic Properties of Solids.* M. Levy, H. Bass, R. Stern and V. Keppens, Eds. New York, Academic Press. I. 331-347 (2001).

[14]. Mutti, P., C. E. Bottani, G. Ghislotti, M. Beghi, G. A. D. Briggs and J. R. Sandercock. "Surface Brillouin Scattering - Extending Surface Wave Measurements to 20 GHz". *Advances in Acoustic Microscopy*. A. Briggs, Ed. New York, Plenum Press. **I** 249-300 (1995).

[15]. Comins, J. D. "Surface Brillouin Scattering". *Handbook of Elastic Properties of Solids, Liquids, and Gases*. Volume I: *Dynamic Methods for Measuring the Elastic Properties of Solids*. M. Levy, H. Bass, R. Stern and V. Keppens, Eds. New York, Academic Press. **I** 349-378 (2001).

[16]. M. G. Beghi, A. G. Every, and P. V. Zinin. "Brillouin Scattering Measurement of SAW Velocities for Determining Near-Surface Elastic Properties", in T. Kundu ed., *Ultrasonic Nondestructive Evaluation: Engineering and Biological Material Characterizatio*n, CRC Press, Boca Raton, chapter 10, 581-651 (2003).

[17]. Kittel. C, Introduction to Solid State Physics, John Wiley & Sons, Inc. 1953.

[18]. Auld B. A. Acoustic Fields and Waves in Solids, A Wiley-Interscience Publications, 1973.

[19]. Sharma. S. M. and Sikka. S. K. " Pressure Induced Amorphization in Materials" Proc. Mater. Sci. **44**, 1, (1996).

[20]. Sikka. S.K, Sharma. S. M, Current Science, **63**, 317, (1992).

[21]. Ramachandran. G. N, Sasisekaran. V. Adv. Protein, Chem. 23, 283, (1968).

[22]. *Comptes rendus de la 14$^{e}$ CGPM*, **78**, 1972, (1971)

[23]. Jayaraman. A, Rev. Mod. Phys. **55**, 65, 1983.

[24]. Chidambaram. R, Sharma. S. M, Bull. Mater. Sci. **22**, 153, (1999).

[25]. Weinstein. B. A, Zallen. R, "Light Scattering in Solids IV," ed. By Cardona. M, Guntherodt, Topics Appl. Phys.,Vol. 54 (Springer, Berlin, Heidelberg 1984) Chap. 8.

[26].Buerger. M. J, in " Phase Transformations in Solids," eds. Smoluchowski. R, Mayer. J. E, and Weyl. W. A, John Wiley, NewYork, 1951.

[27]. Buerger. M. J, Fortschr. Miner., **39**, 9, 1961.

[28]. Rao. C.N.R., Rao. K. J, "Progress in Solid State Chemistry," ed. Reiss. H, Vol 4. Pergamon Press, Oxford, 1967.

[29]. Sato. H, in "Physical Chemistry: An Advanced Treatise," ed. Eyring. H, Henderson. D, Jost. W, Vol.10, Academic Press. New York, 1970.

[30]. G. Kavitha and Chandrabhas Narayana J. Phys.Chem. B, Vol. **110**, 8777, (2006).

[31]. G. Kavitha and Chandrabhas Narayana, J. Phys.Chem.B, **111**, 7003 (2007).

[32]. G. Kavitha and Chandrabhas Narayana J. Phys.Chem. B**, 111**, 14130,(2007).

[33]. R. Roy, in “Phase Transitions,” ed. Henisch. H. K, Roy. R, Cross. L.E, Pergamon Press, NewYork, 1973.

[34]. Ehrenfest. P, Proc.Amsterdam Acad., **36**, 153, (1933).

[35]. Bonham. R.A, Bartell. L.S, J. Amer.Chem.Soc. **81**, 3491, (1959).

[36]. Bonham. R.A, Bartell. L.S, Kohl. D.A, J. Amer. Chem. Soc. **81**, 4765, (1959).

[37]. Bartell L.S, Kohl D.A, J. Chem. Phys. **39**, 3097, (1963).

[38]. Deleuze M., Delhalle J., Pickup B. T., Svensson S., J. Am. Chem. Soc. **116**, 10715, (1994)

[39]. Deleuze M. S.,. Pang W, Salam A., Shang R. C., J. Am. Chem. Soc. **123**, 4049, (2001)

[40]. Gough K. M., Srivastava H. K., J. Phys. Chem. **100**, 5210, (1996)

[41]. Salam A., Deleuze. M. S. J. Chem. Phys. **116**, 1296, 2002.

[42]. Sheppard. N, Szasz. G. J, J. Chem. Phys. **17**, 86, 1949.

[43]. Begum R. Matsuura H., J. Chem. Soc. Faraday Trans. **93**, 3839, (1997).

[44]. Bokobza L., Buffeteau T., Desbat B., Appl. Spec. **54**,360, (2000).

[45]. Atkinson J.R., Biddlestone F , Hay J.N., Polymer **41**, 6965, (2000).

[46]. K.K. Zhuravlev and M.D. McCluskey, J. Chem. Phys. **117**, 3748, (2002).

[47]. Patrick.T.T.W, Henry. H.M., Snyder.R.G., J. Chem. Phys. **79**, 2369, (1983).

[48]. Qiao, E.; Zheng, H. *Appl. Spectrosc.* **59**, 650,(2005).

[49]. Huai, W.; Haifei, Z.; Qiang, S. *Appl. Spectrosc.*, ***59,*** 1498, (2005).

[50]. Yamaguchi, M.; Serafin, S. V.; Morton, T. H.; Chronister, E. L. *J.Phys. Chem. B*, **107**, 2815, (2003).

[51]. Yang Y F,. Herbert Y. F, Rüschen L, H; Cooling, R. J. *Br. Med. J.*, ***325(7363)***, 532, (2002).

[52]. "Perfluorochemucal Blood Substitutes", Naito, R., Yokoyama, K., p 57, The Green Cross Corporation, Technical Information Ser. No. 5, June 30, 1978.

[53]. Mario Rüdiger, Hans Proquitté, Roland Wauer; “3rd european symposium on perfluorocarbon application”, Eur J Med Res **8**, 168, (2003)

[54]. Travis L. Benanti, Pranorm Saejueng ,Venkataraman D. Chem. Comm. 641, (2007).

[55]. Campos-Vallette M.; Rey-Lafon M., J. MoL Struct., **101**, 23, (1983).

[56]. Campos-Vallette M.; Rey-Lafon M., J. MoL Struct., **118**, 245 (1984).

[57]. Campos-Vallette M.; Rey-Lafon M., J. MoL Struct, **101**, 23, (1983).

[58]. Campos-Vallette M.; Rey-Lafon M., chem..phy. lett. **89**, 189, (1982).

[59]. Pask H. M., Prog. Quantum Electron. **27**, 3 , (2003).

[60]. Pask H. M. , Piper J. A, Opt. Commun. **148**, 285, (1998).

[61]. Cerny P., Jelinkova H., Zverev P. G.,. Basiev T. T, Prog. Quantum Electron. **28**, 113 (2004).

[62]. Errandonea D.,. Manjo F.J ´ Somayazulu M., Ha¨usermannb D, J. Sol. Stat. Chem **177**,1087, (2004)

[63]. Kim. Q, Ullman. F. G, Phys. Rev. B. **18**, 3579, (1978).

[64]. Basiev T. T., Sobol A. A.,. Voronko Yu. K, Zverev P. G., Opt. Mater.(Amsterdam, Neth), **15**, 205 (2000).

[65]. Zverev P. G., Basiev T. T., Prokhorov A. M., Opt. Mater. (Amsterdam,Neth.) **11**, 335, (1999).

[66]. Findeisen J., Eichler H. J., Peuser P., Kaminskii A. A., Hulliger J., Appl. Phys. B: Lasers Opt. **70**, 159 (2000).

[67]. Cerny P., Zverev P. G., Jelinkova H., Basiev T. T., Opt. Commun. **177**, 397 (2000).

[68]. Cerny P.,. Jelinkova H, Miyagi M., Basiev T. T., Zverev P. G., Proc. SPIE **4630**, 108 (2002).

[69]. Gurmen. E, Daniels. E, King. J. S. J. Chem. Phys. **55**, 1093, (1971)

[70]. Errandonea D., Pellicer-Porres J., Manjón F. J., Segura A., Ch.Ferrer-Roca, Kumar R. S., Tschauner O., Rodríguez-Hernández P., López-Solano J., Radescu S., Mujica A., Muñoz A., Aquilanti G., Phys. Rev. B **73**, 224103 (2006).

[71]. Errandonea D., Pellicer-Porres J., Manjón F. J., Segura A., Ch.Ferrer-Roca, Kumar R. S., Tschauner O., Rodríguez-Hernández P., López-Solano J., Radescu S., Mujica A., Muñoz A., Aquilanti G., Phys. Rev. B **74**, 144111 (2006).

[72]. LIU Ting-Yu; ZHANG Qi-Ren; ZHUANG Song-Lin; Chin.Phys.Lett. **22**, 442, (2005).

[73]. Bravin M., Bruckmayer M., Bucci C., Cooper S., Giordano S., von Feilitzsch F., Hohne J., Jochum J., Jorgens V., Keeling R., Kraus H., Loidl M., Lush J., Macallister J., Marchese J., Meier O., Meunier P., Nagel U., Nussle T., Probst F., Ramachers Y., Sarsa H., Schnagl J., Seidel W., Sergeyev I., Sisti M., Stodolsky L.,

Uchaikin S., Zerle L., Astropart. Phys. **12**, 107,(1999).

[74]. Errandonea D., Pellicer-Porres J., Manjón F. J., Segura A., Ch.Ferrer-Roca, Kumar R. S., Tschauner O., Rodríguez-Hernández P., López-Solano J., Radescu S., Mujica A., Muñoz A., Aquilanti G., Phys. Rev. B **72**, 174106 (2006).

[75]. Errandonea D., Pellicer-Porres J., Manjón F. J., Segura A., Ch.Ferrer-Roca, Kumar R. S., Tschauner O., Rodríguez-Hernández P., López-Solano J., Radescu S., Mujica A., Muñoz A., Aquilanti G., Phys. Rev. B **74**, 144112 (2006).

[76]. Parthe.E, Crystal chemistry of tetrahedral structures (Gordon and Breach. New York, 1964).

[77]. Shay. J. L, Wernich. J. H, Chalcopyrite semiconductors. Growth. Electronic Properties and Applications (Pergamon, Oxford, 1975).

[78]. Goryunova. N. A, Compound Diamond like Semiconductors,(Nauka, Moscow, 1968).

[79]. Boyd. G. D, Kasper. H. M, McFee. J.H, IEEE J. Quantum Electron. QE-7, 563 (1971).

[80]. G. D. Holah, J. S. Webb, and H. Montgomery, J. Phys. C **7**, 3875, (1974)

[81]. D. J. Lockwood and H. Montgomery, J. Phys. C **8**, 3241, (1975)

[82]. J. P. van der Ziel, A. E. Meixner, H. M. Kasper, and J. A. Ditzenberger, Phys. Rev. B **9**, 4286 (1974)

[83]. W. H. Koschel and M. Bettini, Phys. Status Solidi B **72**, 729, (1975)

[84]. M. H. Grimsditch and G. D. Holah, Phys. Rev. B **12**, 4377, (1975)

[85]. N. S. Orlova, Cryst. Res. Technol. **33**, 1, (1998).

[86]. B. Tell, J. L. Shay, and H. M. Kasper, Phys. Rev. B **4**, 2463, (1971)

[87]. G. Burns and A. M. Glazer, *Space Group for Solid State Scientists*, 2nd ed. (Academic, San Diego, 1990).

[88]. S. C. Abrahams and J. L. Bernstein, J. Chem. Phys. **59**, 1625 (1973).

# CHAPTER – II

# Experimental Techniques

**This chapter constitutes the work published in**

**G. Kavitha, S.R.C. Vivek, A. Govindaraj and Chandrabhas Narayana,**

**Proceedings Indian Academy of Sciences (Chemical Science) 115, 689-694 (2003).**

This chapter deals with the fabrication of a Raman spectrometer, which has been used to carry out the Raman studies described in this thesis. The Raman spectrometer described below has been compared with the commercial setup for standard samples like Si, carbon nanotubes etc and was found to be equivalent in its functionality to the commercial one. We demonstrate here a very cost-effective way of fabricating a research grade Raman spectrometer which has tailor made collection optics taking into consideration experimental environment.

**2.1. Experimental Design of the Raman Spectrometer**

Over the past few decades Raman spectroscopy has been extensively used to study materials at ambient and extreme conditions [1-2]. Raman spectroscopy can be performed as a function of temperature and pressure [3-4]. The advent of lasers in 1960's brought Raman spectroscopy to the forefront. Over the years, there has been lot of modernization in the Raman spectrometer. The use of charge coupled device (CCD) detectors has made Raman measurements extremely simple. Raman instrumentation has under gone a lot of changes. Now a days, Raman spectrometers have single, double and triple monochromators depending on the type of study. The cost of these spectrometers has been a reason for worry. It is also been difficult to integrate Raman spectrometer with experimental environment. In this work we have designed low cost and flexible Raman spectrometers, which are based on a single monochromator and a CCD detector.

## 2.2. Experimental details

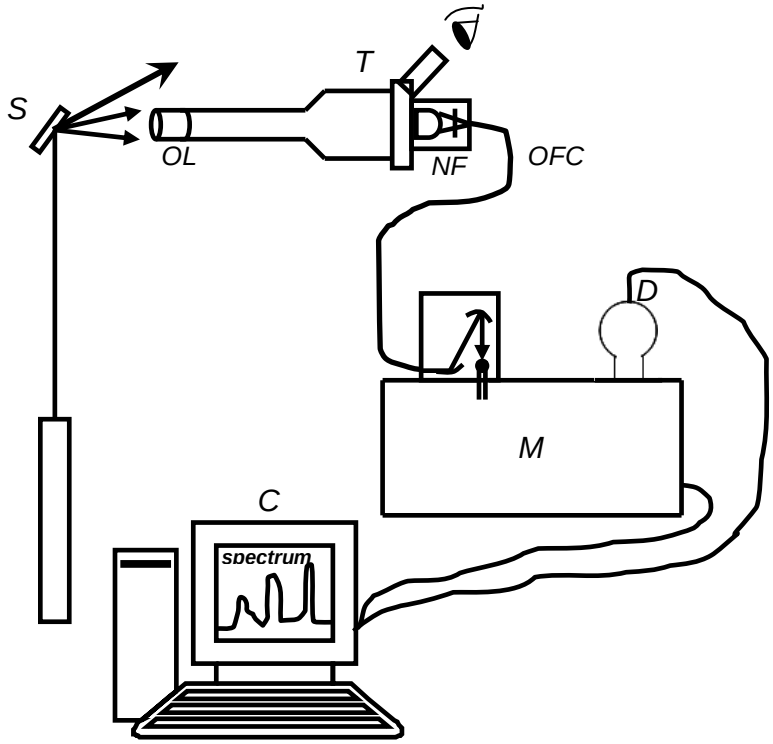


Figure 2.1. Schematic representation of the Raman spectrometer used in the present experiment. S – sample, L – laser, OL – objective lens, T – trinocular, NF – notch filter, OFC – optical fibre cable, D – CCD detector, OC – optical fibre coupling, M – monochromator and C – computer.

### 2.2.1 Excitation Source

The measurement of the absolute intensity of Raman lines enables one to compute the value of the bond polarizability derivative ($d\alpha/dq$, where q = the normal coordinate). Its value is related to the type of bond deforming. Therefore there is a linear relationship between the polarizability derivative and the bond order [5-6]. It is widely held that the detectable scattered Raman intensity is proportional to $\upsilon_0^4$, where $\upsilon_0$ is the frequency of the excitation source. So incident light source plays an important role for Raman line measurement. Depending on the application, various kinds of light sources are available for spectroscopic measurement. For most purposes, He-Ne, Argon ion and Nd-YAG lasers are accepted as being most satisfactory for Raman spectroscopy [7-8]. In this work, a solid state diode pumped vertically polarized Nd-YAG with excitation frequency of 532 nm is used. The average power on the sample was 10-30 mW. The

average life of Nd-YAG laser is 10,000 Hrs and it is very compact [9], which make it very easy to integrate with optical system. Recently we are using (GDLM-5015L, Suwtech Inc., China) with maximum power output of 18 mW.

### 2.2.2 Sample illumination

The classic method of illuminating a Raman sample is to irradiate it at a right angle to the collection which is as shown in the figure [2.1]. It is important that the direct laser light doesn't enter the collection optics to reduce the Rayleigh component. In the case of a transparent sample 90° geometry helps. In the case of opaque sample, the sample is placed at an angle such that the reflected light does not fall on the collection optics. The laser beam must be focused on to the sample and the scattered radiation collected from this point. Excitation and collection from the sample can also be accomplished by using several other geometry. Most commonly used geometries are 90° and 180° (back scattering) geometry. Most of the Raman measurements were done at 90˚ geometry [10], but for high pressure Raman experiments, we have used 180˚ geometry.

### 2.2.3. Collection optics

Simple collection optics comprises of a microscope objective, trinocular viewing port, notch filter/edge filter, focusing optics and optical fibre. In the present setup we have used 20x super long working distance (0.25 NA, 17mm$W_D$) objective and trinocular from Olympus, Japan. We have used (Keiser optics, USA) super notch filter for 532 nm excitation. A 3.3x magnifying lens at the camera port of the trinocular viewing port focuses the scattered light to the optical fiber. A 100 μm diameter and 1.5 m long multimode single optical fiber was used to collect the scattered light and illuminate the monochromator. The fiber was f-number matched with the monochromator described in the next section.

### 2.2.4. Monochromator

A monochromator is an optical device that transmits a mechanically selectable narrow band of wavelength of light or other radiation chosen from a wider range of wavelengths available at the input. The heart of our system is a Jobin Yvon

Triax 550 with triple grating. One can use other monochromators too. Single monochromators have very high throughput and stability [11]. But the down side is that one cannot use it for application very close to the laser line. The use of notch filters help in observing Raman lines at 30 $cm^{-1}$ away from Rayleigh line. But the notch filters are sensitive to humidity, temperature and detoriate. In the present experiments, we have used notch filters, but subsequently replaced it with edge filter which go up to 80 $cm^{-1}$-100 $cm^{-1}$ away from Rayleigh light.

### 2.2.5. Salient features of this Raman setup

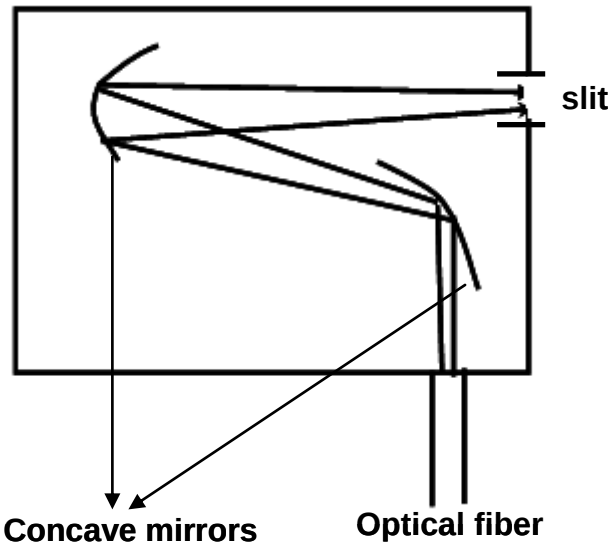


**Figure 2.2.** f-number matching of the optical fiber with monochromater

In this setup we have done two modifications from earlier versions. a) we have used concave lens (see figure 2.2) to f-number match the optical fiber. To the monochromator. The light gathering power is expressed in terms of *f* number, defined by *f* = f/d where f is focal length of the mirror and d is the mirror diameter. Smaller the *f* number, the larger is the light gathering power. It is important to match the *f* number of the optical fiber with the monochromator for efficient collection and the total light throughput to be maximum. b) we have used a tilt alignment for the notch filter. Super notch plus filters have been most successful in eliminating light very close to the incident laser frequency. The

optical density of the notch filter is high, and its spectral band width can be extremely narrow. Thus super notch plus filters are free from extraneous reflection bands and provide significantly higher laser damage thresholds. In principal, $0^o$ notch filters should have a sharp cut off for the excitation frequency. But this is not the case always, hence it is difficult to get Raman modes close to the excitation frequency. By tilting the notch filter by few degrees, one can get Raman signals as close as 10 $cm^{-1}$ to the excitation frequency with a slight loss in transmission. At present we have been routinely recording Raman signals close to 50 $cm^{-1}$. With better control over the tilt alignment one can record very low energy Raman signals.

### 2.2.6. Detection System

Detection of the Raman signal is carried out using 1024 × 256 back thinned liquid $N_2$ cooled Charge Coupled Device (CCD). CCD being a position sensitive detector provides a faster detection of a Raman spectra over a normal photo multiplier tube (PMT). Eventhough PMT is very sensitive compared to CCD, its quantum efficiency is much lower than CCD. Back thinning of CCD increases the quantum efficiency by two times. This the reason most of the Raman experimental setup use a CCD detector.

#### (i) Charged Coupled Device (CCD)

The CCD is a solid state photo detector array made up of semiconductor. Each one of photo sensitive array generates photo electrons and store them as a small charge in the pixel. Pixels are defined by a grid of three electrode gates in the X and Y directions. The voltage applied to the gate electrodes are manipulated to move the charge across the pixels to the output register at the edge of the array [12]. It is possible to address each pixel or a bunch of pixels at a time. When a CCD is used as a 2D imaging device, intensity (hence the charge) from each pixel is collected and displayed. In the Raman application since we are interested in only the frequency Vs intensity, it is a 1D spectrum; hence the pixels corresponding to same frequency are addressed together to the same register called binning.

**(ii) Backthinning**

The depletion layer of CCD (where the photoelectric effect occurs) is normally partially obscured under the electrode gates, which are formed in layers above the depletion layer which are formed in a layer above the depletion layer. This reduces its quantum efficiency. The substrate (or back) of the CCD chip can be etched down to be very thin to allow light to pass through. This helps in increasing the quantum efficiency. In this case the CCD is illuminated from the substrate side and these CCD detectors are called back thinned CCD detectors.

**(iii) Binning**

Major source of noise in CCD comes from readout noise generated by electronics while reading a pixel. So it is wise to read only the useful pixels (or illuminated pixels). In a CCD used for Raman spectroscopy, the spatial information is important only in the frequency direction and not in the intensity direction. In such a situation, a linear array CCD would provide the same information as a 2D CCD. So a process of binning is used along the intensity direction. Here the charges of all the pixels related to same frequency are accumulated to one register. This process is called binning. In Raman experiments, to increase signal to noise (S/N) ratio, one bins only the illuminated pixels and ignore all other pixels.

## 2.3. High Pressure Techniques

Pressure is force per unit area. The force could be time independent or instantaneous. Hence there are tow ways to study materials under pressure [13].

1. **Static pressure –** A constant force is applied and the system is in equilibrium, hence the temperature is constant. The pressure is changed by changing the applied force. The maximum pressure depends on the container characteristics. Eg., Anvil cells and piston-cylinder assembly.
2. **Dynamic pressure –** here the force is applied as a pulse, and the pressure builds

up in the material with time. So the system is not in equilibrium, hence the temperature rises. Here the material itself acts as a pressure transmitting medium and this experiment happens in nanoseconds. Eg., shock loading using gas gun.

**Diamond Anvil Cell (DAC)**

DAC uses gem quality diamonds to transmit pressure to the sample. Diamond, being recognized as the hardest and least compressible material, has the important property of being transparent to the most of the spectrum of electromagnetic radiation, including $\gamma$ - ray, X – ray , portion of UV-visible and most of the IR region.

(a) (b)

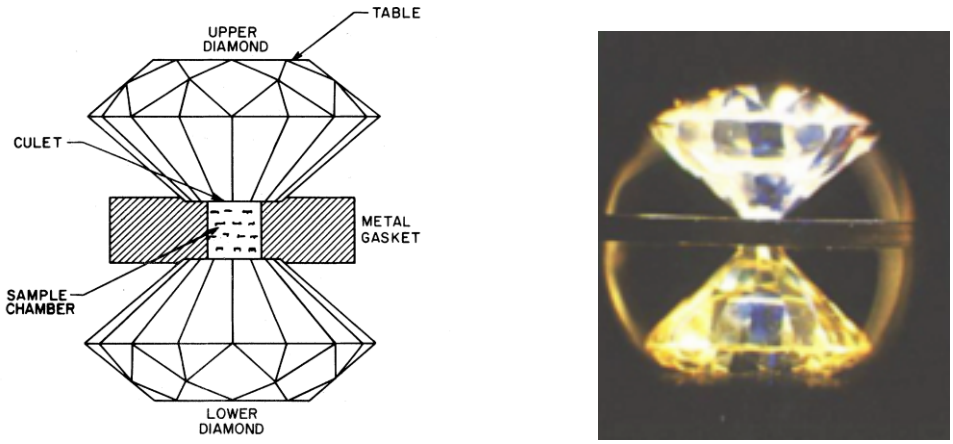


**Figure 2.3.** a) Schematic cross section view of Diamond Anvil, b) Photograph of Diamond anvil

DAC is based upon the opposed – diamond configuration (see figure 2.3(a&b)), in which a sample is placed between the polished culets of two diamonds and is contained on the sides by a metal gasket (see figure 2.2 (a-b)). In this configuration, very little force is required to create extremely large pressures in the sample chamber. The different kinds in the design of the DAC arise mostly from the differences in the mechanisms for generating force and Diamond anvil alignment. According to that the DAC are classified as follows [14-21].

1. NBS Cell
2. Basset Cell

3. Mao – Bell Cell
4. Syassen – Holzapfel Cell
5. Merrill – basset Cell

We have used a Mao-bell type DAC due to the ease to apply pressure, as the load is produced by the set of levers used to force the anvils together.

### 2.3.2. Mao – Bell Diamond Anvil Cell

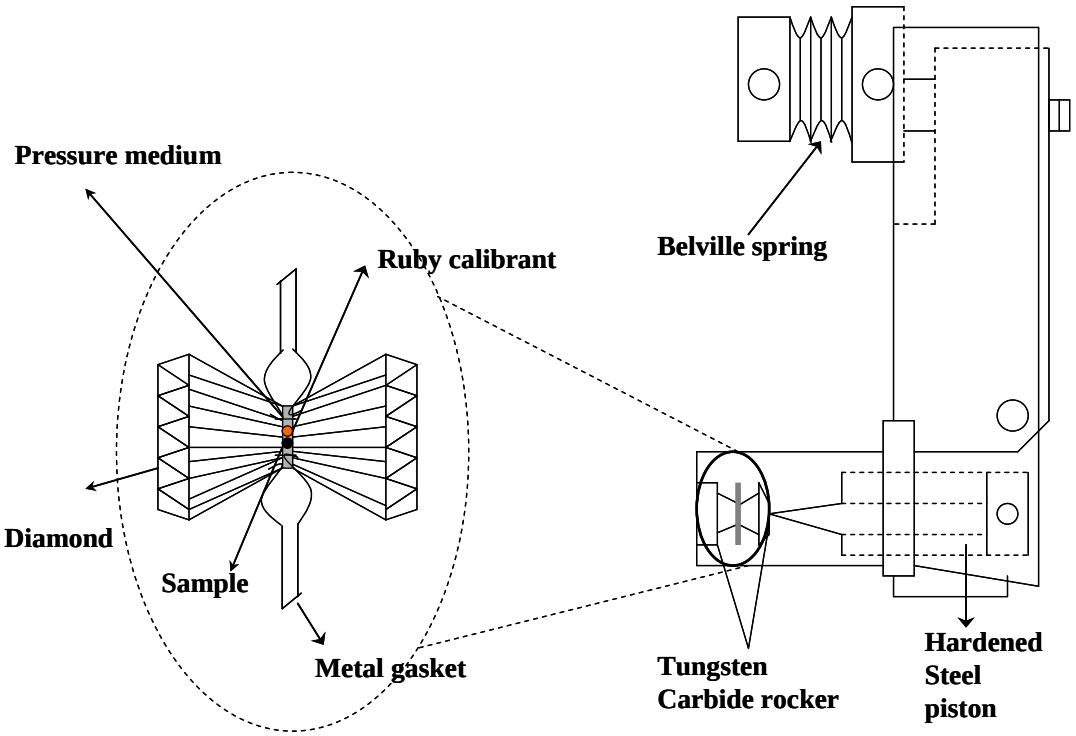


**Figure 2.4.** Schematic representation of Mao-Bell Diamond Anvil Cell

Figure 2.4. shows the schematic of the Mao-Bell DAC used in this thesis. The main parts are, a) Piston and matching cylinder assembly, b) Diamonds mounted on a tungsten carbide rockers, c) Hardened stainless steel lever arm based as a nut cracker or scissor mechanism, d) Hardened stainless steel gaskets to hold sample and e) a lead screw with Belleville spring to clamp the levers.

**(i) Diamond**

The first step is selecting the appropriate diamond stone for DAC. The four important things to be noted are cut, color, clarity and carat. Gem quality, brilliant cut diamond stones are generally used as anvils. For experimental pressure below 30 GPa, the culet of the diamond has a flat face ranges from 500 – 600 μm and further high pressure is achieved by reducing the culet size. The purest type II diamond is transparent to all electromagnetic radiation and through out the IR region. How ever it does not sustain for ultra high pressure due to defects while it is formed. Hence the stone containing evenly dispersed Nitrogen platelet impurity (type I) is commonly used. but this has tremendous absorption in the mid IR region and has fluorescence in the visible region [14]. For Raman spectroscopic measurement, the fluorescence from the diamond is very important and should be low.

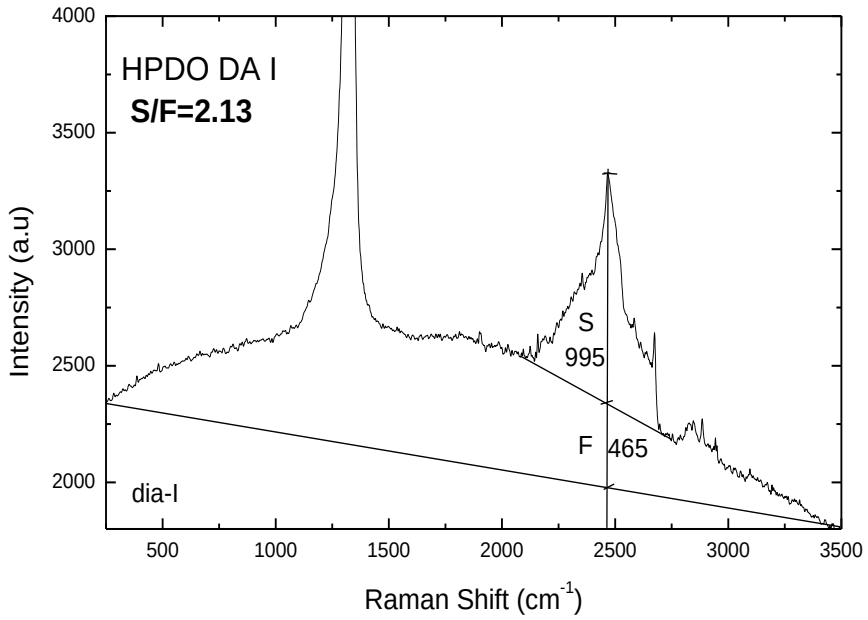


**Figure2.5.** Raman Spectrum of Diamond used in our experiments. The fluorescence (F) to the second order Raman signal (S) ratio is found to be 2.1

The combination of CVD and high pressure/high temperature technique has yielded gem quality synthetic diamond with low fluorescence in visible region up to 300 GPa and above 370 GPa with red excitation. A quality factor used in testing of the diamonds is the ratio of the fluorescence (F) to the second order Raman signal (S) of the diamonds for

any given excitation. Figure 2.5 shows the S/F ratio of the diamonds used and its Raman spectrum. The shape of the diamond anvil is important for achieving high pressures. With circular culet diamond, one can achieve the pressure range nearly 60 GPa. The beveled help to achieve multi mega bar pressures as it avoids build up of stress.

**(ii) Rockers to align the diamond anvils**

Tungsten Carbide and Boron Carbide materials are usually used for mounting the diamond for the high pressure experiments. These metallic plates are provided with tapered holes. The culet of the diamond is centered on the tapered hole of the backing plate. The top surface of the plate is polished to a mirror finish well before placing diamond. The non- uniformity in the surface causes the glue to flow between the diamond and backing plates leading to breakage of diamond well before the highest pressure. The diamonds are generally glued using high strength epoxy like 409.

**(iii) Diamond alignment**

To achieve high pressures, the diamonds should be mirror images of each other. For the perfect alignment of DAC, the following steps are strictly adopted. The parallelism of diamond anvils are matched by translation of the rockers along the X and Y axes. The piston is inserted in to the cylinder, and this assembly rested on the V – block, the diamonds are viewed under optical microscope along the four directions perpendicular to the cylinder axis through the hole in the wall of the cylinder. The gap between the anvils is reduced without touching to estimate the off set of the culets along the X and Y directions. XY alignment is done using the set screws through the ports in the cylinder wall. The process is repeated until the XY alignment is achieved. The angular orientation of the culet is adjusted by the screws on the top of the cylinder. The final alignment obtained by one of the two following methods [14]

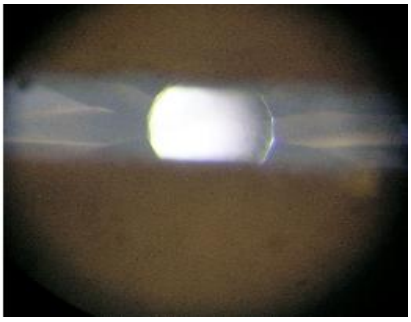

**Figure 2.6.** One fringe condition of DAC using white light illumination

a. silver iodide technique
b. light fringe technique

We have adapted light fringe technique to obtain perfect alignment of DAC. Care is taken not to bump the diamonds against each other before touching the culet. Using an optical microscope, white light is passed through the culet and the interference light fringe pattern was observed through the centre of the cylinder. If one observes stripes or colored fringes The alignment of the DAC is not good. Using tapping screws on the top of the cylinder, one can obtain the one – fringe condition as shown in figure 2.6; and the anvils are perfectly aligned.

**(iv) Gasket**

A gasket is a mechanical seal that serves to fill the space between two objects, generally to prevent leakage between the two objects while under compression. The gaskets are commonly produced by cutting from sheet materials, such as gasket paper, rubber, silicone, metal feet, fiberglass or a plastic polymer. One of the most desirable properties of an effective gasket is the ability to withstand high compressive loads. The metals are highly malleable. They can be thinned to a few μm without breaking or tearing. Suitable gasket materials are stainless steel, martensitic tool – steel, inconel, tungsten, rhenium. It is necessary to pre-indent the gasket before loading sample in to the

DAC. Pre-indentation of the gasket will prevent the premature failure of the diamonds and reduces the hole deformation during experiment. Gaskets not only certain but also play an important role for building high pressure in the cell.

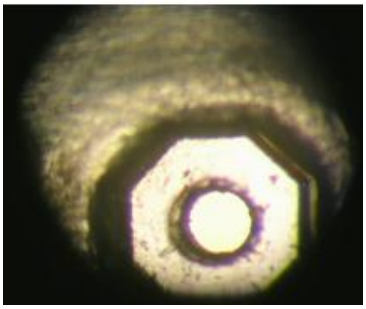

**Figure 2.7.** Preindented stainless steel gasket used in our experiment

The pre-indenting pressure thickness depends on the maximum pressure intended in an experiment and as the gasket deforms plastically, extrudes outwards forming a supporting ring. The initial thickness of the gasket is generally 250 μm which will be pre-indented to a thickness 100 μm for a pressure of 20 GPa to be achieved. After pre– indentation, using micro drilling equipment with a aid of miniature drill bit, a hole can be drilled at the centre of the pre–indentation area. Figure 2.7 shows a pre-indented gasket with a 100 μm hole drilled in it. There is an equal and opposite force acting inwards between gasket material and the surface of the culet. This is the indication of the stability of the gasket. If the thickness of the gasket is sufficiently small, the destabilizing outward force is smaller than inward stabilizing force, as a result shrinkage of the gasket hole. On the other hand, if the thickness of gasket is very large, consequently the outward destabilizing force will be larger than the inward stabilizing force and hence elongation of the gasket hole. The maximum pressure which can be attained by the experiment will be determined by shear strength of material, the pre– indented thickness, culet size and size of the drilled hole.

**(v) Pressure transmitting medium**

Pressure transmitting medium helps in achieving hydrostatic pressure. Depending on the desired pressure range and the reactivity of the sample, different

pressure media are used. Eg., silicon oil, $N_2$, Ar, ethanol – methanol mixture etc.,). To achieve hydrostatic pressure (zero shear stress) on the sample, it has to immersed in a medium. The use of an encapsulating fluid as a pressure transmitting medium generally fulfills this requirement. It has been shown that many pure liquids and liquid mixtures slowly vitrify rather than crystallize with pressure. Some liquids remains hydrostatic to pressures well over 3 GPa. Table 2.1 shows the various medium used to produce hydrostatic pressure and their maximum range. It is common to use inert gases like Ne and Ar but require special handling. Ethanol, methanol mixture gives hydrostatic pressure up to 11 GPa and with a little amount of water can go up to 15 GPa. These liquids are easy to handle and are most commonly used for experiments <20 GPa.

**TABLE 2.1.** Maintaining hydrostatic conditions in systems in high pressure involves the selection of an appropriate fluids [22-30].

| **Pressure medium** | **ratio** | **Hydrostaticity at room temperature (GPa)** |
|---|---|---|
| Methanol : Ethanol : water | 16:3:1 | 14.5 |
| Methanol : Ethanol | 4:1 | 10.4 |
| Methanol | | 8.6 |
| Pentane : isopentane | 1:1 | 7 |
| Silver chloride | | >7 |
| Water (ice VII) | | >7 |
| Sodium chloride | | >7 |
| Hydrogen | | 177 |
| Helium | | 60 - 70 |
| Neon | | 16 |
| Argon | | 9 |
| Xenon | | 55 |
| Nitrogen | | 13 |

**(vi) Pressure sensor**

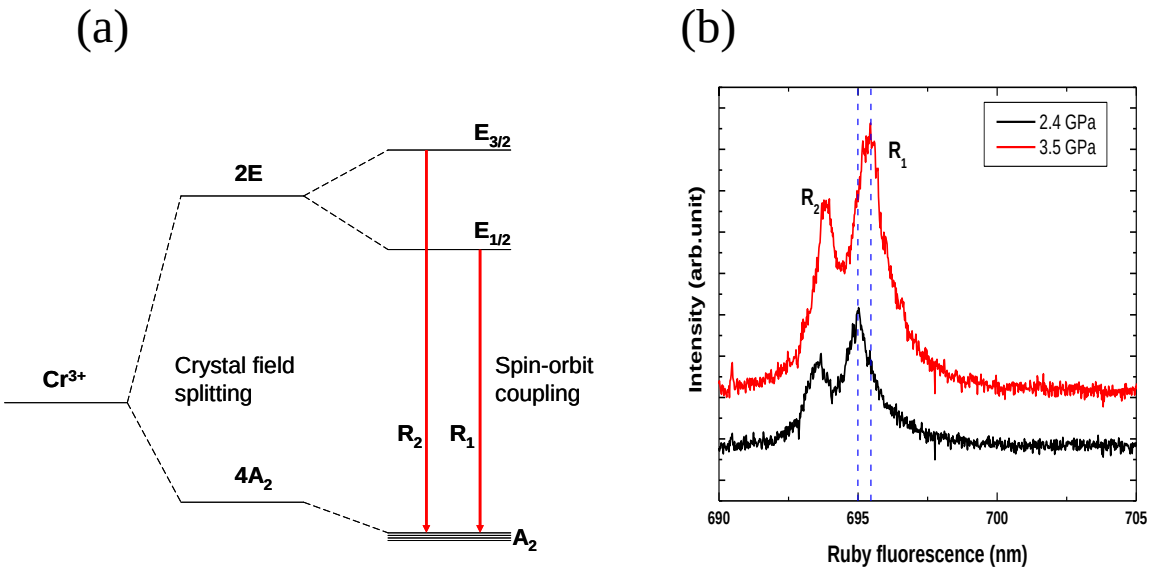


**Figure 2.8.** Schematic representation of a) Ruby fluorescence, b) Ruby $R_1$ line shift with different pressures.

In static high pressure work using diamond anvils, the ruby fluorescence method is the most widely used pressure sensor [31]. Fluorescence from ruby crystals is known to exhibit pressure dependence. $Al_2O_3$ with 1-3% of $Cr^{3+}$ is named as ruby due to its bright red color. In ruby, $Cr^{3+}$ occupies one of the $Al^{3+}$ sites ($D_{3d}$) but is displaced along the c-axis due to its slightly different size, there by assuming $C_{3v}$ site symmetry. The cubic crystal fields splits the state of the $Cr^{3+}$ ion into doubly degenerate state (2E) and a non-degenerate ground state ($4A_2$). Spin-orbit coupling lifts the degeneracy of the 2E states into $E_{3/2}$ and $E_{1/2}$ states separated by ~ 30 $cm^{-1}$ as shown in figure 2.8(a). Electronic transitions can take place between these states and the ground state. Ruby fluorescence has two strong lines called the $R_1$ and $R_2$ lines at 694.3 and 692.9 nm. With pressure, the fluorescence lines shift and have been well characterized to given in-situ pressure. The two R-lines shift equally and no change in $R_1 - R_2$ splitting occurs under hydrostatic pressure (see figure 2.8(b)). The pressure relationship is given by

$$\mathbf{P\ (GPa) = 1904/B[\{1+(\Delta\lambda/694.24)\}^{B} - 1]}$$

where $\Delta\lambda$ is the shift in the ruby $R_1$ line wavelength in Å, B – 7.665 and 5 for quasi hydrostatic and non–hydrostatic conditions respectively [32-34]. The extensive

broadening of the spectra from a single ruby chip in static measurements indicates a substantial non – uniformity of stress over the dimension of the ruby chip. We have used ruby fluorescence method for determining the pressure of the samples loaded in the diamond anvil cell.

**Experimental setup for Brillouin spectroscopy**

In Brillouin experiments, the Fabry-Perrot interferometer has been instrument of choice [35-36]. However, conventional Fabry Perot interferometers do not achieve the contrast needed to resolve the weak Brillouin doublets. Sandercock first showed that the contrast can be significantly improved by multipassing [37-38].

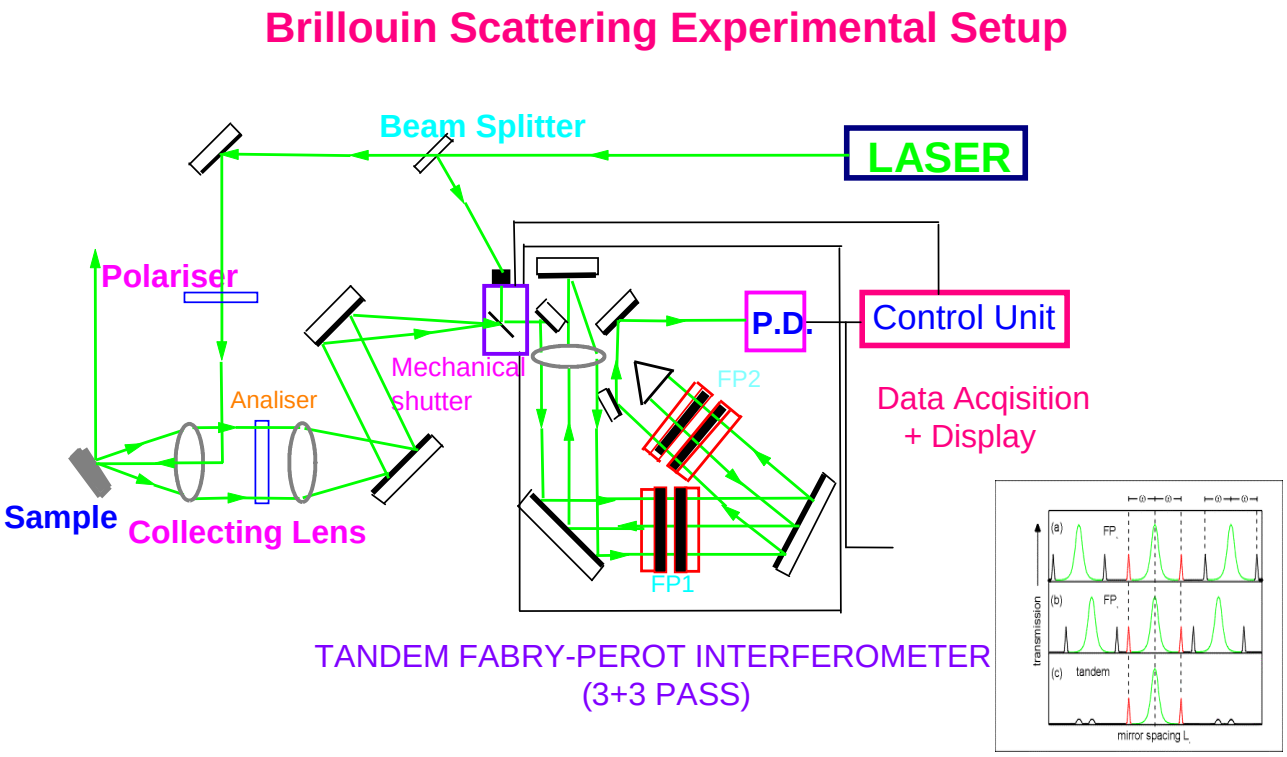


**Figure2.9**. Schematic of Brillouin Experimental setup with back scattering geometry

The usefulness of coupling two synchronized Fabry-Perot, thus avoiding the overlapping of higher orders with central orders was also recognized for increasing the free spectral range. Figure 2.9 shows the modern Tandem Fabry-Perot interferometer which is used in the experiments described in this thesis.

### 2.4.1. Fabry-Perot Interferometer

The Fabry-Perot interferometer is an optical instrument which uses multiple-beam interference (see figure 2.9). This interferometer makes use of multiple reflections between two closely spaced partially silvered surfaces. Part of the light is transmitted each time the light reaches the second surface, resulting in multiple offset beams which can interfere with each other [39-41]. The large number of interfering rays produces an interferometer with extremely high resolution, somewhat like the multiple slits of a diffraction grating increase its resolution.

### 2.4.2. Principles of Fabry – Perot interferometer

A Fabry – Perot interferometer (FP) is used for high resolution spectroscopy where a resolution of MHz to GHz is required. The FP consists of two plane mirrors mounted accurately parallel to one another, with an optical spacing $L_1$ between them. For a given spacing $L_1$ the interferometer will transmit only certain wavelengths $\lambda$ as determined by

$$T = \tau_0 / [1+ (4F^2/\pi^2)\sin^2(2\pi L_1/\lambda)] \text{---------- (2.1)}$$

where $\tau_0$ (<1) is the maximum possible transmission determined by losses in the system, and F, the finesse, is a quality factor depending primarily on the mirror reflectivity and flatness.

**(i) Finesse**

It is customary to define a numerical value which characterizes the width – or better the sharpness – of the maxima. This number is called the *Finesse* of an interferometer and defined as the ratio of peak distance to peak halfwidth (see figure 2.10).

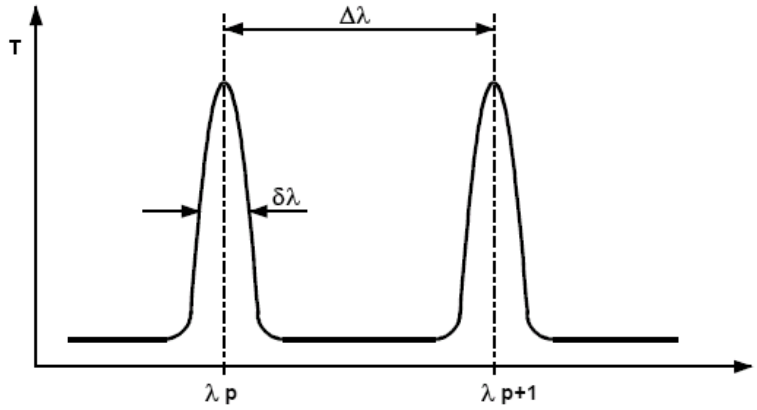


**Figure 2.10.** Spectral representation of Finesse

Equation 2.1 shows that only those wavelengths satisfying

$$L1 = ½\ p\ \lambda \text{ ----------(2.2)}$$

for integral values of p, will be transmitted. This is illustrated in figure 2.10. The Finesse F is defined as the ratio of the spacing between successive transmitted wavelengths $\Delta\lambda$ (Free spectral Range – (FSR)) and the width $\delta\lambda$ of a given transmission peak by

$$F = \Delta\lambda/\delta\lambda \text{ ----------(2.3)}$$

By varying the spacing $L_1$ so as to scan the light intensity at different wavelengths, the FP can be used as a spectrometer. However it is immediately apparent that the measured intensity at a given spacing is the sum of the intensities at all wavelengths satisfying condition in Eq. 2.2. An unambiguous interpretation of the spectrum is thus impossible unless it is known a priori that the spectrum of the light lies entirely within a wavelength spread < $\Delta\lambda$. It is true that since

$$\Delta\lambda = \lambda^2/2L_1 \text{----------(2.4)}$$

one may make $\Delta\lambda$ arbitrarily large by decreasing $L_1$. However $\delta\lambda$ increases proportional to $\Delta\lambda$ and so the resolution decreases. In fact equation 2.3 shows that the ratio between FSR ($\Delta\lambda$) and the resolution $\delta\lambda$ is just the finesse F. In practice F cannot be made much greater than about 100 due to limitations on the quality of mirror substrates and coatings. The relationship between FSR and resolution is thus fixed within limits determined by the achievable values of F.

**(ii) Contrast**

To rate the suppression between maxima, the *Contrast* is defined as ratio of peak height to the minimum intensity. The transmission minimum at $\delta=\pi$ and at equivalent phases define a Contrast value C of

$$C = Q_R + 1 \text{ ------- } (2.5)$$

where $Q_R$ -4R / [1-$R^2$], the quality factor for reflectivity R.

**(iii) Resolution**

The resolution of an optical instrument is defined by the bandwidth of a spectral line, i. e. the broadening imposed on the line by the instrument. We have to calculate what spectral line width $\Delta\lambda$ is equivalent to this instrumental line width. we assume normal incidence. At the maxima, the phase difference $\delta$ is defined by

$$\delta = 2kdn = [4\pi/\lambda]dn = 2N \text{ ----------(2.6)}$$

The line width can be expressed by finesse

$$\delta\lambda = 2\pi/F\text{----------(2.7)}$$

and equated with spectral line width

$$\delta\lambda = 2\pi/F = [4\pi/\lambda]dn – [4\pi/\lambda+\Delta\lambda]dn\text{----------(2.8)}$$

Thus the resolving power of the instrument is defined by the product of the finesse F and the interference order N

$$\lambda / \Delta\lambda = [2\ F/\lambda]dn = F.\ N\text{----------(2.9)}$$

Eq. 2.9 shows that, with a finesse of 100, the resolving power of a 100 mm wide grating is exceeded for dn > 0:5 mm. Using air-spaced Fabry-Perot interferometers, values for $L_1$ up to more than 10 mm can be easily achieved. The resolution then expressed as frequency is around 10 MHz.

### 2.4.3. Tandem Interferometry

There exists a means of increasing the FSR at a fixed resolution by the use of two FP's in series [42]. The most useful arrangement is a vernier system in which the spacing of the second interferometer $L_2$ is close to $L_1$. To overcome FSR problem, a

similar approach as that already discussed uses two different interferometers with different spectral ranges in conjunction, one for coarse, one for finer resolution.

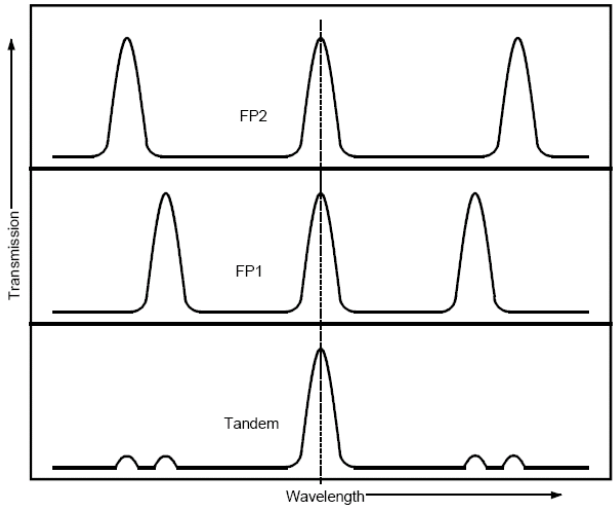


**Figure 2.11.** Elimination of neighboring interference orders in a tandem arrangement of two unequal interferometers.

The wavelengths transmitted by the combination must simultaneously satisfy:

$$L_1 = ½\ p\lambda \text{ and } L_2 = ½\ q\lambda \text{ ----------(2.10)}$$

for integral values of p and q.

If the spacing $L_1$ and $L_2$ are independently set so as to transmit a given wavelength $\lambda$ then the combined transmission for light passing successively through both FP1 and FP2 will be illustrated in figure 2.12. The neighboring transmission peaks do not coincide - only after several times the FSR of FP1 do the transmission peaks coincide again. Small "ghosts" of the intervening transmission peaks remain since the transmission of either interferometer as shown in equation 2.1 never falls exactly to zero. The FSR of the tandem system is thus increased by a considerable factor over that of the single interferometer, while the resolution $\delta\lambda$ remains similar. In order that the first ghost is not too obtrusive one should chose $L_1$ and $L_2$ such that

$$F > L_1/(L_1 - L_2)$$

A good practical value for $L_2 / L_1$ is about 0.95.

To use the tandem interferometer system as a spectrometer, it is necessary to scan the two interferometers synchronously, by simultaneously changing the spacings $L_1$ and $L_2$. It is clear from equations 2.2 and 2.5 that to scan a given wavelength increment, the changes $\delta L_1$ and $\delta L_2$ must satisfy

$$\delta L_1/\delta L_2 = L_1/L_2 \text{ ----------(2.11)}$$

The magnitudes of $\delta L_1$ and $\delta L_2$ are typically 1 to a few μm. The only previously known method of satisfying Equation 2.6 was by use of pressure scanning. Remembering that L is the optical spacing of the mirrors (i.e. the spacing t multiplied by the refractive index n of the gas between the mirrors) one may change L by changing the refractive index of the gas through a pressure change. Since

$$L_1 = nt_1 \text{ and } L_2 = nt_2$$

we see that Eq 2.11 will be satisfied if the refractive index change is the same for both interferometers. The limitation of the method lies in the scanning range which is limited by the achievable refractive index change. Using air, a pressure change of 1 atmosphere will change L by only 3 parts in 104, producing the same relative change in the transmitted wavelengths. Where much larger scans are required, the associated large pressure changes make the system impracticable.

### 2.4.4. A practical design of scanning tandem FP

Using the new design of interferometer, based on the concept of a scanning stage [43-45], it is now possible to combine two interferometers on the single scanning stage to obtain both statically and dynamically stable synchronization.

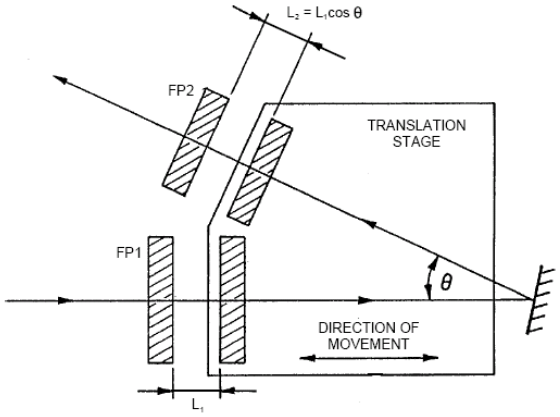


**Figure 2.12.** A translation stage designed to automatically synchronize the scans of two tandem interferometers.

The principle of the tandem scan is seen in Fig 2.12. The first interferometer FP1 is arranged to lie in the direction of the translation stage movement. One mirror sits on the translation stage, the other on a separate angular orientation device. The second interferometer FP2 lies with its axis at an angle θ to the scan direction. One mirror is mounted on the translation stage in close proximity to the mirror of FP1, the second mirror on an angular orientation device which can also allow a small translation of the mirror for adjustment purposes. The relative spacing of the mirrors are set so that a movement of the translation stage to the left would bring both sets of mirrors into simultaneous contact. A movement of the translation stage to the right sets the spacing to $L_1$ and $L_1$ Cos θ. A scan $\delta L_1$ of the translation stage produces a change of spacing $\delta L_1$ in FP1 and $\delta L_1$ Cos θ in FP2. In other words equation 2.11 is satisfied and so the two interferometers scan synchronously. An upper limit on the length of the scan is imposed by the shear displacement of the mirrors of FP2 - after a scan of more than D/Sinθ (mirror diameter D) the mirrors would no longer overlap. A scan of several cms is easily possible for normal mirror diameters (3-5 cms). Since the scan lengths in practice rarely exceeds 3 μm this large range should rather be understood as the range over which $L_1$ may be adjusted without requiring a lateral repositioning of one of the mirrors of FP2. The main features of the system are:- complete dynamic synchronization over a large scanning range and good static synchronization due to the compact design which enables both interferometers to share the same environment [46].

### 2.4.5. Experimental details of low temperature Brillouin scattering

Brillouin scattering measurements were carried out using 180° back scattering geometry with an incident angle of 45° with respect to surface normal. For temperature dependent studies the sample was mounted in a closed – cycle Helium Cryostat (CTI Cryogenic, USA). We used a temperature controller (Conductus: model LTC-10, USA) with silicon diode sensor. To determine the actual temperature of the sample the thermal sensor was kept in contact with the sample on the copper sample holder. Temperature stability with in ± 1 K was achieved during the measurement. Spectra have been recorded with the temperature range from 20 K – 320 K. To perform

Brillouin scattering, single mode vertically polarized Nd – YAG laser operated at $\lambda$ = 532 nm with 50 mW power is used as a light source. The scattered light was analyzed by using JRS Scientific instruments (3+3) pass tandem Fabry–Perot interferometer equipped with a photo – avalanche diode detector which has finesse more than 100. Spectra reported in this work were recorded using a multi channel scaler with 512 channels and the typical accumulations of 500 – 2000 passes were done with 0.768 sec per pass. For polarization study, a polarization rotator and an analyzer were put on the laser path and before the entrance slit of the spectrometer respectively. The line-shape parameters-peak frequency, and area under the curve were extracted by a non-linear least square fitting of the data with a Lorentzian function, along with an appropriate background.

### 2.5. Source of the samples used

The spectroscopic grade alkanes and perfluoroalkanes have been obtained from Sigma Aldrich and used without further purifications. $PbWO_4$ crystal was grown in AT&T Bell laboratories, New Jersey. Large single crystals were grown by Czochralski technique [47]. $BaWO_4$ was made using standard solid state route by BARC group. Barium carbonate and tungsten oxide are mixed in their stochiometric ratios and are finely ground together and then heated in a furnace. $AgGaS_2$ crystal was grown in AT&T Bell laboratories, NewJersey.

### 2.6. Bibiliography


[1]. Goncharov. A.F, Struzhkin. V. V, Somayazulu. M; Hemley. R. J, *Phys. Rev. Lett.* **83** (1999) 1998-2001.

[2]. Kenneth G. Brown, Ellen Bicknell-Brown, Meriem Ladjadj, *J. Phys. Chem.* **91**, 3436, (1987).

[3]. Deb. S. K, Rekha. M. A, Roy. A. P. Vijayakumar. V, Meenakshi. S, Godwal. B.K, Phys. Rev. B. **47**, 11491 (1993).

[4]. Marcelo campos-valle'i're and madeleine rey-lafon, *J. Mol. Struc*, **101** 23, (1983).

[5]. Long D.A. The Raman Effect: A unified Treatmetn of the Theory of Raman Scattering by Molecules, John Wiley & Sons Ltd, 2002.

[6]. Yoshino T, Bernstein H. J., *Spectrochim. Acra*, **14**, 127 (1959).

[7]. Evans M. V., Hard T. M., Murphy W. F., *J. Opt. SOC. Amer,* **56**,1638, (1966).

[8]. R. C. C. Leite and S. P. *S.* Porto, *J. Opt. SOC. Amer.*, **54**,981, (1964).

[9].Wolfgang Demtröder, "Laser Spectroscopy Basic Concepts and Instrumentation" 3rd Edition Springer-Verlag Berlin Heidelberg New York, 2002.

[10]. *G.* F. Bailey, S. Kint, and 3. R., Scherer, *Anal. Chem.*, **39**, 1040, (1 967).

[11]. D. Landon and S. P. S. Porto, *Appl. Opt.,* 4,762 (1965).

[12]. Kuzmany. H, " Solid-State Spectroscopy-An Intoduction, Springer-Verlag Berlin Heidelberg New York, 1998.

[13]. Chidambaram. R, Sharma. S. M, Bull. Mater. Sci. **22**, 153, (1999).

[14] Jayaraman.A, Rev. Mod. Phys. **55**, 65, (1983).

[15]. Hazen R. M, Downs. R. T, " High Temperature and High Pressure Crystal Chemsitry", Reviews in Mineralogy and Geochemistry Vol **41** (2000).

[16]. Ermets. M. I, High Pressure Experimental methods", Oxford university press, Oxford, New York, (1996).

[17]. Xu. J, Yen. J, Wang.Y, Huang. E, High.Pressure. Res. **15**, 127, (1994).

[18]. Mao. H. K, Xu. J, Hemley. R. J, Proc. International Workshop on Crystallography at high pressures abstracts 36, (2001).

[19]. Patterson. J. R, Catledge. S. A, Vohra. Y. K, Akella. J, Weir. S.T, Phys. Rev. Lett. **85**, 5364, (2000).

[20]. Utsaumi. W, Funakoshi. K, Shimomura. O, The review of high pressure science and technology (ed) Nakahara. M, AIRAPT – 16, (Kyoto: Nakanishi) **7**, 484, (1998).

[21]. Klotz. S, Besson. J. M, Hamel. G, Nelmes. R. J, Marshall.W. G, Loveday. J. S, Braden. M, The review of High Pressure Science and Technology, Nakahara. M (ed.) AIRAPT-16, (Kyoto: Nakanishi) **7**, 217, (1998).

[22]. Angel. R.J, " High temperature and high pressure crystal chemistry", Reviews in Mineralogy and Geochemistry" (ed. Hazen R. M and Downs. R. T,) Vol. **41**, (2000).

[23]. Piermarini. G. J, Block. S, Barnett. J. D, J. Appl. Phys. **44**, 5377 (1973).

[24]. Sidorov. V. A, Tsiok. O. B, Fizika I Tekhnika Vysokikh Davlenii **34,** 74, (1991)

[25]. Barnett. J.D, Bosco. C.D, J. Appl. Phys. **40**, 3144, (1969).

[26]. Fujishiro. I, Piermarini. G. J, Block. S Munro. R. G, In high pressure research and industry Proc.8$^{th}$ AIRAPT conf. Uppsala, Backman C. M., Johannison T., Tegner

L.. (eds.) p608 (1981).

[27]. Mao. H. K, Bell. B. M, Carnegie Inst. Wash Yrbk **80**, 404, (1991).

[28]. Liebenberg. A, Phys. Lett. A **73**, 74, (1979).

[29]. Asaumi. K, Ruoff. A. L, Phys. Rev. B **33**, 5633 (1986).

[30]. Le Sar. R, Ekberg. S. S, Jones. L. H, Mills. R. L, Schwalbe. L. A, Schiferel. D, Sol. Stat. Comm. **32**, 131, (1979).

[31]. Forman. R. A, Piermarini. G. J, Barnett. J. D, Block. S, Science, **176**, 284, (1972).

[32]. Mao. H.K, Xu. J. A, Bell. P. M, J. Geo. Phys. Res. **B91**, 4673, (1986).

[33]. Mao. H.K, Bell. P. M, Science, **102**, 1145, (1978).

[34]. Bell. P. M,Xu. J. A, Mao. H.K, In shock waves in condensed matter, Y.M. Gupta, Plenum press, New York, p125 (1986).

[35]. Lindsay S. M; Anderson M.W; Sandercock J.R; Rev. Sci. Instrum. **52**, 1478,(1981).

[36]. Hercher. M, Appl. Opt. **7**, 951, (1968).

[37]. Sandercock. J. R, U.S. Patent, 4,014,614 (1977).

[38]. Vacher. R, Sussner. H, Schickfuss. M.V, Rev.Sci.Instrum. **51**, 288, (1980).

[39]. Sandercock. J. R: In 2nd Int. Conf. on Light Scattering in Solids, ed, by M. Balkanski (Flammarion, Paris 1971) p170.

[40]. Lindsay.S.M, Shepard. I.W, J.Phys.E, **10**, 150 (1977).

[41]. Roychoudhuri. C, Hercher. M, Appl.Opt. **16**, 2514, (1977).

[42]. Cannell. D.S, Benedek. G. B, Phys.Rev. Lett. **25**, 1157, (1970).

[43]. Jones.R.V, Young. I.R, J.Sci.Instrum. **33**, 11, (1956).

[44]. Bradley. D.J, J.Sci.Instrum. **39**, 41, (1962).

[45]. Gutstafsson, S. E, Khan. M.N, Van Eijk. J, J.Phys.E. **12**, 1100, (1979).

[46]. Sandercock. J. R, U.S. Patent, 4,225,236 (1980).

[47]. Jayaraman A; Batlogg B; VanUitert L.G; Phys. Rev. B. **31**, 5423 (1985).

# CHAPTER-III

# High Pressure Raman Studies on Medium chain Hydrocarbons

**This chapter constitutes the work published in**

1) **Journal of Physical Chemistry B 110, 8777-8781 (2006).**
2) **Journal of Physical Chemistry B 111, 7003-7008 (2007).**
3) **Journal of Physical Chemistry B 111, 14130-14135 (2007).**

### 3.1. Motivation

Long- and short-chain alkanes have various applications in industry, such as use as lubricants or as solvents. Since an alkyl group is present in several complex molecular systems [1] and forms a crucial component in systems ranging from membranes to micelles and self-assembled mono-layers, [2] a study of the phase diagram of linear and branched alkanes helps in the understanding of the complex phenomena in these systems. Liquid *n*-heptane mixed with isooctane has the anti-knocking properties of engine fuels [3]. On the whole, *n*-pentane has a wide variety of applications [4]. It is one of the main components in petroleum [5] and a solvent in reaction mixtures as well as an extracting agent [6-8]. It has been used as hydrostatic pressure medium in high-pressure experiments [9-11]. The electron mobilities of methane and ethane differ by a factor of 500 even though the difference in the number of atoms is only 3 (one carbon and two hydrogen) [12]. The excess electron mobility in hydrocarbons depends on its structure [13]. This mobility and chain–ordering of the hydrocarbons are useful in examining the perturbation effects of cholesterol or proteins when present within the lipid layer [14]. n-hexane and n-pentane account for most of the normal paraffins found in petroleum. High-pressure studies of n-hexane and n-pentane would then give an insight into the environment of crude oil deep inside the earth [14]. It would also help in understanding the generation and retention of petroleum in geological structure. Other applications of n–hexane are: as an extracting agent, solvent and reaction medium in food chemistry [15-19]. Hence, it is important to understand its conformation, phase diagram, and molecular arrangement under pressure.

In general, the n-alkanes exhibit different kinds of conformational isomers in liquid state. The conformation of the *n*-alkanes in liquids has been actively investigated. In the crystalline phase, linear alkanes exhibit interesting rotator phases, which have been shown using neutron scattering [20] and computer simulations [21]. There has been considerable interest in the structure and dynamics of crystalline *n*-alkanes, which have been recently studied [22-26]. High-pressure infrared (IR) spectroscopic investigations carried out up to a pressure of 7 GPa revealed that *n*-heptane undergoes a liquid to solid transition at ~1.2-1.5 GPa and a possible solid-solid transition at ~3 GPa [25]. Recent molecular dynamic (MD) simulations on *n*-heptane have confirmed the existence of the

liquid to solid transition at ~1.2-1.5 GPa, but could not show any evidence of solid-solid transition in their studies up to 7 GPa [26]. The MD simulations revealed a dynamic arrest of the rotation of the methyl end groups and extensive changes in the environment around the end groups of *n*-heptane as a function of pressure in the solid phase [26]. In addition to this, *n*-pentane is also a model for all kinds of linear alkanes, as it possesses the basic molecular conformational units like all-trans (TT), single gauche (TG), and double gauche (GG) conformers [27]. Recent high-pressure Raman studies up to 4.77 GPa by Qiao and Zheng [4] and infrared studies up to 2.8 GPa by Kato and Taniguchi [27] showed the existence of a liquid-solid transition around 2.5 GPa. n-hexane undergoes a liquid to solid transition around 1.4 GPa and has been reported earlier [28].

However, there have been no studies carried out to look at transition in the solid n-alkanes. The cumulative effect of the dynamic arrest of the rotation and changes in the environment around the methyl end group could introduce a phase transition in n-alkane at higher pressures. In view of this and to verify the theoretical prediction, we have undertaken a comprehensive investigation of n-alkane under pressure at ambient temperature with Raman spectroscopy as the probe.

### 3.2. Experimental section

We have used n-alkane bought from Sigma-Aldrich without further purification. A Mao-Bell type piston cylinder diamond anvil cell (DAC) with a 1:6 lever arm was used to generate the pressure [29]. The pressure was measured in situ using the ruby fluorescence technique [30]. The experiments were carried out in a backscattering geometry using a laser excitation wavelength of 532 nm from a solid-state diode pumped Nd-YAG laser (Coherent Inc., USA) of ~120 mW power. The Raman spectra were recorded using a Jobin-Yvon Triax 550 and a liquid $N_2$ cooled CCD detector (Instrument SA, USA), the details of which can be found in ref [31, 32].

### 3.3. Conformation

Configuration is the permanent structure of the molecule that cannot be changed with out chemical reaction. Conformation is the structure of the single molecule defined sequence of bonds and torsion angles.

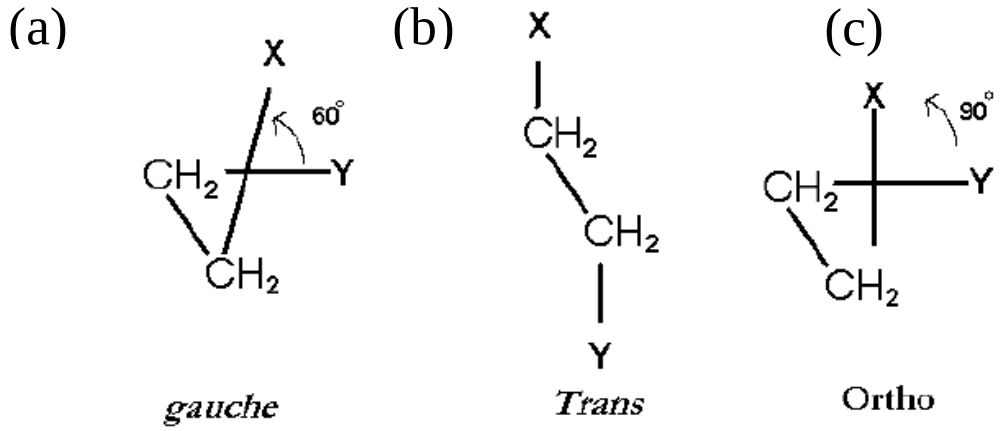


**Figure 3.1.** Schematic representation of a) Gauche, b) Trans, c) Ortho conformations in carbon chains.

When the torsion angle is 60º, we refer to it as *gauche* conformation (see figure 3.1 (a)) Similarly when the torsion angle is 90º, it is *ortho* conformation and when it is 180º, we call it *Trans* conformation.

In this work, we have done high pressure Raman studies on medium chain alkanes namely, n –heptane, n – hexane and n – pentane and their conformational change with high pressures and respective phase transitions.

### 3.4. Results

#### 3.4.1. n-heptane

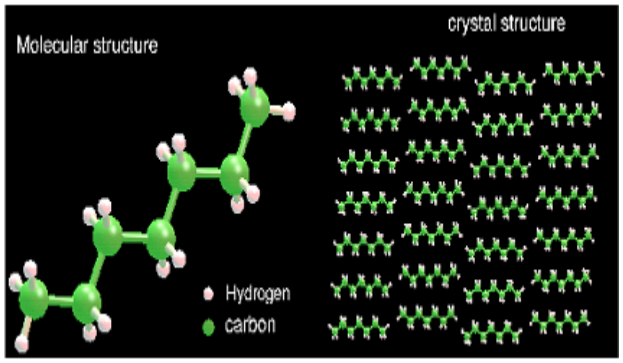


**Figure 3.2.** Molecular and crystal structure of n-heptane

n-heptane ($C_7H_{16}$) crystallizes in a triclinic cell with space group $P\overline{1}$, with crystal density 0.890 gm/cm$^3$ and having lattice parameters a=4.15 Å, *b*=19.97 Å, c=4.69 Å, $\alpha$=91.3°, $\beta$=74.3° and $\gamma$=85.1° at a pressure of ~1.2.-1.5 GPa (see figure 3.2) [26]. The chain axis of each molecule makes an angle of 2° with the *ab*-plane and 71° with the *a*-axis. In general liquid phase of n-heptane contains all kind of trans and gauche conformational rotamers.

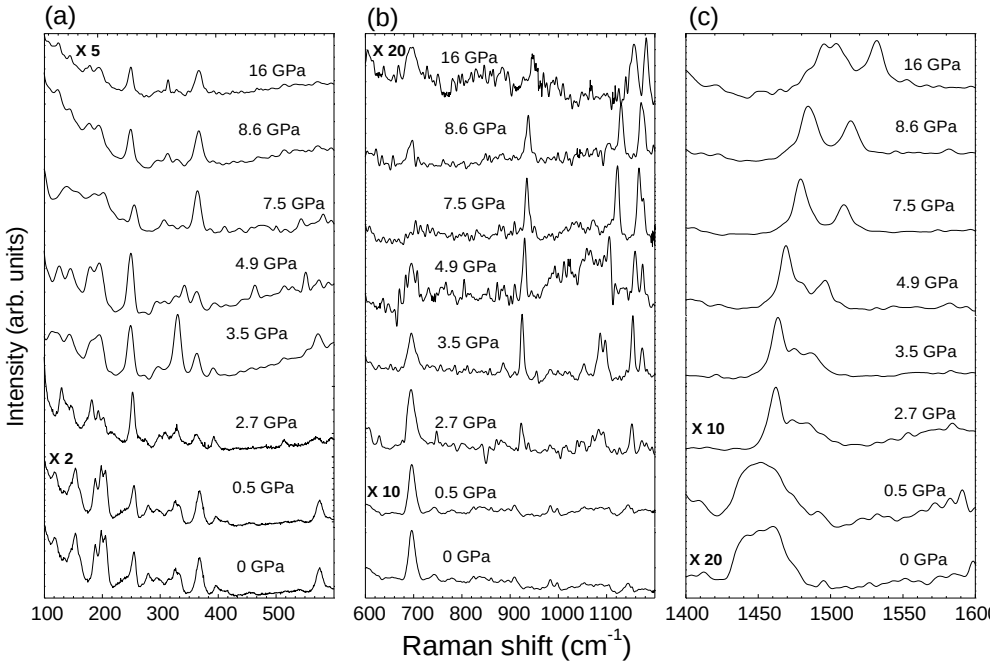


**Figure 3.3.** Raman spectra of *n*-heptane at ambient conditions and at high pressures. For larity the spectra have been divided into three parts: (a) 100-600, (b) 600-1200, and (c) 1400-1600 cm$^{-1}$. The region 1200-1400 cm$^{-1}$ is dominated by a diamond first-order peak and has not been shown.

Figure 3.3. shows the Raman spectra of *n*-heptane at ambient and high pressures. The highest pressure was 16, 17 GPa in all these experiments. Table 3.1 shows the mode frequencies ($\omega$), pressure derivative (d$\omega$/d*P*), and Raman mode assignments of *n*-heptane at three different phases deduced from the pressure behavior of the Raman modes up to a pressure of 16 GPa. The mode assignments were based on ref [33].

**TABLE 3.1:** Frequency (ω), its pressure derivative (dω/dP) for the various Raman modes of *n*-heptane in three different phases and their mode assignments.

| Phase I (0 GPa) | | Phase II (1.4 GPa) | | Phase III (7.5 GPa) | | |
|---|---|---|---|---|---|---|
| Frequency $cm^{-1}$ | dω/dP | Frequency $cm^{-1}$ | dω/dP | Frequency $cm^{-1}$ | dω/dP | Assigned mode |
| 115 | 0.08 | | | | | Lattice and acoustic mode |
| 134 | 0.16 | 134 | -0.08 | 131 | 0.04 | LAM |
| 152 | 0.16 | 152 | 0.04 | 153 | 0.02 | Librational mode |
| 187 | -0.07 | 185 | 0.01 | | | LAM |
| 198 | -0.01 | 197 | 0.06 | | | LAM |
| 205 | 0.03 | 205 | -0.01 | 206 | -0.06 | LAM |
| 252 | 0.23 | 255 | 0.02 | | | Methyl rotation |
| 278 | 0.05 | | | | | Methyl torsion |
| 295 | 0.24 | 300 | 0.06 | | | Methyl torsion |
| 313 | -0.24 | 311 | 0.06 | | | LAM |
| 328 | -0.24 | 330 | 0.72 | 366 | 0.48 | Librational mode |
| 367 | -0.19 | 364 | 0.15 | | | GTTT conformer |
| 399 | -0.22 | 395 | 0.13 | | | Super position of GTTT & TTGG |
| 568 | 2.67 | 595 | -0.15 | | | Single gauche |
| | | | | 693 | 0.09 | Inphase $CH_3$ rocking |

**TABLE 3.1**. (*continued*)

| | | | | | | |
|---|---|---|---|---|---|---|
| 696 | -0.23 | 694 | 0.09 | | | Inphase $CH_3$ rocking |
| 743 | 0.18 | | | | | $CH_2$ rocking |
| 818 | 0.94 | 842 | 0.64 | 842 | 0.14 | Sym C-C stretching |
| 842 | 1.15 | | | | | Sym C-C stretching |
| 908 | 0.40 | 926 | 0.26 | 937 | 0.21 | $CH_2$ twist |
| 985 | -0.92 | 985 | -0.04 | | | Methyl rocking |
| 1000 | 0.57 | 1018 | 0.54 | | | Skeletal C-C stretching |
| 1056 | -0.41 | 1053 | 0.47 | 1079 | 0.39 | Skeletal C-C stretching |
| 1090 | 0.28 | 1089 | 0.37 | 1106 | 0.47 | Gauche defect |
| | | | | 1144 | 0.10 | Trans |
| 1148 | 0.06 | 1156 | 0.31 | 1171 | 0.11 | Trans |
| 1178 | 0.37 | 1181 | 0.75 | | | $CH_2$ twisting |
| 1442 | 0.13 | 1461 | 0.09 | | | Asym $CH_2$ and $CH_3$ bending |
| 1453 | -0.01 | 1473 | 0.20 | 1475 | 0.45 | Asym$CH_2$ and $CH_3$ bending |
| 1461 | 0.13 | 1483 | 0.55 | | | Symmetric out of plane $CH_3$ bending |

We observe the liquid to solid transition around 1.5 GPa. Since this has been reported earlier, [25, 26] we will restrict our discussion to the pressure effects in the solid phase of *n*-heptane in this work. Since *n*-heptane is a molecular solid, the Raman spectrum shows

the librational modes along with the lattice and the acoustic modes in the range 100-400 $cm^{-1}$, also known as external modes. The internal modes or the intra-molecular vibrations are found above 250 $cm^{-1}$. Internal modes have been grouped into (i) rotation, torsion, and rocking modes of methyl end group, (ii) vibrational modes due to gauche and trans conformations, (iii) skeletal C-C vibration modes, (iv) $CH_2$ stretching vibrations, and (v) $CH_2$ and $CH_3$ bending vibration modes. We discuss below the effect of the pressure on these modes and the implication of the same on the structure of *n*-heptane in the solid phase.

**(I) External Modes**

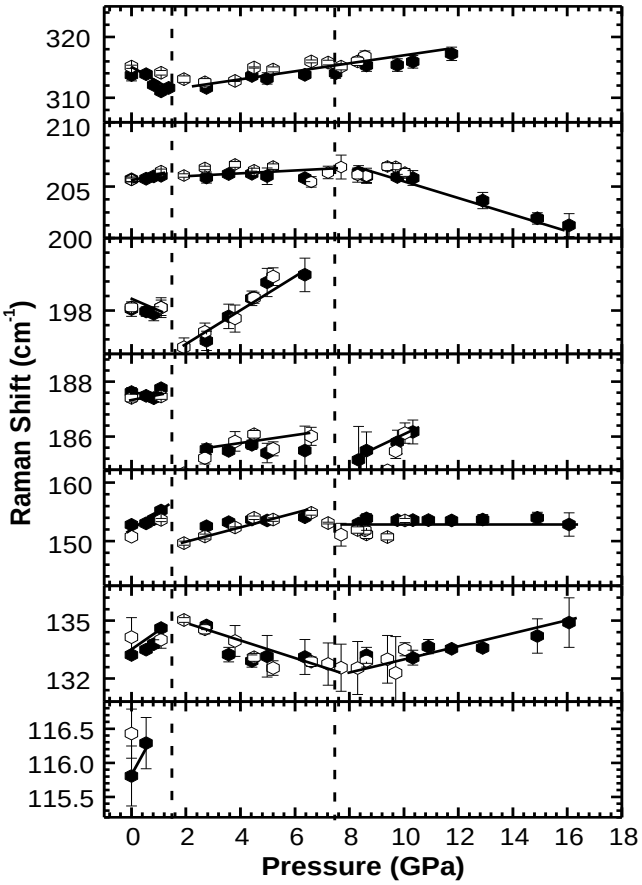


**Figure 3.4.** Behavior of external modes as a function of pressure. Filled symbols represent increasing pressure data, and open symbols represent reverse pressure data. The solid lines through the data points are linear fits to the data.

In a molecular solid, where the inter-molecular interactions are van der Waal interaction, upon application of pressure we expect large changes in the lattice, acoustic, and librational modes. These modes are very sensitive to subtle transition. Figure 3.4 shows the pressure dependence of all the external modes observed in *n*-heptane. Phase I is the liquid phase (0-1.5 GPa), Phase II is the solid phase of n-heptane between 1.5 to 7.5 GPa. Above 7.5 GPa we observe the phase III. Around 7.5 GPa, the 197 $cm^{-1}$ mode of phase II disappears along with large changes in pressure behavior of other mode signifying the appearance of phase III. It is interesting to note the pressure dependence of the 152 $cm^{-1}$ mode of phase I. This corresponds to vibration followed by rotation involving atomic displacements in the direction perpendicular to the molecular long axis [26]. In the solid phase this mode shows very little pressure dependence. This suggests that the *n*-heptane is densely packed in the direction perpendicular to the molecular long axis. The decrease in number of lattice and acoustic modes along with changes in the mode behavior above 7.5 GPa suggests a definitive phase transition.

**(II)Internal Modes**

**(i) Methyl rotation, Torsional, and Rocking Vibrational Modes.**

Figure 3.5 shows the vibrational mode frequencies associated with methyl rotation, torsion, and rocking as a function of pressure. We observe five modes associated with the methyl end groups in this category at ambient conditions: In phase I, 252 $cm^{-1}$ is the methyl rotation mode, 278 and 295 $cm^{-1}$ are methyl torsional modes, and 696 and 985 $cm^{-1}$ are methyl rocking modes [33]. Molecular dynamic simulation studies suggest that the methyl end group vibrations show a considerable dampening with increase in pressure up to 7 GPa [26]. As shown in Figure 3.5, we observe the disappearance of the methyl torsional modes. This means that the torsional mode ceases to exist above 7.5 GPa. The methyl rocking modes also disappear, but a new mode appears in phase III at a much lower frequency (692 $cm^{-1}$).

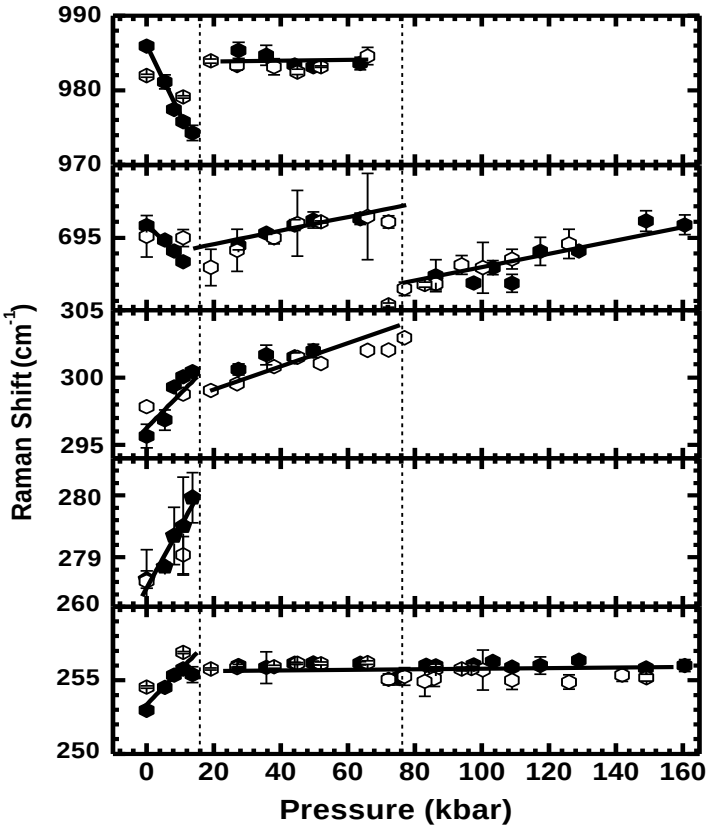


**Figure 3.5.** Vibrational modes associated with $CH_3$ rotation, torsional, and rocking as a function of pressure. Filled symbols represent increasing pressure data, and open symbols represent reverse pressure data. The open and filled star symbols represent the new mode above 7.5 GPa. The solid lines are linear fits to the data.

These observations support the MD simulation studies [26] namely; there is considerable dampening of vibrational degree of freedom for the methyl end groups at high pressures leading to a phase transition at 7.5 GPa. It is interesting to see that 252 $cm^{-1}$ mode (phase I) associated with methyl rotation about the long axis of the molecule does not show any pressure dependence in the solid phase. This could be due to dense packing of *n*-heptane along the *c*-axis as the pressure is increased. In IR studies of *n*-alkanes at high temperatures, in an all-trans (planar) conformation, one observes hindered rotation and twisting about the long axis, which supports our case [34].

**(ii) Vibrational modes of gauche and trans conformers**

It is known that with increase in pressure, the gauche form is favored over the trans form across the liquid to solid transition. This has been shown in the case of *n*-hexane along the liquid to solid transition, but experiments have been limited to low pressures [35]. In *n*-heptane also, in the liquid to solid transition, we observe an increase in the gauche form compared to the trans form looking at the intensities of these modes. Figure 3.6. shows the various modes associated with the gauche and trans conformers and their pressure dependence. In the solid phase, with the increase in pressure, that is, decrease in volume, linear alkanes should show a considerable change in their gauche and trans conformers. In the case of *n*-heptane at ambient pressures we observe both single and double gauche conformers along with all-trans conformers (see Table 3.1). Due to the presence of a strong diamond Raman band around 1332 $cm^{-1}$ from the DAC, we could not quantitatively measure the intensities of these modes.

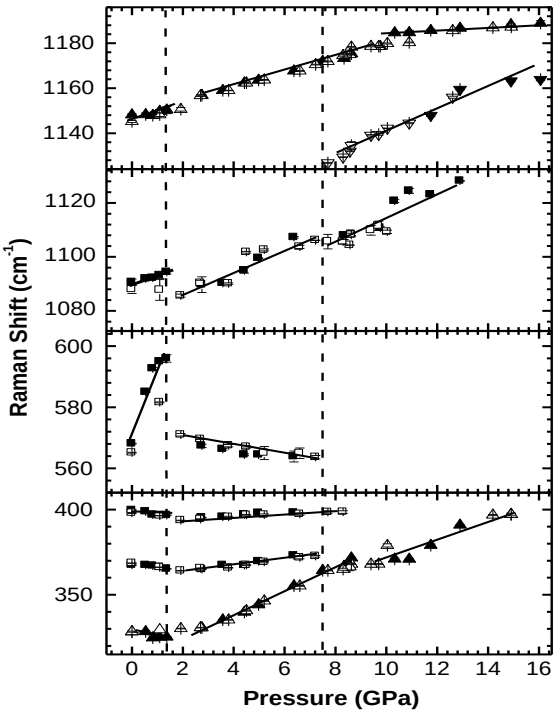


**Figure 3.6.** Vibrational modes associated with gauche and trans conformers as a function of pressure. Filled symbols represent the increasing pressure data, and open symbols represent reverse pressure data. Squares represent the gauche conformers, and triangles represent trans conformers. The solid lines are linear fits through the data.

It is customary to look at the intensities of 1090 and 1148 $cm^{-1}$ to ascertain the amount of gauche and trans conformers [36-38]. In the case of *n*-hexane, low-frequency modes around 250-550 $cm^{-1}$, which are related to these conformers, have been looked at to determine the conformers [35]. In our case, too, the qualitative measurements of intensities of 367 (GTTT), 399 (GTTT and TTGG), and 568 $cm^{-1}$ (single gauche) in phase I increases with increase in pressure, suggesting that increase in pressure favors the gauche form as seen in *n*-alkanes [35,39]. At pressures above 5 GPa, in the solid phase, we observe that with increase in pressure there is considerable decrease in the gauche defects and increase in trans conformers. This is seen from the disappearance of 367, 399, and 568 $cm^{-1}$ (phase I) and the appearance of a new mode at 1144 $cm^{-1}$ (all trans of phase III) above 7.5 GPa. We have made a qualitative intensity measurement of the 1090 and 1148 $cm^{-1}$ modes of phase I. We observe an increase in intensity of the 1148 $cm^{-1}$ mode with a decrease in intensity of the 1090 $cm^{-1}$ mode. This again suggests that *n*-heptane at high pressure is tending toward an all-trans conformation [36-38]. However, the 1090 $cm^{-1}$ mode persists up to 12 GPa and this mode is difficult to measure above this pressure, suggesting that there are some gauche defects still present at high pressures.

**(ii) C-C Stretching vibrational modes**

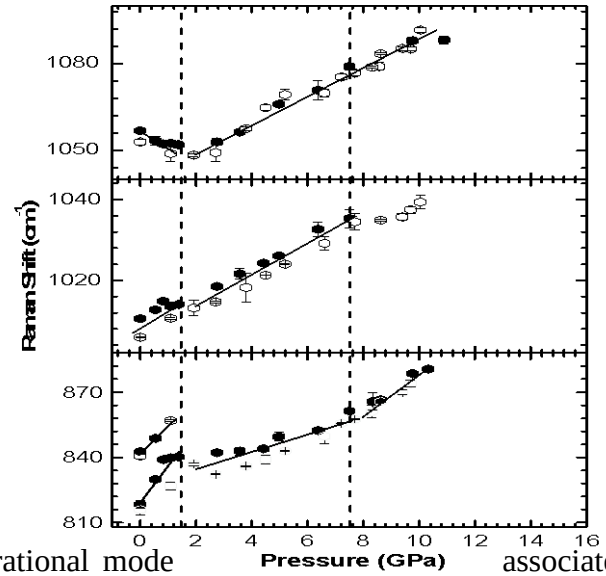


**Figure 3.7.** Vibrational mode associated with skeletal C-C stretching as a function of pressure. Filled symbols represent increasing pressure data, and open symbols represent reverse pressure data. The solid lines are linear fits through the data.

Figure 3.7 shows various C-C backbone stretching modes associated with *n*-heptane and its pressure dependence. As we increase the pressure, these modes harden in the solid phase. With a decrease in the volume at high pressures, there is an increase in the inter-atomic interactions, leading to a much stiffer mode. These modes are difficult to observe at pressures greater than 10 GPa due to interference from other modes in this region. The above observation also suggests that the *n*-heptane, being a linear chain, packs along the *c*-axis, which is perpendicular to the chain direction. Hence the phase transition has no effect on the behavior of these modes across the transition.

**(iii) $CH_2$ Vibrational Modes**

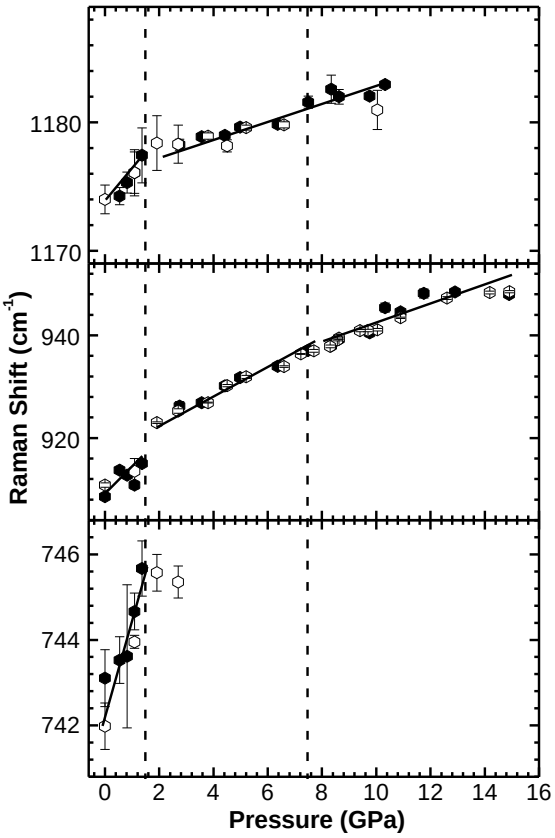


**Figure 3.8.** $CH_2$ vibration modes as a function of pressure. Filled symbols represent increasing pressure data, and open symbols represent reverse pressure data. The solid lines are linear fits through the data.

Figure 3.8 shows the $CH_2$ vibrational modes and their pressure dependence. The $CH_2$ rocking mode at 743 $cm^{-1}$ of phase I cease to exist in the solid phase above 7.5 GPa due to restriction in the degree of freedom along the *c*-axis in the condensed phase. The $CH_2$ twisting modes at 908 and 1178 $cm^{-1}$ of phase I show considerable hardening in both the liquid phase and solid phase. The hardenings of these modes are expected due to increase in inter-atomic interactions in the condensed phase at higher pressures leading to stiffening of these modes. The mode behavior is not affected by increase in pressure. This again suggests that the high-pressure phase III (> 7.5 GPa) is not structurally very different from the low-pressure phase II (< 7.5 GPa) except for changes around methyl end group and conformation.

### (iv) $CH_2$ and $CH_3$ Bending

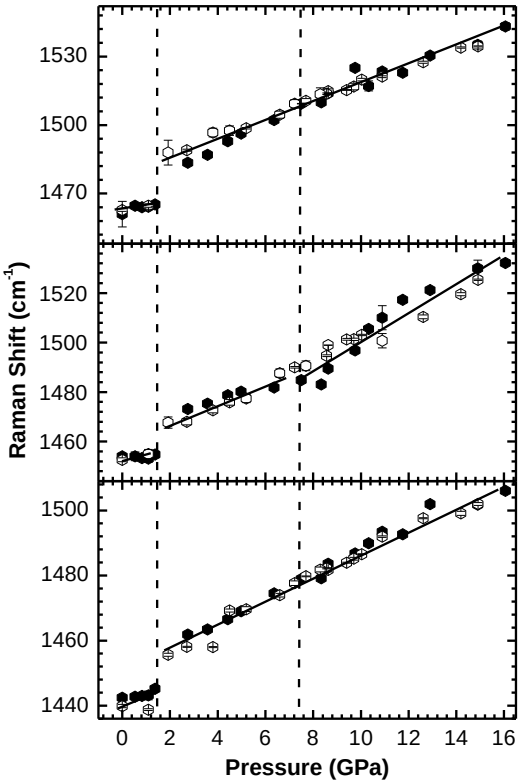


**Figure 3.9.** $CH_2$ and $CH_3$ bending modes as a function of pressure. Filled symbols represent increasing pressure data, and open symbols represent reverse pressure data. The solid lines are linear fits through the data.

Figure 3.9 shows the $CH_2$ and $CH_3$ bending mode region and its pressure dependence. Both the symmetric and anti-symmetric bending modes show large pressure dependence as shown from the large $d\omega/dP$ values in Table 3.1. These modes persist up to 16 GPa and show changes in $d\omega/dP$ at both 1.5 and 7.5 GPa. This indicates the liquid-solid transition and solid-solid transition respectively.

### 3.4.2. N-hexane

N-hexane crystallizes in the triclinic structure with one paraffin molecule per unit cell [40]. In this structure, all the molecular axes and all planes through the carbon atoms are parallel to each other. The $-CH_3$ end groups are arranged in planes, which make an angle of about 73° with the molecular axes.

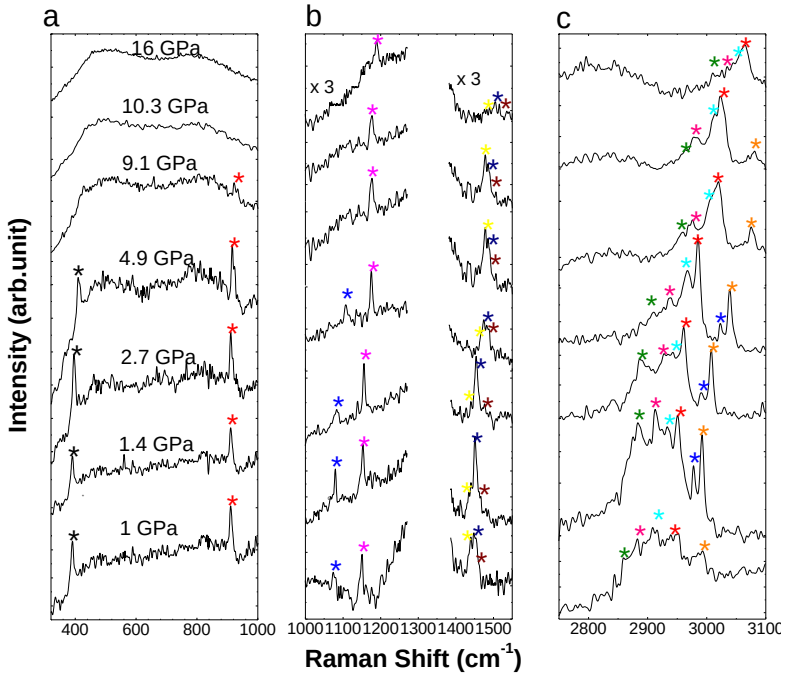


**Figure 3.10.** Raman spectra of n-hexane recorded at ambient conditions and at high pressures. For clarity the spectra has been divided into three regions (a) 300-1000 $cm^{-1}$, (b) 1000-1600 $cm^{-1}$ and (c) 2700-3100 $cm^{-1}$. The 1200 – 1400 $cm^{-1}$ region is dominated by diamond first-order peak and has not been shown. The pressure value indicated against each spectrum in (a) is valid for both (b) and (c). The various colored star symbols in each spectra show the peaks which are followed with different pressure range.

The sub-cell, which characterizes the lateral packing of $>CH_2$ groups, are also triclinic. N-hexane crystal structure is similar to that of n-heptane [40, 41]. Several dynamic mixtures of distinct conformations including straight chain a*ll–trans* isomer and kinked chain conformers with up to three gauche bonds will exist in the pure liquid n-hexane. The conformers contribution to the n-hexane at ambient conditions are approximately 30% − TTT, 35% − TTG, 15% − TGT, 15% − GGT and 5% − GGG [42, 43]. Among these conformers, TTT, TTG and TGT conformers have strong features in Raman spectra. Therefore these conformers have been studied in detail in this chapter.

The Raman spectra of n-hexane at ambient condition and high pressures are shown in the Fig. 3.10. The liquid phase Raman spectra of n-hexane agrees very well with previous reports [28, 42-44]. Due to the high Rayleigh background, it was not possible to observe the low frequency modes below 300 $cm^{-1}$. The observed Raman modes of n-hexane at ambient conditions can be classified into: (a) longitudinal acoustic mode (LAM or C-C-C angle bending mode), (b) methyl rocking mode, (c) C-C skeletal stretching modes, (d) methylene and methyl bending modes and (e) poly methylene and methyl stretching modes. In the presence of the predominant first order diamond peak, we were not able to resolve the peaks around 1332 $cm^{-1}$ region. Changes in the Raman mode behavior as well as intensity behavior with pressure are a good indicator of a possible phase transition. The pressure dependency of various Raman modes and their intensity of n-hexane have plotted in Figures (3.11-3.15). In Table 3.2, we have tabulated the individual modes and its pressure derivative ($d\omega/dP$) at representative pressure for each phase. The mode assignment was based on Refs. [42-49]. We observe a liquid–solid transition around 1.4 GPa. Since the liquid to solid transition has already been reported [28] we restrict our discussion to the condensed phase of n-hexane. To the best of our knowledge, this is the first report on high pressure Raman studies on n-hexane above 3 GPa.

**TABLE 3.2.** Frequency (ω) of the Raman modes of n-hexane and its pressure derivative (dω/d*P*) observed in different phases are shown below. Their mode assignments are given based on Refs. [42-49].

| **Phase I (1 GPa)** | | **Phase II (>1.4 GPa)** | | **Phase III (>9.1 GPa)** | | **Mode assignment** |
|---|---|---|---|---|---|---|
| ω($cm^{-1}$) | dω/dP | ω ($cm^{-1}$) | dω/dP | ω ($cm^{-1}$) | dω/dP | |
| 328 | 3.3 | 335 | 5.5 | | | LAM C-C-C angle bending |
| 908 | 7.5 | 915 | 1.8 | | | Methyl rocking mode (GTT) |
| 1075 | 4.8 | 1081 | 3.5 | | | Skeletal C-C stretching (TTG + TGT) |
| 1146 | 3.6 | 1152 | 2.9 | 1173 | 2.8 | $CH_3$ Rocking (TTT) + C-C stretching (TGT) |
| 1445 | 3.8 | 1436 | 4.7 | 1472 | 2.8 | Asymmetric $CH_2$ and $CH_3$ bending |
| 1446 | 0.2 | 1453 | 3.9 | 1482 | 2.3 | $CH_2$ Rocking (TTT) |
| 1465 | 4.4 | 1474 | 1.8 | 1485 | 1.9 | $CH_3$ deformation (TTT+TTG) and $CH_2$ Scissoring (TGT) |
| 2872 | 4.0 | 2880 | 10.4 | 2964 | 5.9 | Symmetric $(CH_2)_n$ stretching(TTT) |
| 2902 | 9.9 | 2913 | 8.5 | 2968 | 5.8 | Symmetric $(CH_2)_n$ stretching(TTT) |
| 2923 | 2.6 | 2929 | 8.4 | 3008 | 6.0 | Symmetric $(CH_2)_n$ stretching (TGT) |
| 2946 | 3.1 | 2952 | 8.3 | 3020 | 5.2 | In–plane asymmetric methyl stretching (TTT) |
| | | 2977 | 11.3 | | | Out of plane asymmetric methyl stretching (GTT) |
| 2992 | 20.0 | 2993 | 11.8 | 3069 | 4.3 | Asymmetric C–H methyl stretching (TTT) |

**(i) LAM (C-C-C angle bending mode)**

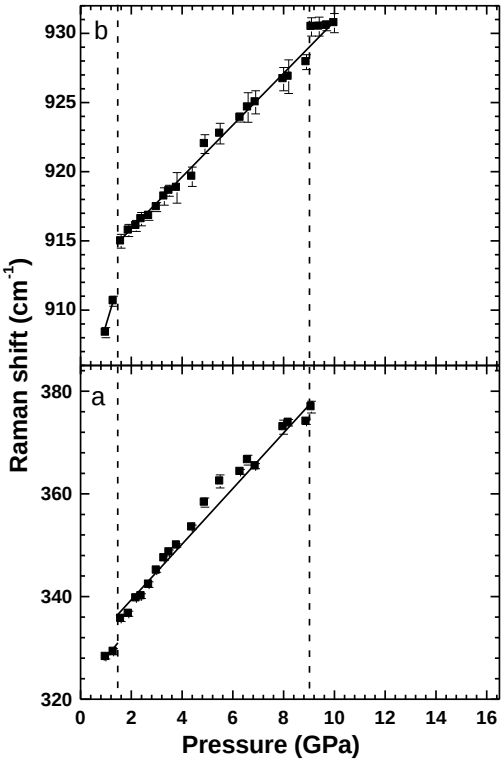


**Figure 3.11.** The Raman modes of (a) LAM and (b) Methyl Rocking region as a function of pressure. The solid lines through the data points are the linear fit to the data.

The low frequency Raman modes depends on the number of molecules per unit cell. Since the even paraffin starting from $C_6H_{14}$ to $C_{24}H_{54}$ has only one molecule per unit cell, they have the smallest number of Raman bands in the low frequency region [40]. The low frequency modes are very weak in the liquid phase in the case of both Raman and IR spectra. This coupled with huge Rayleigh background made it difficult to observe any modes below 300 $cm^{-1}$. The bending and torsional modes appear in the region 200-600 $cm^{-1}$ which overlaps with LAM at 328 $cm^{-1}$ and other external modes. We observe only the LAM (328 $cm^{-1}$) in our experiment. This mode is called an accordion mode due to its in–phase expansion and contraction of the C-C-C bend angle [50, 51]. The frequency of this mode is inversely proportional to the length of the chain [52]. In the case of n-hexane, this mode is related to GTT conformation (where G stands for gauche and T stands for trans) [42-43, 45]. As shown in Fig. 3.11(a), there is an abrupt change in the

frequency of this mode around 1.4 GPa. This is due to the liquid–solid transition reported earlier [28]. This mode disappears beyond 9.1 GPa. This could signify the onset of a phase transition and will be discussed later.

**(ii) Methyl Rocking mode**

The well resolved mode at 908 $cm^{-1}$ is associated with a single gauche conformation (GTT) [42-43, 45]. Figure 3.11(b) shows the pressure dependence of this mode. This mode is related to $-CH_3$ end group, hence has an importance in chain packing and conformational randomness in the solid phase [53]. There is a considerable change near the crystallization pressure at 1.4 GPa as shown in Fig, 3.11 and Table 3.2. Beyond the crystallization, this mode has a positive $d\omega/dP$. At higher pressure the intensity reduces and gradually disappears beyond 9.1 GPa. This could be an onset of a phase transition and is discussed later.

**(iii) Skeletal C–C stretching region (1050 – 1200 $cm^{-1}$)**

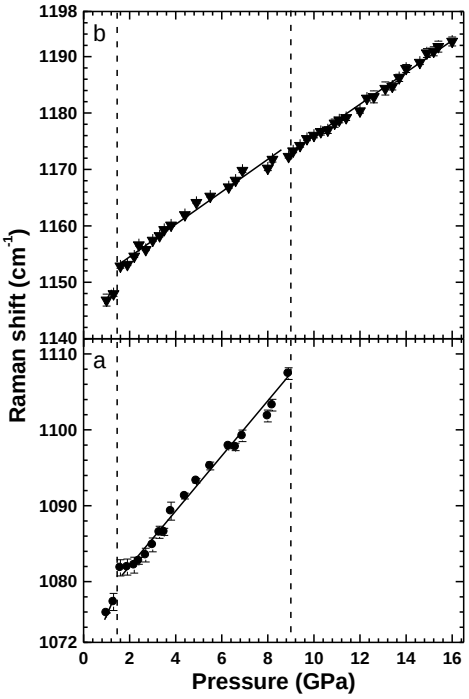


**Figure 3.12.** Raman modes of skeletal C-C stretching modes (a) TTG + TGT, (b) TTT + TGT conformers as a function of pressure. The solid lines are the linear fit to the data.

In the condensed state the chain packing is reflected by the carbon back-bone skeletal stretching mode behavior as a function of pressure. Figure 3.12 shows the pressure dependence of these modes. These modes occupy the spectral region 1050 – 1200 $cm^{-1}$. In the case of n-hexane, the mode at 1075 $cm^{-1}$ has contribution from both skeletal C-C stretching TTG and TGT isomers. The mode at 1146 $cm^{-1}$ originates from $-CH_3$ rocking (TTT) and C-C stretching (TGT) conformers [43, 45]. These modes become sharp and distinguishable beyond 1.4 GPa as a result of periodic arrangement of the molecules upon crystallization. Beyond this pressure both these modes (1075 and 1146 $cm^{-1}$) show a positive dω/dP up to 9.1 GPa. As shown in Fig. 3.12 (a), the mode which has only gauche conformers, namely, 1075 $cm^{-1}$ mode disappears beyond 9.1 GPa in comparison with the mode associated with the trans conformers (1146 $cm^{-1}$ mode), which persists up to 16 GPa as shown in Fig. 3.12 (b).

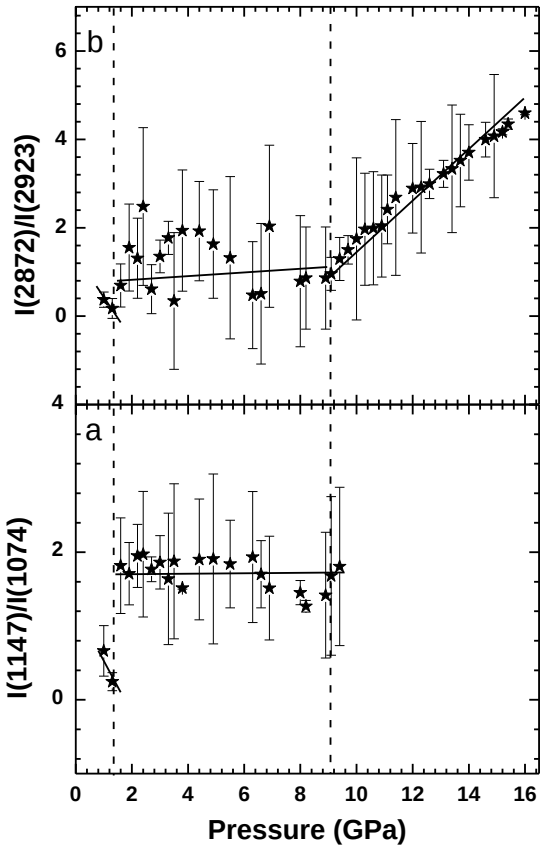


Figure 3.13. The intensity ratio (a) $I_{1146}/I_{1075}$ and (b) $I_{2872}/I_{2923}$ of *trans* and *gauche* conformational isomer of n-hexane are plotted as a function of pressure. The solid lines are the linear fit to the data.

It is relevant to know about the intensity variation of these modes with pressure since it reflects the population of trans and gauche conformers in n-hexane in any phase. Figure 3.13 (a) shows the intensity ratio of 1146 $cm^{-1}$ and 1075 $cm^{-1}$ mode. The intensity ratio ($I_{1146}/I_{1075}$) suggests an increase in *all–trans* conformers with some gauche conformers still persisting above crystallization [46-48]. At 9.1 GPa, the gauche conformers seize to exist. This point with high frequency mode intensity shown in fig 3.13 (b) and its implication on the possible phase transition will be discussed later.

### (iv) Methylene and Methyl bending region (1400 – 1500 $cm^{-1}$)

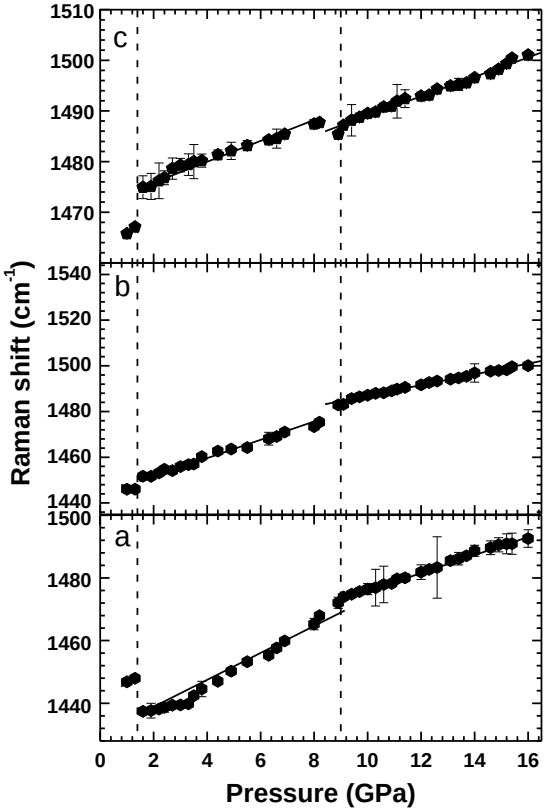


**Figure 3.14.** Raman modes of (a) asymmetric $>CH_2$ and $-CH_3$ bending, (b) $>CH_2$ Rocking (TTT) and (c) $-CH_3$ deformation (TTT + TTG) and $>CH_2$ scissoring (TGT) as a function of pressure. The solid lines are the linear fit to the data.

The $>CH_2$ and $-CH_3$ bending mode region in n-alkane is around 1400-1500 $cm^{-1}$ and Fig. 3.14 shows its pressure dependence. In the case of n-hexane, the

modes at 1445, 1446 and 1465 $cm^{-1}$ are associated with asymmetric $>CH_2$ and $-CH_3$ bending, $>CH_2$ Rocking (TTT) and the contribution from $-CH_3$ deformation (TTT+TTG) and $>CH_2$ scissoring (TGT) respectively [43, 45]. These modes show a strong dependence on pressure and have a large positive dω/dP as shown in Table 3.2. These modes persist up to the highest pressure but show a change in slope at 9.1 GPa suggesting a possible phase transition. The behavior of the bending modes of n-hexane is similar to that observed in the case of n-heptane.

**(v) Poly methylene and methyl stretching region**

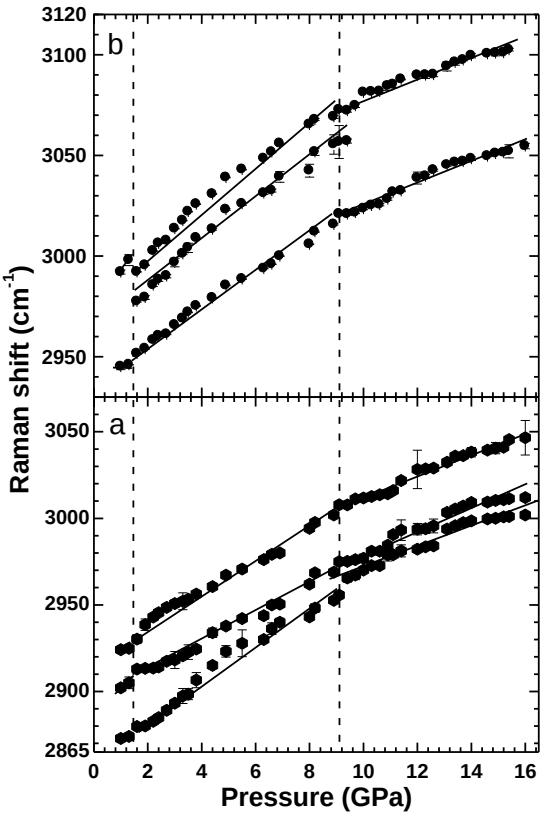


**Figure 3.15.** (a) $(CH_2)_n$ and (b) $-CH_3$ stretching modes as a function of pressure. The solid lines are the linear fit to the data.

The C-H stretching region is influenced by large intra-molecular interaction and interaction between symmetric C-H stretching fundamental and the overtone of the $>CH_2$ scissor mode. These bunch of modes around 2800-3100 $cm^{-1}$ play a key role in the

conformational chain packing at higher pressure. These modes have been classified into two categories [40,43,45] Symmetric methylene stretching region comprising of three bands; a) sharp band at 2872 $cm^{-1}$ (TTT), b) broad band at 2902 $cm^{-1}$ (TTT) and c) a shoulder near 2923 $cm^{-1}$(TGT). Methyl stretching region involves another three modes: a) in-plane asymmetric methyl stretching (TTT) at 2946 $cm^{-1}$, b) out of plane asymmetric methyl stretching (GTT) at 2977 cm-1 and c) asymmetric C-H stretching of $CH_3$ (TTT) at 2992 $cm^{-1}$. Figure 3.15 shows the pressure dependence of these modes and their $d\omega/dP$ values are given in Table 3.2. Large changes around 1.4 GPa is a result of the liquid–solid transition [28].

There is a considerable mode broadening as well as changes in their intensity ratio around 9.1 GPa as shown in Fig. 3.13 (b) [54]. This observation suggests a possible phase transition in n-hexane around 9.1 GPa. As is true in n-alkanes, upon crystallization the n-alkanes retain some amount of gauche conformers. In the case of n-hexane, like n-heptane in the solid phase we observe the presence of gauche conformers. This is confirmed by appearance of 2977 $cm^{-1}$ (GTT) mode beyond solidification. This mode is not well resolved in the liquid phase of n-hexane. (See Figure 3.10.c) Above 9.1 GPa we observe an increase in trans conformer, since the $I_{2872}/I_{2923}$ (TTT/TGT) ratio shows a steep increase as shown in Fig. 3.13 (b)

### 3.4.3. n-pentane

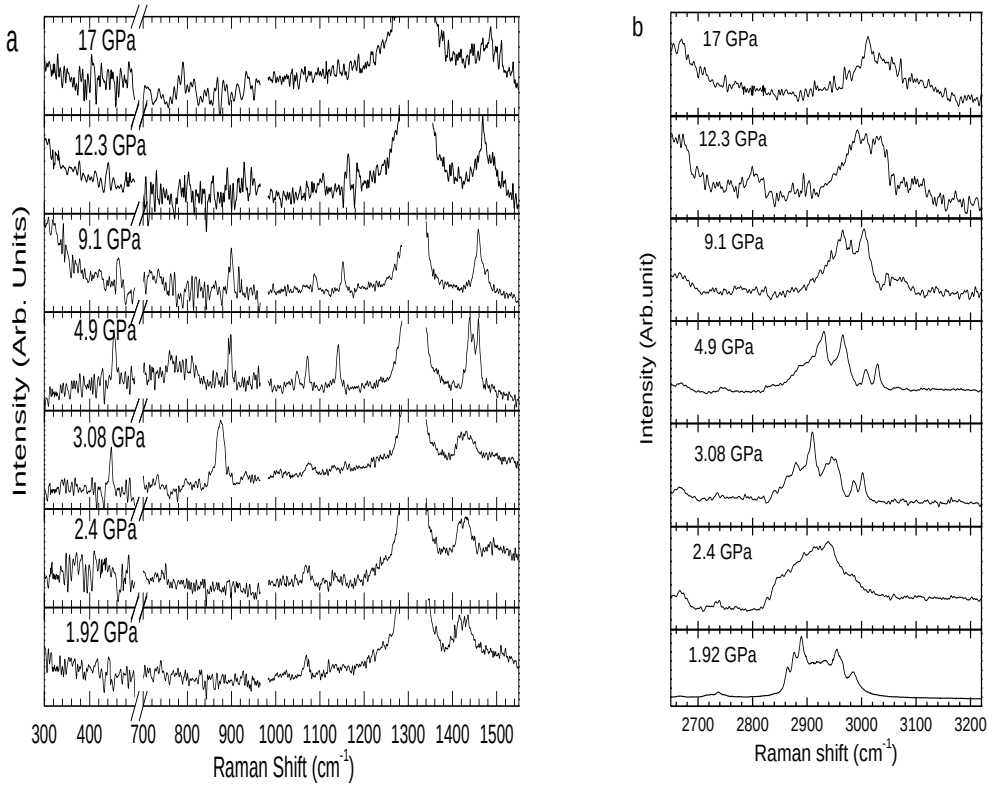


**Figure 3.16.** Raman spectra of *n*-pentane recorded at ambient conditions and at high pressures. For clarity, the spectra have been divided into two regions: (a) 300-1500 $cm^{-1}$ and (b) 2700-3200 $cm^{-1}$. The 1200-1400 $cm^{-1}$ region is dominated by diamond first-order peak and has not been shown.

Figure 3.16 (a-b) shows the Raman spectra of *n*-pentane at ambient and high pressures. Due to high Rayleigh background, we are unable to clearly observe any low-frequency mode below 300 $cm^{-1}$. The Raman mode frequency ($\omega$), its pressure derivative ($d\omega/dP$), and the Raman mode assignments are listed in Table 3.3.

**TABLE 3.3.** Frequency ($\omega$) of the Raman modes of *n*-pentane and its pressure derivative ($d\omega/dP$) observed in the various phases

| **Phase I (1.9 GPa)** | | **Phase II (>3.0 GPa)** | | **Phase III (>12.3 GPa)** | | **Mode assignment** |
|---|---|---|---|---|---|---|
| $\omega$ ($cm^{-1}$) | $d\omega/dP$ | $\omega$ ($cm^{-1}$) | $d\omega/dP$ | $\omega$ ($cm^{-1}$) | $d\omega/dP$ | |
| | | 444 | 5.4 | | | LAM C-C-C angle bending |
| | | 894 | 3.4 | | | Methyl rocking mode (GG) |
| | | 1065 | 5.5 | | | All-*trans* Skeletal C-C stretching |
| 1092 | 1.7 | 1093 | 3.4 | | | Skeletal C-C stretching with gauche defect |
| 1157 | 2.9 | 1162 | 1.5 | | | All *trans* Skeletal C-C stretching |
| | | 1460 | 3.6 | 1495 | 0.4 | $CH_2$ and $CH_3$ bending |
| 1450 | 5.1 | 1473 | 5.0 | 1526 | 1.1 | Symmetric out of plane $CH_3$ bending |
| 2867 | 15.4 | 2890 | 9.6 | 2979 | 3.2 | Symmetric $(CH_2)_n$ stretching(TT) |
| 2897 | 0.1 | 2932 | 6.2 | 3006 | 6.3 | Symmetric $(CH_2)_n$ stretching(TG) |
| 2924 | 32.2 | 2961 | 7.5 | 3016 | 3.4 | Symmetric $(CH_2)_n$ stretching (TG) |
| 2934 | 4.3 | 2971 | 7.4 | 3045 | 1.7 | In–plane asymmetric methyl stretching (TG) |
| 2958 | 19.6 | 2996 | 9.0 | | | Out of plane asymmetric methyl stretching (TT) |
| 2993 | 15.4 | 3017 | 9.9 | | | Asymmetric C-H methyl stretching (TT) |

At around 3.0 GPa, we observe appearance of new modes as well as a sharp change in the Raman mode frequencies of *n*-pentane. This is the onset of the liquid-to-solid transition. We will not discuss this transition any further since it has already been reported earlier [55-57]. In the solid phase, *n*-pentane crystallizes in an orthorhombic crystal structure with four molecules in the unit cell [40]. The structure of the *n*-pentane

is completely different from other paraffin as the molecular long axes are not parallel to each other. We have classified the Raman modes observed in *n*-pentane into (1) longitudinal acoustic mode LAM, (2) methyl rocking mode, (3) C-C skeletal stretching region (1050-1150 $cm^{-1}$), (4) $CH_2$ and $CH_3$ bending (1400-1500 $cm^{-1}$), and (5) $(CH_2)_n$ and $CH_3$ stretching (2800-3100 $cm^{-1}$).

**(i) LAM (C-C-C Angle Bending)**

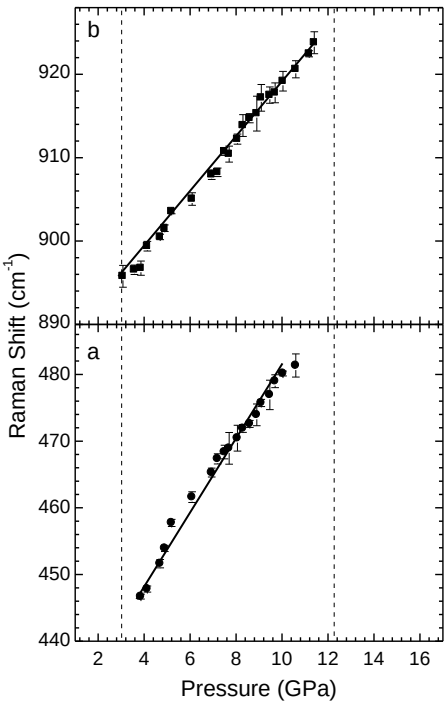


**Figure 3.17.** The Raman modes associated with (a) LAM and (b) Methyl Rocking region as a function of pressure. The solid lines through the data points are the linear fit to the data.

The LAM of *n*-alkanes is rather weak in the liquid phase in both infrared and Raman spectra [58]. In *n*-pentane, we could not observe the low frequency mode below 300 $cm^{-1}$ in the liquid as well as solid phase because of the presence of a large Rayleigh background. The torsional and bending modes exist in the region of 200-600 $cm^{-1}$. In the solid phase, we observe a high-frequency LAM around 440 $cm^{-1}$. These are related to the extension of the alkyl chains [50]. The LAM mode is associated with the C-C-C bond angle expansion or contraction in phase and is also known as the "accordion mode" [51-52]. It is mainly dependent on chain length and its frequency is inversely proportional to

the length of the ordered chain. This mode appears above the liquid-solid transition. Pressure behavior of LAM frequency is shown in Figure 3.17 a. Its disappearance around 12.3 GPa could suggest a possible solid-solid transition, which will be discussed later.

**(ii) Methyl Rocking Region**

The mode at 895 $cm^{-1}$ is related to methyl rocking with GG rotamers, [45] and its pressure dependence is shown in Figure 3.17 b. It is particularly sensitive to conformational randomness and motion of the local molecular state [53]. It is significantly important in large alkanes, because it probes the order of the alkane chain termini and is also sensitive to chain packing. In the present case, it appears in the solid phase of *n*-pentane. From Figure 3.17 b, it is seen that the mode disappears above 12.3 GPa. A possible phase transition at 12.3 GPa could be the origin for the disappearance (discussed later).

**(iii) Skeletal C-C Stretching Region (1050-1200 $cm^{-1}$)**

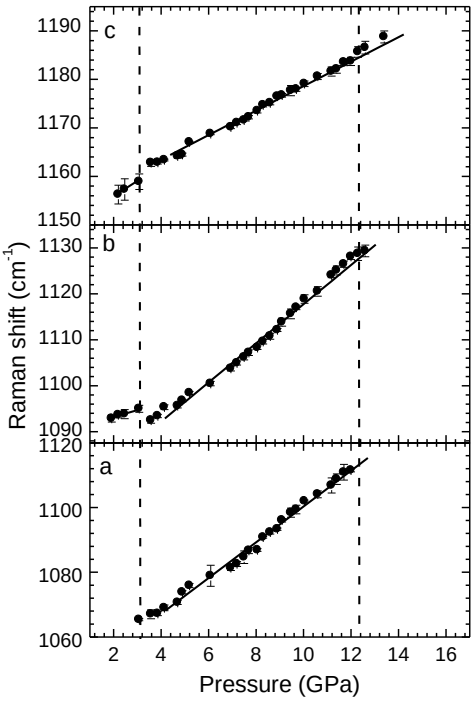


**Figure 3.18.** Raman modes associated with skeletal C-C stretching modes (a) TT, (b) TG, and (c) TT conformers as a function of pressure. The solid lines are the linear fit to the data.

The region 1050-1200 $cm^{-1}$ is related to the Raman modes associated with these conformers, and Figure 3.18 shows their pressure dependence. The Raman modes associated with the all-trans conformation are 1060 and 1130 $cm^{-1}$, where 1090 $cm^{-1}$ is related to globular gauche conformation [46-47, 59]. Figure 3.19 shows these two conformers in n-pentane.

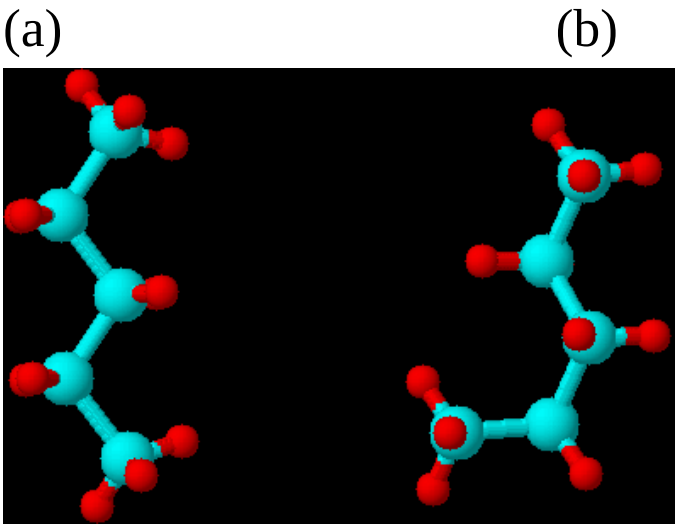


The Figure 3.19 shows schematic representation of (a) all–*trans,* (b)end *gauche* conformation for n–pentane respectively [46-49, 59-60].

A strong 1090 $cm^{-1}$ Raman mode in the liquid state suggests that large numbers of gauche rotamers are present in the liquid state. The appearance of 1060 $cm^{-1}$ mode and increase in intensity of the 1130 $cm^{-1}$ mode suggest that *n*-pentane in the condensed phase prefers to be in all-trans conformation.

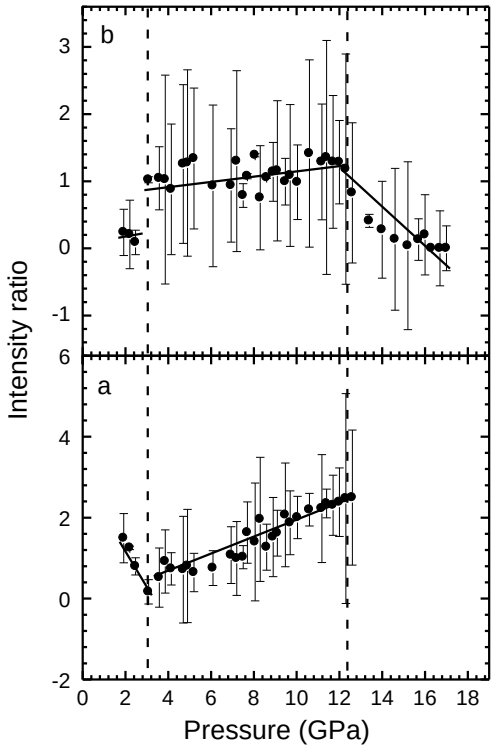


**Figure 3.20.** The intensity ratio (a) $I_{1130}/I_{1090}$ and (b) $I_{2850}/I_{2922}$ of TT to TG conformational isomer of n-pentane are plotted as a function of pressure. The solid lines are the linear fit to the data.

Figure 3.20 a) shows the intensity ratio of $I_{1130}/I_{1090}$, which is a representation of the population of trans and gauche conformers [47-49, 60-62]. The $I_{1130}/I_{1090}$ intensity ratio increases with increase in pressure suggesting an increase in TT (all-trans) population. These modes cease to exist beyond 12.3 due to the phase transition around 12.3 GPa. The discussions on gauche and trans conformer beyond this pressure will be now discussed based on fig 3.20. b).

**(iv) $CH_2$ and $CH_3$ Bending Region (1400-1500 $cm^{-1}$)**

The mode 1455 $cm^{-1}$ is related to the $CH_2$ and $CH_3$ bending while 1460 $cm^{-1}$ is related to the symmetric out-of-plane $CH_3$ bending mode. Figure 3.21 shows the Raman mode frequencies of these modes as a function of pressure. The pressure effects on the bending region of the spectra in the solid state are mainly due to relative changes in the conformational isomers [48]. These modes persist up to 16 GPa which is

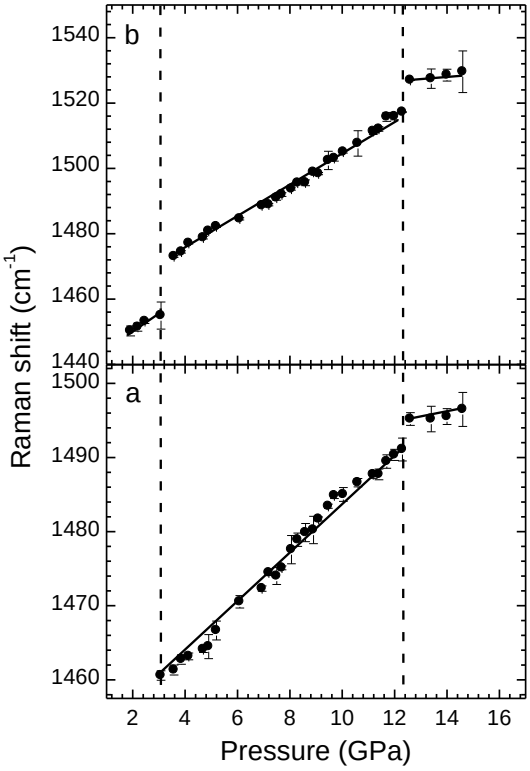


**Figure 3.21.** (a) $CH_2$ and $CH_3$ bending and (b) symmetric out-of-plane $CH_3$ bending modes as a function of pressure. The solid lines are the linear fit to the data.

similar to *n*-heptane. There is a distinct change in the mode frequency of these modes beyond 12.3 GPa, and they become stiff beyond 12.3 GPa.

### (v) $(CH_2)_n$ and $CH_3$ Stretching Region (2800-3100 $cm^{-1}$)

There are a bunch of modes appearing in the region 2800-3100 $cm^{-1}$, which are related to polymethylene stretching. These modes have a strong dependence on chain length of the hydrocarbon.

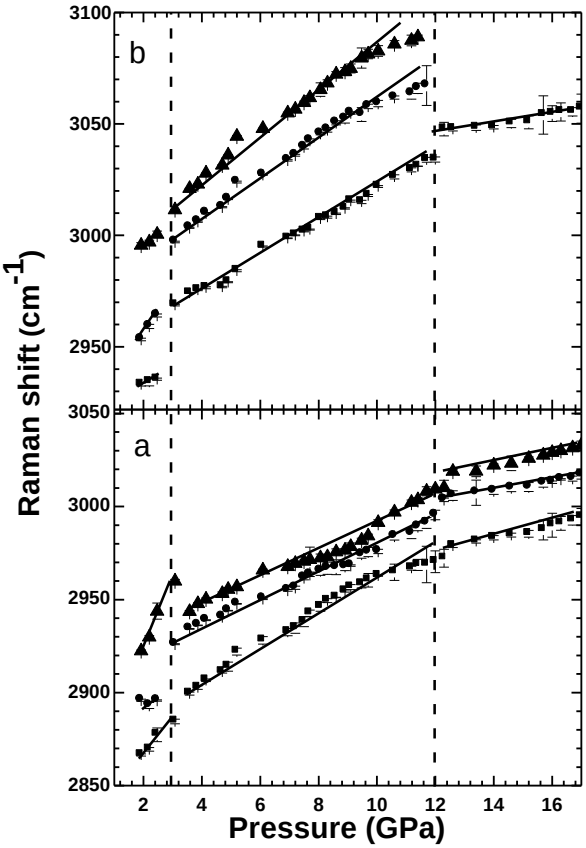


**Figure 3.22.** (a) $(CH_2)_n$ and (b) $CH_3$ stretching modes as a function of pressure. The solid lines are the linear fit to the data.

Figure 3.22 shows the pressure dependence of these modes. The symmetric methylene stretching mode involves three bands: (a) a narrower band at 2850 $cm^{-1}$ (TT), (b) a broadband at 2880 $cm^{-1}$ (TG), and (c) a shoulder near 2922 $cm^{-1}$ (TG) [45, 49]. The mode at 2940 $cm^{-1}$ (TG) is related to in-plane asymmetric methyl stretching, the mode at 2950 $cm^{-1}$ (TT) is related to out-of-plane asymmetric $CH_3$ stretching, and the mode at 2980 $cm^{-1}$ (TT) is due to asymmetric C-H stretching of $CH_3$ (skeletal plane mode) [45, 62].

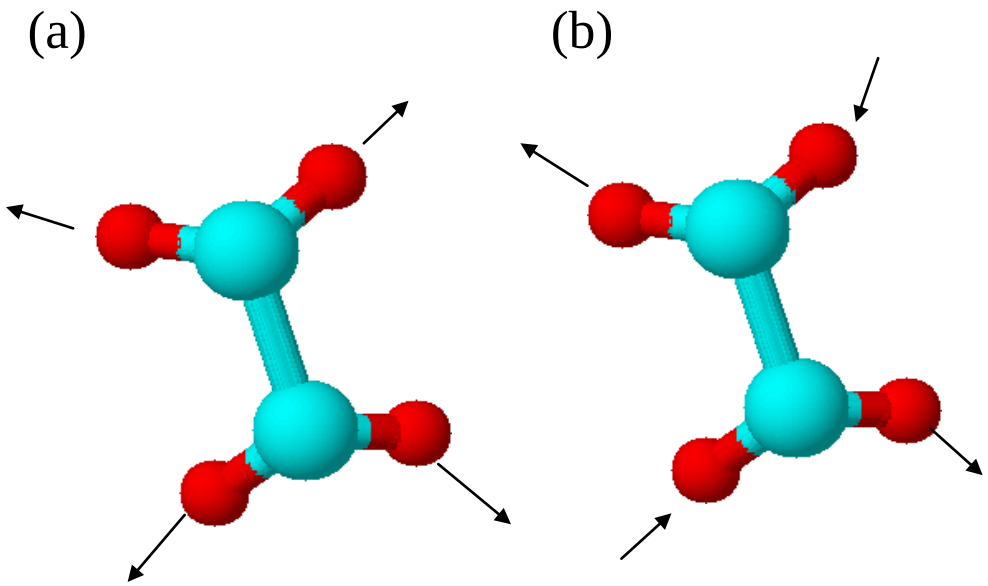


Figure 3.23. show schematic representation of (a) symmetric ($d^+$) and (b) anti-symmetric ($d^-$) methylene stretching respectively [49].

These modes are sensitive to alkyl chain conformation and chain packing arrangement [28, 63]. The changes in the Raman spectra in this region around 12.3 GPa suggest a possible phase transition because of conformational changes. We have plotted the relative intensity ratio of 2850 $cm^{-1}$ and 2922 $cm^{-1}$ mode ($I_{2850}/I_{2922}$) in Figure 3.20 b), which gives the populations of the two conformational isomers [54, 62]. There is a monotonous increase in this ratio in the solid phase between 3.0 and 12.3 GPa suggesting an increase in all-trans conformation population in this region. Beyond 12.3 GPa, this ratio starts to decrease. This is interesting and could mean an increase in gauche population. To the best of our knowledge, we do not know of any other system which shows an increase in the gauche population with an increase in pressure. We propose a possible way this could happen in *n*-pentane, the affect of this on n-pentane and the resulting phase transition. This will be discussed in comparison with n-heptane and n-hexane.

### 3.5. Discussion

In the case of molecular solid, the Raman spectrum is sensitive to the changes in the inter- and intra-molecular vibrations because of conformations. The application of pressure on liquid *n*-alkane increases the inter-molecular potential through increase in van der Waal forces and increase in intra-molecular potential because of decrease in bond distance as a result of the decrease in volume. Based on the results of the high pressure Raman studies on n-heptane, n-hexane and n-pentane, we observe that the liquid to solid transition is similar to earlier report [4, 11, 25-28]. The transition pressure for both n-heptane and n-hexane occur at around the similar pressure range, but in the case of pentane it occurs at a higher pressure. This is important because n-pentane due to its small size is able to retain its mobility at higher compaction. This is also the reason why n-pentane crystallizes differently from higher alkanes. All the n-alkanes studied in this chapter exhibit a solid to solid transition with increasing pressure. The transition pressure decreases with increasing chain length namely, 7.5 GPa for n-heptane, 9.1 GPa for n-hexane and 12.3 GPa for n-pentane. The decrease in transition pressure with increase in chain length is an expected one. As the chain length increases, the steric interferences increase at relatively low pressures or decreasing volume, leading to the phase transition.

Based on the Raman mode behaviors discussed in the earlier section, we suggest that at lower volume, the n-alkanes studied in this chapter, due to the molecules being linear chains pack closely perpendicular to the chain length at first. Result of this is an increase in trans configuration at the expense of gauche conformation. It is well known that when n-alkane solidifies, the molecules prefer to retain gauche conformation. But in reduced volume, gauche conformation increases steric hinderances, leading to more trans conformation. This observation is supported by the changes in intensities of the Raman modes related to gauche and trans conformers [see figures 3.13, 3.20]. As the pressure is increased further the volume reduction is achieved by decrease in distances between molecules along the chain length. In liquid and in the solid phase, the $CH_3$ end group of n-alkane is free to rotate and these lead to the rotational and torsional modes associated with $CH_3$ end groups in Raman spectra of n-alkanes. With increase in pressure the execution of these vibrations tend to be hindered. Hence one should expect a dampening

of these modes at higher pressure. This was observed in the MD simulation work of Krishnan *et al* [26] on n-heptane. Upon further increasing pressure, these modes freeze. The freezing of the $CH_3$ torsional modes are observed in n-alkanes studied in this chapter, deduced from the disappearance of these modes in their respective Raman spectra.

The freezing of $CH_3$ end group, which is tetrahedral in coordination, could introduce disorder at higher pressure. Since rotational degree of freedom of $CH_3$ end group gives the crystal a higher ordering at low pressure, phase II could be called an orientationally ordered state. Upon freezing, the phase III could be called an orientationally disordered state. So in each of n-heptane, n-hexane and n-pentane the solid to solid state is an orientational order-disorder transition driven by freezing of $CH_3$ end group. The structure of n-alkane would have no or very little change and hence the transition is second order in nature. This is corroborated by the behavior of $CH_2$ and $CH_3$ stretching modes, $CH_2$ and $CH_3$ bending modes etc. All these modes remain even at higher pressure and show only a slope change ($d\omega/dP$) across the orientational order-disorder transition. The slope changes are mainly due to the increase in the stiffness of the bonds or execution of the vibration due to increased steric hindrances in the high pressure phase (phase III). This would lead to a lower value of $d\omega/dP$ as shown by Table (3.1-3.3).

In the case of both n-heptane and n-hexane, the high pressure phase (phase III) has the molecule in an all trans conformation. But in the case of n-pentane, we find that phase III has an increase in gauche conformation. This is an interesting observation, as at higher pressures per every system a trans conformation is the lowest energy conformation. We relate this analogy to the small size of the carbon chain and n-pentane being the first mid chain alkane which is a liquid. It is also worth pointing out here that n-pentane tends to solidify with the chain being non parallel (a percentage of them) [64]. It is important to note that as in the case of n-heptane and n-hexane an increase of pressure leads to an increase in trans conformation at the transition, where the $CH_3$ end groups freeze. Since the n-pentane retains a non parallel chain packing due to its small size [65] helps the n-pentane to have an end gauche conformation to reduce steric hindrance.

On the basis of the symmetry operations, one can predict the chain packing, and it has been shown that in the case of crossed chain alkanes like *n*-pentane, the density of van der Waal contacts between the chain rows is minimal which requires end gauche conformation in its crystal structure [66]. A similar argument could be used for *n*-pentane at high pressures where the gauche conformers help in better packing in high density condition leading to a disordered phase above 12.3 GPa. High-pressure Brillouin studies on 1:1 pentane/isopentane up to 12 GPa, which is used as a hydrostatic medium in high-pressure experiments, shows a glass transition around 7 GPa [67]. This suggests that *n*-pentane could develop disorder at higher pressure.

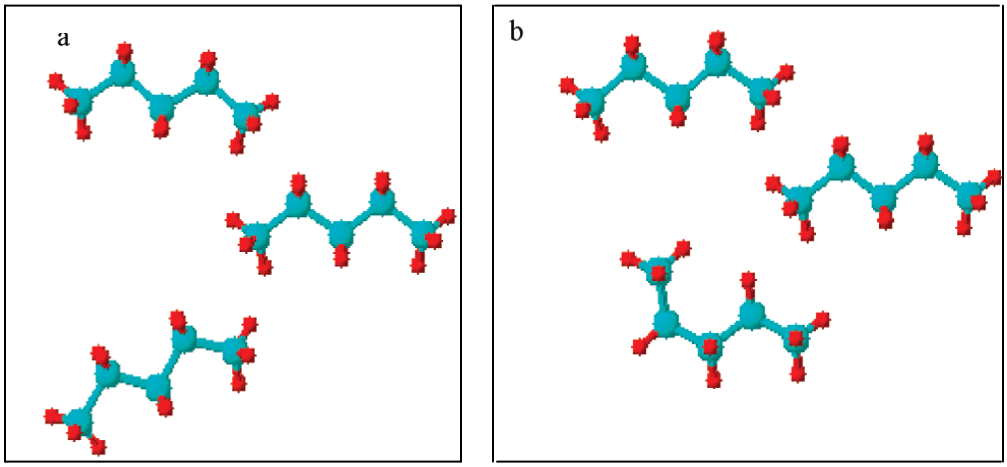


**Figure 3.24.** The schematic representation of possible *n*-pentane molecular arrangement at pressures (a) below and (b) above the transition pressure of 12.3 GPa.

Figure 3.24. shows the schematic representation of the *n*-pentane at pressures a) below and b) above the transition pressure of 12.3 GPa. In this schematic, we suggest that the gauche defects are mostly end gauche and are associated with those molecules which are not aligned parallel to the long axis in the low-pressure phase. This could lead to a very small reduction in volume. It has been seen from our experiments that the sample does not show any large change in volume across this transition, since we do not observe any micro cracks in the sample. It has been seen in the NMR studies on *n*-pentane that in the temperature region 70-143.4 K the second moments of the absorption lines were found to be smaller than the computed rigid lattice values throughout the temperature range. It has been suggested that the lower value is achieved by the reorientation of the methyl group

at the end of each molecule about the adjacent C-C bond [65]. This could mean that molecular rearrangements at the end of the molecule are possible in *n*-pentane in the solid form. Thus we suggest that in *n*-pentane, we expect a fraction of the TG conformation in the all-trans conformation by molecular rearrangement above 12.3 GPa [65]. Additionally, using valence force field calculations, Snyder has calculated the vibrational frequencies of *n*-pentane at 143 K temperature and has found six bands associated with the molecule in GG state [45]. This again suggests that *n*-pentane unlike other *n*-alkanes tends to have end gauche configuration for effective packing.

### 3.6. Conclusions

In conclusion, we observe a solid-solid transition in all the mid chain n-alkanes. We have studied their change in intra-molecular vibrational behavior as a function of pressure. Upon application of pressure all the n-alkanes in the present case showed a large change in their torsional mode associated with methyl end groups. The close packing of these n-alkanes leads to freezing of the methyl end groups leading to a solid-solid transition which is characterized an orientationally order-disorder transition. The transition pressure decreases with increase in chain length which is an expected one. The most interesting observation is that unlike normal n-alkanes, in n-pentane dense packing introduces end gauche conformation in the disordered phase. This could be related to the difference in their crystal structure in the solid phase as well as the chain length. The solid-solid transition observed in n-alkanes is second order in nature and would involve no or very little volume change.

### 3.7. Bibliography

1) Small, D. M. *The Physical Chemistry of Lipids*; Plenum Publishing: New York, 1988.

2) Chapman, D.; Jones, M.; Micelles, M. N. *Monolayers and Biomembrane*; John Wiley: New York, 1984.

3) Dagaut, P.; Reuillon, M.; Cathonmet, M. *Combust. Sci. Technol.***1994**, *95*, 233.

4) Qiao, E.; Zheng, H. *Appl. Spectrosc.* **2005**, *59*, 650.

5) Hunt, J. M. *Petrol. Geochem. Geol.* **1979**, 31-35.

6) White, C. M.; Jensen, K. L.; Rohar, P. C.; Tamilia, J. P.; Shaw, L. J.; Hickey, R. F.

*Energy Fuels* **1996**, *10*, 1067.

7) Rhlid, R. B.; Matthey, D. W.; Blank, I.; Fay, L. B.; Juillerat, M. A. *J. Agric. Food Chem.* **2002**, *50*, 4087.

8) Ganiev, I. M.; Timerghazin, Q. K.; Khalizov, A. F.; Andriyashina, N. M.; Shereshovets, V. V.; Volodarsky, L. B.; Tolstikov, G. A. *Tetrahedron Lett.* **1999**, *40*, 4737.

9) Tkachev, S. N.; Bass, J. D. *J. Chem. Phys.* **1996**, *104*, 10059.

10) Zeto, R. J.; Vanfleet, H. B. *J. Appl. Phys.* **1969**, *40*, 2227.

11) Gelles, S. H. *J. Chem. Phys.* **1968**, *48*, 526.

12) Allen. A. O; Natl. Stand. Ref. Data Sys. Vol. 58 of Natl. Bur. Stand. (U.S. GPO, Washington, D.C., 1976) Nishikawa. M; *Electrons in CondensedMedia*, Chap. 5 of *CRC Handbook of Radiation Chemistry*, edited by Y. Tabata *et al.* (CRC Press, Boca Raton, 1991)

13) Kengo. I; Nishikawa. M; Richard. A. H. *J. Chem. Phys*. **1996**, 104, 1545.

14) David. A. P; Trevor. J. G; Dennis. C. *Biochemistry*. **1980**, 19, 349.

15) Edmundo. C; Valerie. C. D. Alain. M. *J. Am. Oil Chem. Soc*. **1998**, 75, 309.

16) Soumanou. M. M; Bornscheuer. U. T. Eur. *J. Lipid Sci. Technol*. **2003**, 105, 656.

17) Prycek. J; Ciganek. M; Simek. Z. *J. Chromatog*r. **2004**, A 1030, 103.

18) Ramadan. M. F; Morsel. J. T. *Photochem. Anal*. **2003**, 14, 366.

19) Komprda. T; Zelenka. J; Fajmonova. E; Bakaj. P; Pechova. P. *J. Agric. Food. Chem*. **2003**, 51, 7692.

20) Sirota, E. B.; King, H. E., Jr.; Hughes, G. J.; Wan, W. K. *Phys. Re*V. *Lett.* **1991**, *68*, 492.

21) Ryckaert, J. P.; Klein, M. L.; McDonald, I. R. *Phys. Re*V. *Lett.* **1987**, *58*, 698; *Mol. Phys.* **1994**, *83*, 439.

22) Yamomoto, H.; Nemoto, N.; Tashiro, K. *J. Phys. Chem. B* **2004**, *108*, 5827.

23) Guillaume, F.; Ryckaert, J. P.; Rodriguez, V.; MacDowell, L. G.; Girard, P.; Dianoux, A. *J. Phase Transitions* **2003**, *76*, 823.

24) Boese, R.; Weiss, H. C.; Bla¨ser, D. *Angew. Chem., Int. Ed.* **1999**, *38*, 988.

25) Yamaguchi, M.; Serafin, S. V.; Morton, T. H.; Chronister, E. L. *J.Phys. Chem. B* **2003**, *107*, 2815.

26) Krishnan, M.; Balasubramanian, S. *J. Phys. Chem. B* **2005**, *109*, 1936.

27) Kato, M.; Taniguchi, Y. *J. Chem. Phys.* **1991**, *94*, 4440.

28) Huai, W.; Haifei, Z.; Qiang, S. *Applied Spectroscopy* **2005**, 59, 1498.

29) Mao, H. K.; Bell, P. M. *Year Book*sCarnegie Inst. Washington **1978**, *77*, 904.

30) Barnett, J. D.; Block, S.; Piermarini, G. J. *Re*V. *Sci. Instrum.* **1973**, *44*, 1.

31) Kavitha, G.; Vivek, S. R. C.; Govindaraj, A.; Narayana, C. *Proc.Indian Acad. Sci. (Chem. Sci.)* **2003**, *115*, 689.

32) G.V. Pavan Kumar and Chandrabhas Narayana**,** Current Science **2007,** 93, 778-781.

33) Mayo, D. W.; Miller, F. A.; Hannah, R. W. *Course Notes on the Interpretation of Infrared and Raman Spectra*; John Wiley & Sons: New York, 2004.

34) Casal, H. L.; Mantsch, H. H.; Cameron, D. G.; Snyder, R. G. *J.Chem. Phys.* **1982**, *77*, 2825.

35) Wong, P. T. T.; Mantsch, H. H.; Snyder, R. G. *J. Chem. Phys.***1983**, *79*, 2369.

36) Snyder, R. G.; Cameron, D. G.; Casal, H. L.; Compton, D. A. C.; Mantsch, H. H. *Biochim. Biophys. Acta* **1982**, *684*, 111.

37) Brown, K. G.; Brown, E. B.; Ladjadj, M. *J. Phys. Chem.* **1987**, *91*, 3436.

38) Wallach, D. F. H.; Verma, S. P.; Fookson, J. *Biochim. Biophys.Acta* **1979**, *559*, 153.

39) Maroncelli, M.; Strauss, H. L.; Snyder, R. G. *J. Chem. Phys.* **1985**, *82*, 2811.

40) Heinz, G.; Fanconi, B. *J. Chem. Phys.* **1973**, *59*, 534.

41) Norman N.; Mathisen H. Acta Crystallogr, **1960**, 13, 1043.

42) Patrick. T. T. W; Mantsch. H. H. *J. Chem. Phys*. **1983**, 79, 2369.

43) Huang. Y; Wang. H. *Langmuir*, **2003**, 19, 9706.

44) Hibbon. J. H. *Chem. Rev*. **1935**, 18, 11.

45) Snyder, R. G. *J. Chem. Phys.* **1967**, *47*, 1316.

46) Kint, S.; Scherer, J. R.; Snyder, R. G. *J. Chem. Phys.* **1980**, *73*, 2599.

47) Schoen, P. E.; Priest, R. G.; Sheridan, J. P.; Schnur, J. M. *J. Chem.Phys.* **1979**, *71*, 317.

48) Yamaguchi, M.; Serafin, S. V.; Morton, T. H.; Chronister, E. L. *J.Phys. Chem. B* **2003**, *107*, 2815.

49) Snyder, R. G.; Scherer, J. R. *J. Chem. Phys.* **1979**, *71*, 3221.

50) 50) Braden, D. A.; Parker, B. S.; Hudson, B. S. *J. Chem. Phys.* **1999**, *111*, 429.

51) Logan, K. W.; Danner, H. R.; Gault, J. D.; Kim, H. *J. Chem. Phys.* **1973**, *59*, 2305.

52) Snyder, R. G.; Strauss, H. L.; Alamo, R.; Mandelkern, L. *J. Chem.Phys.* **1994**, *100*, 5422.

53) Brown, K. G.; Bicknell-Brown, E.; Ladjadj, M. *J. Phys. Chem.***1987**, *91*, 3436.

54) Snyder, R. G. *J. Chem. Phys.* **1982**, *76*, 3342.

55) Qiao, E.; Zheng, H. *Appl. Spectrosc.* **2005**, *59*, 650.

56) Gelles, S. H. *J. Chem. Phys.* **1968**, *48*, 526.

57) Yamaguchi, M.; Serafin, S. V.; Morton, T. H.; Chronister, E. L. *J.Phys. Chem. B* **2003**, *107*, 2815.

58) Painter, P. C.; Coleman, M. M.; Koenig, J. L. *The Theory of Vibrational Spectroscopy and its Application to Polymeric Materials;* John Wiley: New York, 1982.

59) MacPhail, R. A.; Strauss, H. L.; Snyder, R. G.; Elliger, C. A. *J.Phys. Chem.* **1984**, *88*, 334.

60) Snyder, R. G.; Cameron, D. G.; Casal, H. L.; Compton, D. A. C.; Mantsch, H. H. *Biochim. Biophys. Acta* **1982**, *684*, 111.

61) Pink, D. A.; Green, T. J.; Chapman, D. *Biochemistry* **1980**, *19*, 349.

62) Wallach, D. F. H.; Verma, S. P.; Fookson, J. *Biochim. Biophys.Acta* **1979**, *559*, 153.

63) Pratt, L. R.; Hsu, C. S.; Chandler, D. *J. Chem. Phys.* **1978**, *68*, 4202Snyder, R. G. *J. Chem. Phys.* **1982**, *76*, 3342.

64) Mathisen, H.; Norman, N.; Pederson, B. F. *Acta Chem. Scand.* **1967**, *21*, 127.

65) Rushworth, F. A. *Proc. R. Soc. London, Ser. A* **1954**, *222*, 526.

66) Segerman, E. *Acta Crystallogr.* **1965**, *19*, 789.

67) Oliver, W. F.; Herbst, C. A.; Lindsay, S. M.; Wolf, G. H. *Phys.Re*V. *Lett.* **1991**, *67*, 2795.

# CHAPTER-IV

# High Pressure Raman Study of Perfluorohexane and Perfluoroheptane

**This chapter constitutes the work will be published in**

**G. Kavitha and Chandrabhas Narayana**
**Journal of Physical Chemistry B submitted (2007).**

## 4.1. Motivation

In recent years, the interesting topic which draws every one's attention is the molecular orientation of simple hydrocarbons and perfluorocarbons at different high pressure phases. Perfluorocarbons have analogous molecular structure to simple hydrocarbons where all the hydrogen atoms are replaced by fluorine atoms [1]. The industrial use is mainly linked to the electronic and computer industry [2-6] where the bonding nature is important for the poly perfluoroethane to act as lubricant between magnetic hard disks and heads. Though perfluorocarbons have variety of potential applications in computer industry as lubricant, binary and ternary mixtures of liquid thin films and obtaining plastic crystals from molecular solids and so on [7-9]. The number of investigations on perfluorocarbons is very less. Temperature dependent vibrational behavior of perfluorocarbons has been studied by Rey-Lafon and co-workers [10, 11]. Subjecting various types of matter to external pressure and utilizing Raman spectroscopic technique as the diagnostic tool, one can obtain the valuable information like intermolecular interaction, phase transition and structural changes. The existence of solid–solid transition in short chain and long chain perfluorocarbons under temperature has been reported earlier [12-15]. In spite of the properties like boiling point, vaporization energy, dipole moments and electron polarizability of alkanes and perfluoroalkanes being same [16, 17], their conformational properties are more complex at the ordered and the disordered states due to perfluorocarbons helical nature. So it is necessary to investigate the conformational characteristics and phase behavior of perfluorocarbons with pressure to compare it with their hydrocarbon analogy. Due to this reason, we have carried out high pressure Raman studies on medium chain perfluorohexane and per- fluoroheptane till 12 GPa. We observe a liquid–solid transition at 1.6 GPa and solid to solid transition at 8.2 GPa for perfluorohexane. In comparison a liquid – solid transition at 1.3 GPa, and a solid-solid transitions at 3.0 GPa and at 7.0 GPa is observed in the case of perfluoroheptane. The conformational and phase behavior at different high pressure phases of these perfluorocarbons are discussed.

## 4.2. Results

Though some of the perfluorocarbon's properties are similar to simple hydrocarbons, the structure is little bit different from hydrocarbons [21]. Figure 4.1(a-b) shows the difference in molecular structure of hexane and perfluorohexane as a representative. The perfluorocarbon adopt a helical structure due to greater van der Waals

(a) (b)

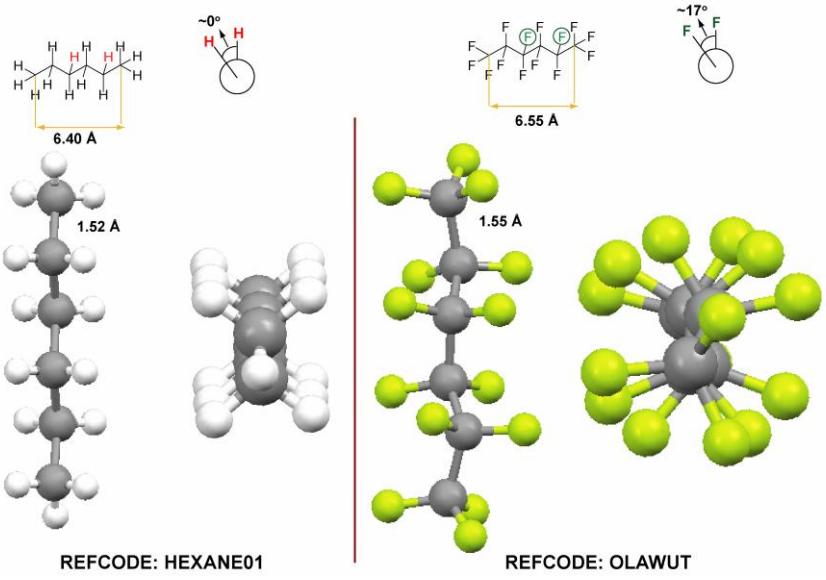


**Figure 4.1**. show the molecular structure of (a) Hexane, (b) Perfluorohexane

radius of fluorine atom compared to hydrogen atom in alkanes. Since the van der Waals radius of hydrogen atom is small, there will be lot of room for these atoms and they wont be able to touch each other (see figure 4.1-a). But in the case of perfluorocarbon, the atoms which are attached to the carbon back bone appeared to be over crowded due to greater van der Waals radius of fluorine atom [22]. To overcome this problem, the molecules adjust themselves with the rotation of the chain bonds to create distance between the neighboring flourine atoms (see figure 4.1-b). Hence the helical structure. Due to this reason, the back bone dihedral angles for the trans conformation are shifted by about 17˚ from the true trans angle [23]. The pressure studies on the perfluorohexane

and perfluoroheptane has performed up to a pressure of 12 GPa to investigate the structure of rotational isomers as a function of pressure.

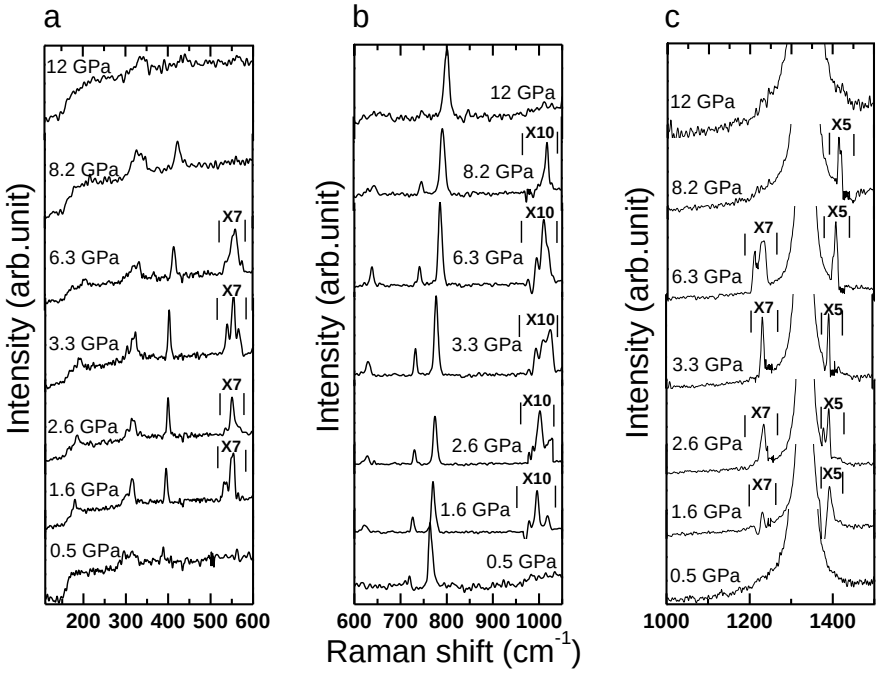


**Figure 4.2.** Raman spectra of perfluorohexane recorded at ambient conditions and at high pressures. For clarity the spectra has been divided into three regions (a) 100-600 $cm^{-1}$, (b) 600-1000 $cm^{-1}$ and (c) 1000-1500 $cm^{-1}$. The 1200–1400 $cm^{-1}$ region is dominated by diamond first-order peak and has not been shown.

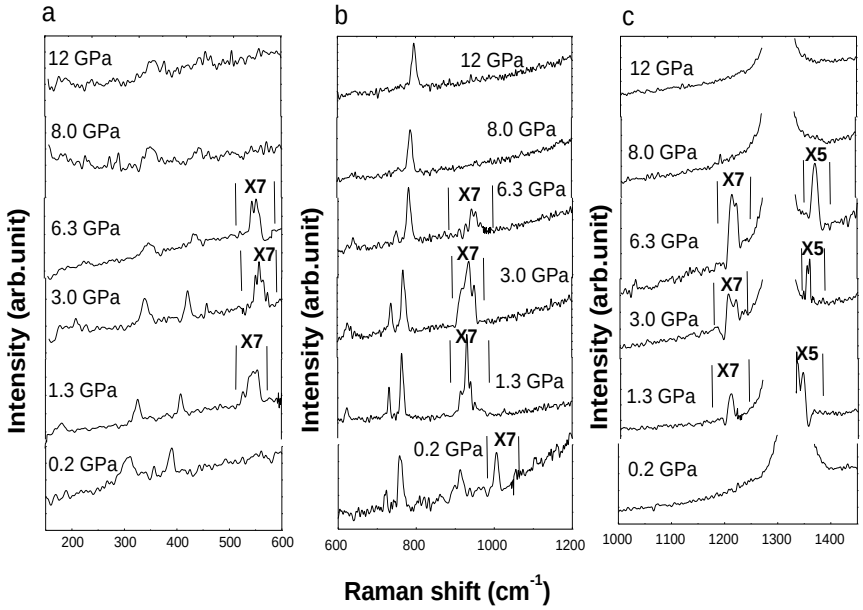


**Figure 4.3.** Raman Spectra of perfluoroheptane recorded at ambient conditions and at high pressures. For clarity the spectra has been divided into three regions (a) 100-600 $cm^{-1}$, (b) 600-1200 $cm^{-1}$ and (c) 1000-1500 $cm^{-1}$. The 1200–1400 $cm^{-1}$ region is dominated by diamond first-order peak and has not been shown.

Figure (4.2&4.3) shows the Raman spectra in the spectral region (100 – 1500 $cm^{-1}$) for perfluorohexane and perfluoroheptane at ambient and high pressures. The Rayleigh cut off for 180° back scattering was limited by the use of edge filter and dichroic mirror to 100 $cm^{-1}$ and hence the spectrum starts at 100 $cm^{-1}$. The region around 1330 $cm^{-1}$ is dominated by diamond peak and hence has been deleted for clarity.

**TABLE 4.1.** Frequency (ω) of the Raman modes of Perfluorohexane, and its pressure derivative (dω/d*P*) observed in the various phases are shown below respectively. Their mode assignments are also given based on Ref. [10-11, 24-30].

| **Phase I (0.5 GPa)** | | **Phase II (>1.6 GPa)** | | **Phase III (>8.2 GPa)** | | **Mode assignment** |
|---|---|---|---|---|---|---|
| ω ($cm^{-1}$) | dω/dP | ω ($cm^{-1}$) | dω/dP | ω ($cm^{-1}$) | dω/dP | |
| | | 180 | 5.2 | | | LAM C-C-C angle bending |
| 295 | 9.0 | 298 | 5.5 | 330 | 3.8 | $CF_2$ Wagging (TTT) |
| 313 | 7.7 | 312 | 3.7 | 339 | 4.4 | $CF_2$ Twisting (TTT) |
| 327 | 0.2 | 332 | 7.5 | | | $CF_2$ Twisting (TTT) |
| 385 | 1.3 | 395 | 3.4 | 425 | 4.5 | $CF_2$ Bending (TTT) |
| | | 552 | 3.0 | | | $CF_3$ Rocking (TTT) |
| 615 | 5.8 | 627 | 2.7 | 647 | 0.1 | Asymmetric $CF_3$ bending (TTT) |
| 680 | 0.6 | 682 | 1.2 | | | Chain Stretching (TTG) |
| 719 | 0.8 | 726 | 2.7 | 747 | 4.8 | Symmetric $CF_2$ stretching (TTT) |
| 768 | 3.6 | 769 | 2.6 | 792 | 2.7 | Symmetric $CF_3$ stretching (TTT) |
| | | 995 | 3.5 | | | $CF_3$ stretching and bending (TTG) |
| 1224 | 9.7 | 1230 | 1.5 | | | Asymmetric $CF_2$ stretching (TTG) |
| 1383 | 0.6 | 1388 | 3.8 | 1413 | 3.8 | Symmetric C-C stretching (TTG) |

**TABLE 4.2.** Frequency (ω) of the Raman modes of Perfluoroheptane, and its pressure derivative (dω/d*P*) observed in the various phases are shown below respectively. Their mode assignments are also given based on Ref. [10-11, 24-30].

| **Phase I (>0.2 GPa)** | | **Phase II (>1.3 GPa)** | | **Phase III (>3.0 GPa)** | | **Phase IV (>7.0 GPa)** | | **Mode assignment** |
|---|---|---|---|---|---|---|---|---|
| ω ($cm^{-1}$) | dω/ dP | ω ($cm^{-1}$) | dω/ dP | ω ($cm^{-1}$) | dω/dP | ω ($cm^{-1}$) | dω/dP | |
| | | 152 | 7.9 | 167 | 3.8 | | | LAM C-C-C angle bending |
| 310 | 4.3 | 307 | 1.8 | 310 | 1.8 | 314 | 2.5 | $CF_2$ Twisting (TTTT) |
| 349 | -5.5 | 361 | 3.7 | 367 | 3.7 | | | $CF_2$ Rocking (TTTT) |
| 388 | 3.5 | 396 | 3.5 | 401 | 3.5 | 415 | 4.7 | $CF_2$ Bending (TTTT) |
| | | 550 | 1.4 | 552 | 1.4 | | | $CF_3$ Bending (TTTT) |
| | | 627 | 3.3 | 631 | 3.3 | 641 | 2.6 | Out of plane $CF_3$ Bending (TTTT) |
| 647 | -5.2 | 651 | 1.7 | 655 | 1.5 | | | Chain Stretching (TTTG)-regular helix |
| 719 | 3.3 | 733 | 3.4 | 736 | 3.4 | 750 | 2.9 | Symmetric $CF_2$ stretching (TTTT) |
| 755 | 4.0 | 765 | 2.4 | 769 | 2.4 | 782 | 3.8 | Symmetric $CF_3$ stretching (TTTT) |
| 914 | 8.8 | 927 | 13.0 | 946 | 0.5 | | | $CF_3$ stretching and bending (TTGT) |
| 1006 | 1.7 | | | | | | | $CF_3$ stretching and bending (TTTG) |
| | | 1236 | -5.3 | 1231 | 3.9 | | | Asymmetric $CF_2$ stretching (TTGT) |
| | | 1372 | 10.0 | 1388 | 4.0 | | | Symmetric C-C stretching (TTTG) |

The Raman spectra of perfluorohexane and perfluoroheptane have been compared with earlier reports [10-11, 24-30] and the mode assignments have been tabulated in Table 4.1&4.2. The modes observed can be clarified broadly into 3 catogories. 1) Low frequency modes or Longitudinal Acoustic Mode (LAM) (150-190 $cm^{-1}$), 2) Twisting, bending and wagging modes of $CF_2$ & $CF_3$ (350-620 $cm^{-1}$) and 3) stretching modes of $CF_2$ and $CF_3$ (700-1500 $cm^{-1}$). The bending, (twisting and wagging included) and stretching modes are having influence of gauche and trans conformation of the carbon back bone. And have been identified in Table 4.1&4.2. It is important to note that unlike hydrocarbons described in chapter 3, perfluorocarbons do not have a large number of gauche conformers. This is due to the helical nature. It is important to note that unlike their hydrocarbon analogs perfluorocarbons have only one gauche defect per chain for mid-chain hydrocarbon and as the chain length increases the mid gauche defect appears. Compare perfluorohexane and perfluoroheptane (Table 4.1&4.2)

### **4.2.1**. **Longitudinal Acoustic Mode (LAM – C-C-C- Angle Bending)**

The LAMs are related to the in-phase C-C-C bond angle expansion and contraction which is also known as accordian the mode. Like in n-alkanes, the property of this mode depends on the length of the chain [31-32]. Due to the Rayleigh cutoff (100 $cm^{-1}$), it is difficult to get all the low frequency modes for perfluorocarbon and restrict our discussion to these LAM modes. This mode seems to be very weak in liquid phase which is consistent with our results on alkanes described in chapter III [33-34]. We have been unable to follow LAM modes in liquid phase, but when the sample solidifies, the mode becomes intense and sharp. The LAM shifts to lower frequency with increase in chain length. Hence we observe LAM at 180 $cm^{-1}$ for $C_6F_{14}$ and 152 $cm^{-1}$ for $C_7F_{16}$. This evolution is characteristic of C-C-C angle bending mode [10-11, 35].

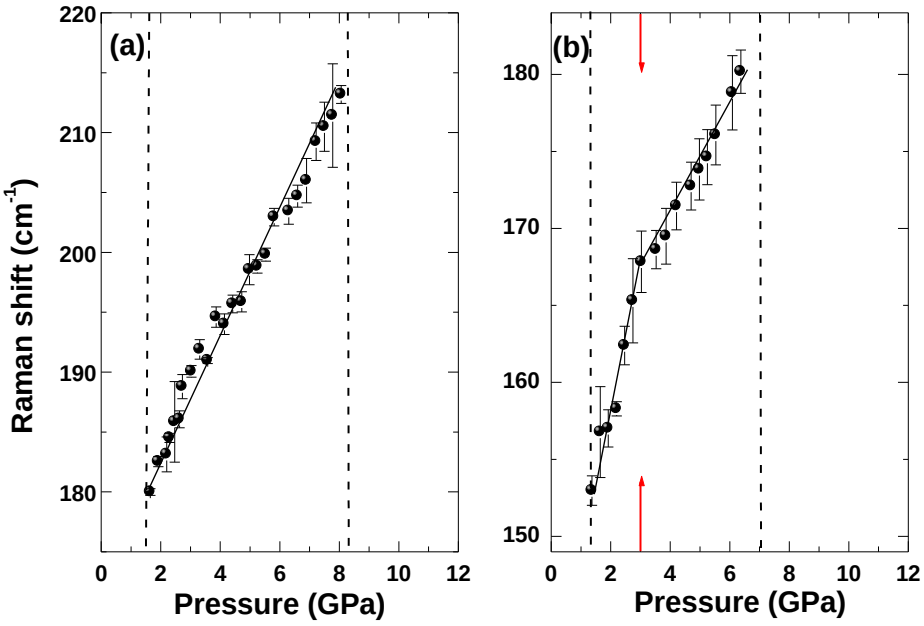


**Figure 4.4.** LAM mode as a function of pressure for (a) perfluorohexane and (b) perfluoroheptane. The solid lines through the data points are the linear fit to the data. The red color arrow indicate a possible phase transition for perfluoroheptane

The LAM mode behavior as function of pressure is shown in figure 4.4(a,b). As the pressure is increasd the mode hardens (increases in frequency). With increase in pressure bonds stiffen, hence the vibrational frequency increases. Since LAM involves all the carbon skeletal bonds the $d\omega/dP$ is large. It is interesting to note that in the case of $C_7F_{16}$ we observe a slope change around 3.0 GPa. This is important and we expect a phase transition in $C_7F_{16}$ at this pressure and will be discussed later. In both cases at very high pressures LAM modes disappear, 8.2 GPa in the case of $C_6F_{14}$ and 7.0 GPa in the case of $C_7F_{16}$.

### 4.2.2. $CF_2$ Wagging and Twisting Region

The region 200-400 $cm^{-1}$ is populated with wagging and twisting modes of $CF_2$ in perfluorocarbons. In the case of perfluorohexane, the $CF_2$ wagging mode is associated with 295 $cm^{-1}$ mode where as the modes at 312 and 327 $cm^{-1}$ are due to $CF_2$ twisting vibration. while in the case of perfluoroheptane, there are only two modes in the region at 310 and 349 $cm^{-1}$ associated with $CF_2$ twisting and rocking modes. These bands are attributed to the stable all-trans conformational isomer in the liquid phase [10-11].

These modes are unresolved and featureless in the liquid phase. But beyond 1.6 GPa for perfluorohexane and 1.3 GPa for perfluoroheptane, they became sharp and well resolved indicating a liquid–solid transition. Figure 4.5 shows the pressure dependence and the vertical dashed lines signify the phase transitions due to the observed changes in Raman spectra. As expected these modes harden with pressure. We do not see a major change in mode behavior at 3.0 GPa in these modes associated with perfluoroheptane.

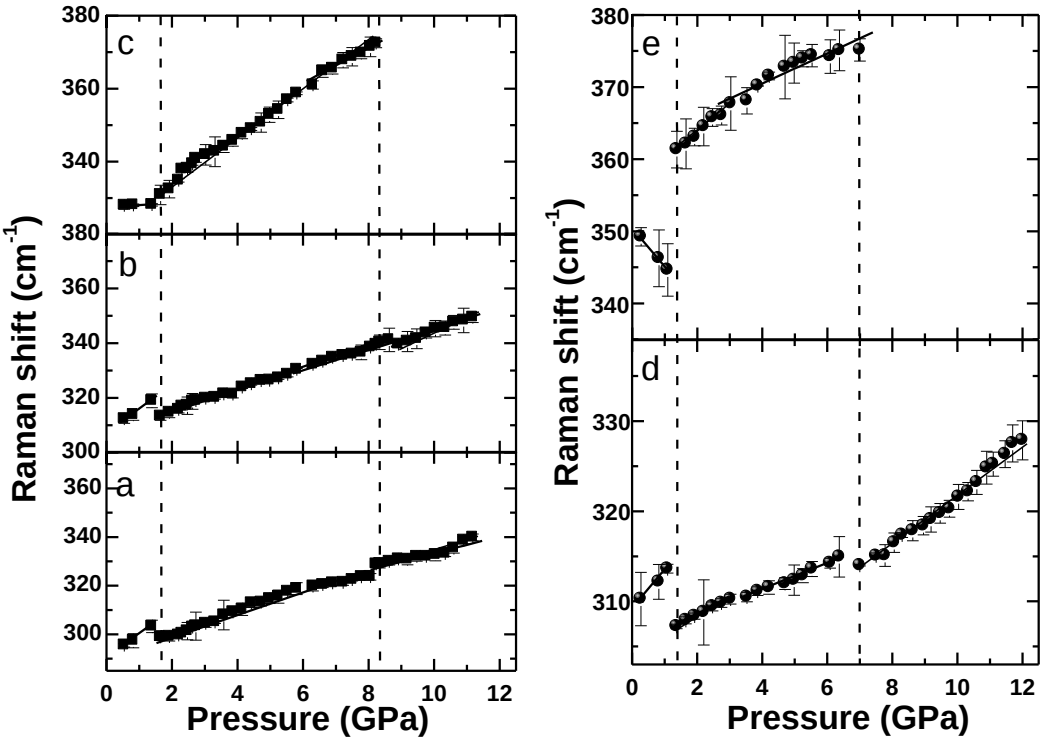


**Figure 4.5.** Pressure dependence of $CF_2$ wagging and Twisting modes (a-c) for perfluorohexane and (d-e) for perfluroheptane. The solid lines through the data points are the linear least square fit to the data.

At high pressures we observe that the $CF_2$ twisting modes disappear for both perfluoroalkanes due to the solid-solid transition around 8.2 GPa ($C_6F_{14}$) and 7.0 GPa ($C_7F_{16}$).

### 4.2.3. $CF_2$ and $CF_3$ Bending and Rocking Modes

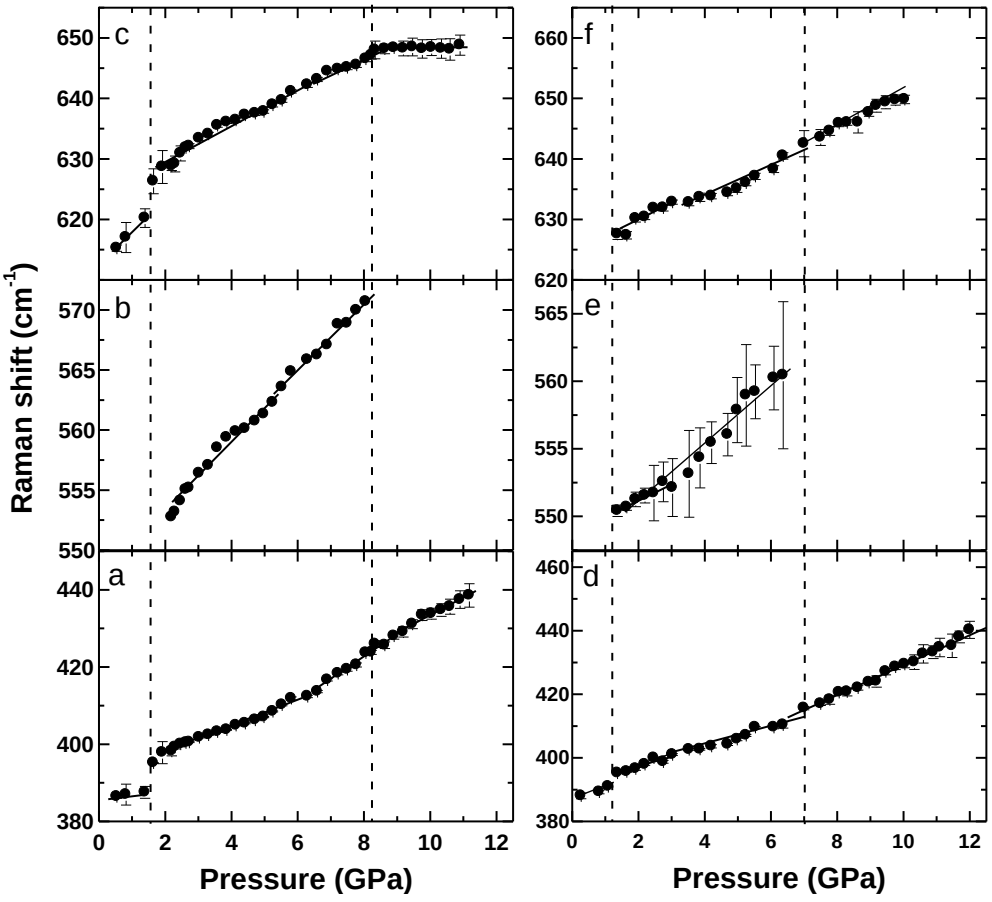


**Figure 4.6.** Pressure dependence of $CF_2$ & $CF_3$ bending and rocking modes of (a-c) for perfluorohexane and (d-f) for prefluoroheptane. The solid lines are the linear least square fit to the data.

The Raman modes between 380 – 620 $cm^{-1}$ at ambient conditions are related to $CF_2$ and $CF_3$ bending and rocking modes for a perfluorocarbons. These modes are attributed to chain packing and it reveals the order of chain termini at high pressure phase [36]. The 385, 552 and 617 $cm^{-1}$ (388, 544 and 613 $cm^{-1}$) modes are related to $CF_2$ bending, $CF_3$ rocking and $CF_3$ asymmetric bending vibration for perfluorohexane (perfluoroheptane) [37]. Pressure dependence of these modes is presented in fig 4.6. and the vertical dashed line suggest the phase transition based on the changes in Raman spectra at these pressures.

It is important to note that these modes are associated with all trans conformation. At 1.6 GPa (1.3 GPa) there is a change in frequency of these modes for perfluorohexane (perfluroheptane) and reduction in their full width half maximum (FWHM) suggesting a liquid to solid transition . Above 8.2 GPa for perfluorohexane and 7.0 GPa for perfluroheptane, the $CF_3$ rocking mode disappear suggesting a solid-solid transition which could be due to dense packing. Here too there is no major changes around 3.0 GPa for perfluoroheptane.

### 4.2.4. $CF_2$ and $CF_3$ stretching modes

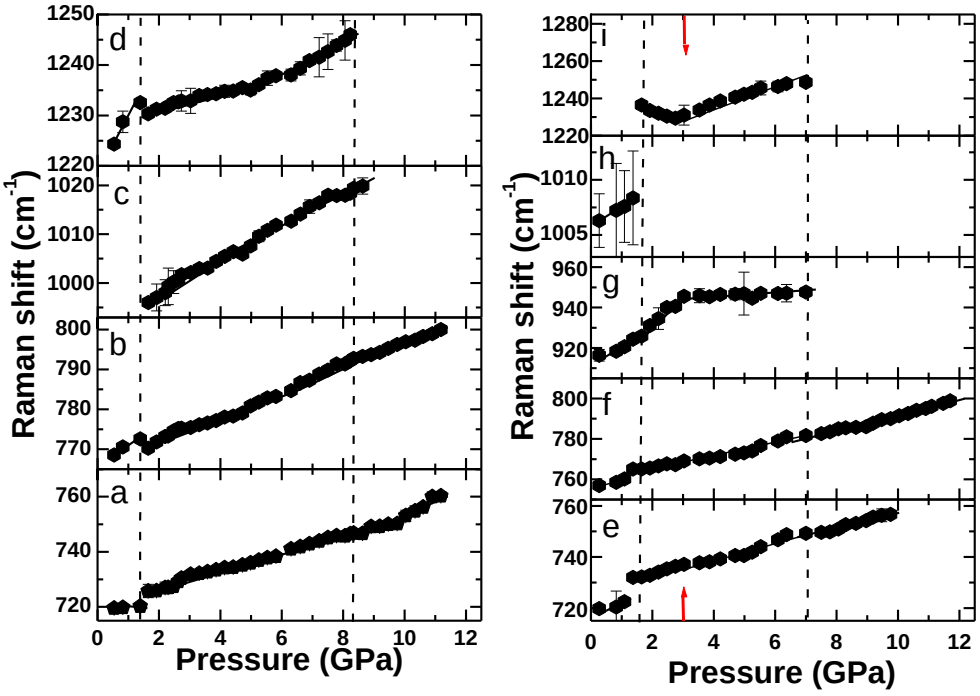


**Figure 4.7**. $CF_2$ and $CF_3$ stretching Raman modes as function of pressure (a-d) for perfluorohexane and (e-i) for perfluoroheptane. The solid lines are the linear least square fit to the data. The red color arrow in the second panel shows a possible phase transition.

The region between 700-1250 $cm^{-1}$ are populated with the modes related to the chain conformation and the chain packing [33-34]. There are three Raman bands for

perfluorohexane in this region which are a) 719 $cm^{-1}$ - symmetric $CF_2$ stretching (TTT), b) 763 $cm^{-1}$ – symmetric $CF_3$ stretching (TTT), c) 996 $cm^{-1}$ – $CF_3$ stretching and bending (TTG) which splits into two at higher pressure. But for perfluoroheptane, there are four modes observed in this region. They are (a) Symmetric $CF_2$ stretching (TTTT) at 719 $cm^{-1}$, (b) Symmetric $CF_3$ stretching (TTTT) at 755 $cm^{-1}$, (c) $CF_3$ stretching and bending (TTGT) at 916 $cm^{-1}$, and (d) $CF_3$ stretching and bending (TTTG)-1006 $cm^{-1}$. A new mode appears at 1236 $cm^{-1}$ related to Asymmetric $CF_2$ stretching (TTGT) in the solid phase at the expense of of 1006 $cm^{-1}$ mode. These modes are not well resolved in the liquid phase of perfluorocarbon. As per the figure 4.7 shows their pressure dependence and the vertical dashed lines show the phase transiton based on change in Raman spectra. The apperarnce of new modes at 1.6 GPa (1.3 GPa) for perfluorohexane (perfluoroheptane) and change in slopes signify the liquid-solid transition in these samples and their solid phase contains more than one conformer [10, 11]. The intensity ratio $I_{763}$(TTT)/$I_{993}$(TTG) of the bands belonging to different conformers shows the conformer population of different physical states of perfluorohexane [38].

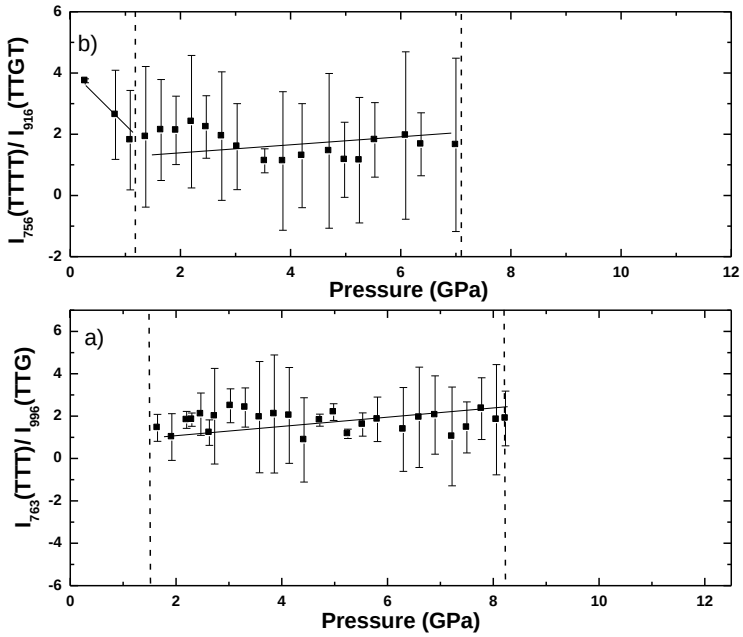


**Figure 4.8.** (a) The intensity ratio $I_{763}/I_{996}$ and (b) $I_{756}/I_{916}$ of *Trans* to *Gauche* conformational isomer of perfluorohexane and perfluoroheptane are plotted as a function of pressure. The solid lines are the linear least square fit to the data.

Figure 4.8 shows the intensity ratio of these modes for both perfluorocarbons. Disappearance of gauche modes at high pressure makes it difficult to calculate the ratio and signify the high pressure phase is all trans. It is important to point out here that the mode 916 $cm^{-1}$ and 1236 $cm^{-1}$ are related to mid gauche defects in perfluoroheptane and both these modes show a slope change around 3.0 GPa. Where as all the trans modes do not show any change. This suggest that in perfluoroheptane, since there exist two types of gauche defects, one mid chain and the other end gauche, there are two transition due to these conformers becoming trans conformers and occur at different pressures. It is intuitive to expect mid gauche to flip to all trans at lower pressure. In both perfluorocarbon at higher pressures 8.2 GPa in $C_6F_{14}$ and 7.0 GPa in $C_7F_{16}$ the end gauche mode disappear suggesting highest pressure has all trans conformer.

### 4.2.5. Skeletal C – C stretching region

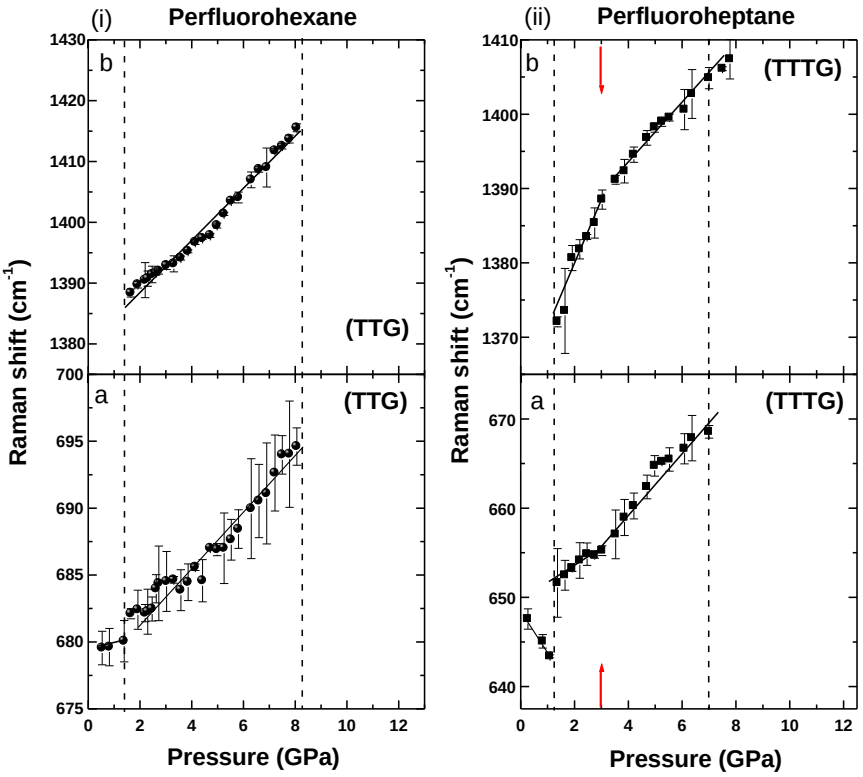


**Figure 4.9.** Pressure dependence of skeletal C-C stretching mode (a-b) for perfluorohexane and (c-d) for perfluoroheptane. The solid lines are the linear lease square fit to the data. The red color arrow in the second panel shows the possible phase transition.

Figure 4.9. shows the pressure dependence of skeletal C-C stretching mode. Like simple alkanes, these modes are conformational sensitive in perfluoroalkanes also the modes at 678 (648 $cm^{-1}$) and 1383 (1372$cm^{-1}$) are attributed to the end gauche conformers (TTG) in perfluorohexane (perfluoroheptane). These mode show a drastic change around liquid to solid transiton like other modes. The disappearance of end gauche modes at higher pressures again suggests that high pressure phase is an all trans phase in both the perfluorocarbons. In condensed phase it has been seen that perfluorohexane prefers to have a globular extended zig zag conformer [38]. In the case of perfluoroheptane the 1372 $cm^{-1}$ mode shows a slight change in slope around 3.0 GPa. We believe this could be due to presence of different gauche conformers associated with this molecular vibration.

**4.3. Discussions**

Based on the pressure dependence of various Raman modes associated with perfluorocarbons one can conclude that like their analogous hydrocarbons perfluorocarbons transform from liquid to solid transiton at relatively low pressures between 1-2 GPa. Also the solid phase formation depends on the chain length and the transition pressure is inversely proportional to chain length like n-alkanes. But the liquid to solid transition in both the analogs are similar [34]. At 1.6 GPa (1.3 GPa) perfluorohexane (perfluoroheptane) transforms from liquid to solid. In the liquid phase perfluorocarbons have all possible conformers which get frozen in the solid phase similar to their analogous hydrocarbon [39-40]. Due to the helical native, the gauche conformers are less in population, and multiple gauche defects in a single chain seldom occur.

The application of pressure causes two important phenomena in the molecular system [36]. 1) Increase in inter-molecular potential through van der Waals forces and 2) increase in intra-molecular potential through reduction in bond length. This could lead to the reduction in the volume of molecular system in the high pressure phase. Due to intermolecular interaction, it is expected that the large change will occur on lattice, acoustic and librational modes with pressure. We observe only LAM C-C-C angle bending and that too in the solid phase. This mode harden with pressure. The mode

behavior is different in perfluoroheptane. There is a slope change near 3.0 GPa. Based on the gauche conformer mode change discussed earlier, the C-C bond bending vibration would be affected due to mid gauche conformational change. Thus we observe a change in C-C LAM mode behavior at 3.0 GPa. Looking at the Raman mode behavior in the solid phase, one can generalize that in the case of perfluorocarbon with increasing pressure gauche conformer tend to transform to all trans form for better packing. In both perfluorohexane and perfluoroheptane we observe that the highest pressure phase has only all trans conformer vibrational modes. This leads to disappearance of the $CF_3$ rocking modes (550 $cm^{-1}$). This is significant. This suggests that in the dense state there is hindarance to $CF_3$ rotation similar to what was observed in n-alkanes.

Hence dense packing restricts end group rotation leading to an orientational disordered phase. The two phase are structurally equivalent and hence would not show any change until investigate carefully. Since perfluorocarbons are helical it is difficult to expect multiple gauche conformers present on a single chain like n-hexane and n-pentane. But on the chain length increases the probability of finding single gauche defects in different position increase. Due to rigid back bone, perfluorocarbons would have different conformational energies for presence of gauche conformer at different carbon positions. Hence it is possible to expect the conversion to occur at different packing fraction. This is the reason to observe the 3.0 GPa transition in perfluoroheptane. The mid-gauche have a change in mode behavior at this pressure. It is interesting to spectulate that as the chain length increases one would expect many more subtle transition before the perfluorocarbons transform completely to an all trans conformation with frozen end groups. This is quite different from the higher hydrocarbons. Similar observations have been made in temperature dependent vibrational studies on perfluorocarbons [10, 11, 41].

### 4.4. Conclusions

In conclusion, high pressure Raman spectroscopic studies on perfluorohexane and perfluoroheptane were performed up to 12 GPa. Perfluorocarbons undergo a liquid to solid transition in the pressure range of 1-2 GPa. The solid phase has both the trans and gauche conformers like hydrocarbon analogs. Due to the helicity, the number of gauche conformers are less. Perfluorohexane solidifies at 1.6 GPa where as perfluoroheptane at

1.3 GPa. Like their hydrocarbon analogs in the highest pressure phase the perfluorocarbons prefers to stay in all-trans state. This supported by the disappearance of all the gauche modes in the high pressure phase. In the densest phase, the perfluorocarbons like n-alkanes have end group freezing which is shown by the disappearance of $CF_3$ rocking modes. The perfluorohexane transform to an all trans phase at 8.2 GPa where as perfluoroheptane transforms at 7.0 GPa. Due to its rigid and helical structure, perfluoroheptane shows two transitions when compared to perfluorohexane. This is because the mid gauche conformation converts completely to all trans well before the end gauche. Like n-alkanes, the transition pressure is inversely proportional to the chain length in the case of perfluorocarbons too. We do not expect any volume changes across the transition and expect it to be reconstructive transitions.

**4.5. Bibliography**


1. Vandana. V; Rosenthal. D. J; Teja. A. S; Fluid. Phase. Equil. **1994**, 99, 209.
2. Walczak. M. M; Leavitt. P. K; Thiel. P. A. J. Amer.Chem.Soc. **1987**, 109, 5621.
3. Walczak. M. M; Thiel. P. A; Surf. Sci. **1989**, 224, 425.
4. Walczak. M. M; Leavitt. P. K; Thiel. P. A. Mate. Res. Soc.Symp. Proc. Volume Date 1988, 140 (New Mater. Approaches. Tribol.), **1989**, 417.
5. Walczak. M. M; Thiel. P. A. Spinger Ser. Surf. Sci. Volume date 1988, 17 (Adhes, Frict.) **1989**, 89.
6. Avery, N.R; Langmuir 1985, 1, 162.
7. Golden. W. G; Hunziker. H; de Vries. M. S; J. Phys. Chem. **1994**, 98, 1739.
8. Zhang. L; Siepmann J. I; J. Phys. Chem. B, **2005**, 109, 2911.
9. Smith. J. H; Pace. E. L; J. Phys. Chem. **1969**, 73, 2368.
10. Campos – vallettte M; Rey-Lafon. M; Lagnier. R; Chem. Phys. Lett. **1982**, 89, 189.
11. Campos – vallettte M; Rey-Lafon. M; J. Mol. Struct. **1984**, 118, 245.
12. Symposium Report on ”Plastic Crystals and Rotation in the Solid State,“ Phys. Chem. solids, **1961**, 18, 1.
13. Westrum. E. F; Jr. Pure Appl. Chem., **1961**, 2, 241; **1964**, 8, 187.
14. Stavely. L. A. K; Ann. Rev. Phys. Chem., **1962**, 13, 351.

15. Hsu. S. L; Reynolds. N; Bohan.S. P; Strauss. H. L; Snyder. R. G; Macromolecules, **1990**, 23, 4565.

16. Simons. J. H; Dunlap. R. D; J. Chem. Phys. **1950**, 18, 335.

17. Dunlap. R. D; Murphy Jr. C. J; Bedford. R. J; J. Am. Chem. Soc. **1958**, 80, 83.

18. Mao H.K; Bell. P.M; Carnegie Institution of Washington Year Book 77, 904 1978.

19. Mao. H. K; Xu. J; Bell. P. M; J. Geo. Res. **1986**, 91, 4673.

20. Pavan Kumar. G.V; Chandrabhas. N; Current Science. **2007**, 93,778.

21. Bunn. C. W; Howells. E. R; Nature, **1954**, 174, 549.

22. Smith. G. D; Jaffe. R. L; Yoon. Do. Y; Macromolecules, **1994**, 27, 3166.

23. Jang. S. S; Blanco. M; Goddard III. W. A; Caldwell. G; Ross. R. B; Macromolecules, **2003**, 36, 5331.

24. Koenig. J. L; Boerio. F. J; J. Chem. Phys. **1969**, 50, 2823.

25. Dixon, D. A; J. Phys. Chem. **1992**, 96, 3698.

26. Pace. E. L; Aston. J. G; J. Amer. Chem. Soc. **1948**, 70, 566.

27. Liang. C. Y; Krimm. S; J. Chem. Phys. 1**956**, 25, 563.

28. Boerio. F. J; Koenig. J. L; J. Chem. Phys. **1970**, 52, 4826.

29. Hannon. M. J; Boerio. F. J; Koenig. J. L; J. Chem. Phys. **1969**, 50, 2829.

30. Kobayashi. M; Sakashita. M; Adachi. T; Kobayashi. M; Macromolecules, **1995**, 28, 316.

31. Rabolt. J. F; Fanconi. B; Polymer, **1977**, 18, 1258.

32. Snyder. R. G; J. Chem. Phys. **1982**, 76, 3921.

33. Kavitha. G; Chandrabhas. N; J. Phys. Chem. B. **2007**, 111, 7003.

34. Kavitha. G; Chandrabhas. N; J. Phys. Chem. B. **2007**, 111, 14130.

35. Campos – vallettte M; Rey-Lafon. M; J. Mol. Struc. **1983**, 101, 23.

36. Kavitha. G; Chandrabhas. N; J. Phys. Chem. B, **2006**, 110, 8777.

37. Koenig. J. L; Boerio. F. J; J. Chem. Phys. **1970**, 52, 4170.

38. Szasz. G. J; J. Chem. Phys., **1950**, 18, 1417.

39. Brown. R.G; J. Chem. Phys. **1964**, 40, 2900.

40. Hyndman. D; Origlio. F. G; J. Appl. Phys. **1960**, 31, 1849.

41. Piaggio. P; francese. P. G; Masetti. G; Dellepiane. G; J. Mol. Struct. **1975**, 26, 421.

# CHAPTER-V

# Low Temperature Brillouin Studies on $PbWO_4$ and $BaWO_4$

**This chapter constitutes the work will be published in**

**G. Kavitha, Nandhini Garg, S.M. Sharma and Chandrabhas Narayana, Physical Review B (submitted) 2008.**

## 5.1. Motivation

Recently, rare earth molybdates and tungstates materials have been actively studied by scientist because of their pronounced acousto–optic applications and cryogenic phonon scintillation detectors [1-3]. These materials can be doped with rare–earth ions. Such doped crystals have great importance in current study of optical maser [4]. Isostructural divalent metal molybdates and tungstates are important host materials for a variety of inorganic phosphors [5]. These materials are the host crystals for laser [6]. Structural phase transition, change in physical properties and spontaneous symmetry breaking of perovskites and rare–earth molybdates have been actively investigated by vibrational spectroscopy and neutron scattering spectroscopy [7-16]. Scheelite structured tungstates and molybdates are the main focus of recent spectroscopic studies at high temperature and high pressure, which exhibit several phase transitions [17]. However, it is still little known on their acoustic properties and its temperature behavior. It is relevant to study the similarities and differences among the structures belonging to the same type. It might help to determine the factors involved in structure stability. Further the influence of cation on the crystal structure can help in modeling the effect of impurities on the physical properties [18]. The introduction of cationic impurities in the host crystal can achieve the laser light emission at desired frequencies [19]. The impurity strongly affects the emission properties of the crystal. Therefore the study of structural distortion in cation coordination can provide useful information for crystal growth and better understand of the fine structure of the emission lines [20].

To know about the nature of acoustic phonon behavior coupled with electronic states, Brillouin spectroscopy could be used. Since defects in cationic sites could have strong effect on the elastic properties signifies the phase transition [21, 22]. We have performed performed Brillouin studies on $PbWO_4$ and $BaWO_4$ as a function of low temperature ranging from 20 K to 320 K. In $PbWO_4$, we observe a phase transition around 180 K where as in the case of $BaWO_4$, we observe two phase transitions are at 240 K and the other at 130 K. The reason for the phase transitions are the basis for this thesis.

## 5.2. Materials and Experimental details

$PbWO_4$ crystal is grown in AT&T Bell laboratories, New Jersey as large single crystals by Czochralski technique [23]. $BaWO_4$ was made by the standard solid state route. Barium carbonate and tungsten oxide are mixed in their stochiometric ratios and are finely ground together and then heated in a furnace. The $PbWO_4$ and $BaWO_4$ crystals for Brillouin measurement has (001) plane. The EDAX and Powder XRD measurement of $PbWO_4$ shows the excess Pb in the form of $PbO_2$ impurity. But in the case of $BaWO_4$, we found the $WO_3$ impurity due to excess W in the system. Brillouin scattering measurements were carried out using 180° back scattering geometry with an incident angle of 45° with respect to surface normal. The sample was mounted in a closed–cycle Helium Cryostat (CTI Cryogenic, USA). We used a temperature controller with silicon diode sensor. Temperature stability with in ± 1 K was achieved during the measurement. Spectra have been recorded in the temperature range 320 K to 20 K. To perform Brillouin scattering, single mode vertically polarized Nd – YAG laser operated at $\lambda$ = 532 nm with 50 mW power is used as a light source. The scattered light was analyzed by using JRS Scientific instruments (3+3) pass tandem Fabry – Perot interferometer [24] equipped with a photo – avalanche diode detector which has finesse more than 100. Spectra reported in this work were recorded using a multi channel scaler with 512 channels and the typical accumulations of 500 – 2000 passes were done with 0.768 sec per pass. The line-shape parameters-peak frequency and area under the curve were extracted by a non-linear least square fitting of the data with a Lorentzian function, along with an appropriate background.

## 5.3. Theory of Elastic Constants

$PbWO_4$ and $BaWO_4$ crystallizes with the body centre tetragonal scheelite structure having space group $I4_1/a$. These compounds have four numbers of formula units per crystallographic cell at ambient condition [25]. The elastic properties depend on the orientation of the crystals. The elastic constant will give the internal properties of the crystal [26]. The velocity propagation 'v' of elastic waves in crystalline solid is given by the Cristoffel equation solution $\mathbf{( \Gamma_{jk} - \delta_{jk}\rho v^2)a_k = 0,}$ Where $\Gamma_{jk} = \frac{1}{2}\, l_i\, l_l( C_{ijkl} + C_{ijlk} )$; i,j,k,l = 1,2,3..; $\delta_{jk}$ = kronecker delta; and $l_i$ are the direction cosines of the direction of

propagation. The non–trivial solution for the above equation can be obtained, if the $| \mathbf{\Gamma_{ij} - \delta_{ij} \rho v^2} | = \mathbf{0}$ secular equation is satisfied [27]. The roots of above equation will give the velocities of different waves propagated in a particular direction with in a solid. The plane of the crystal and the elastic wave propagation direction are the two prerequisites to calculate elastic constants. With the help of back – reflection Laue x – ray photograph,

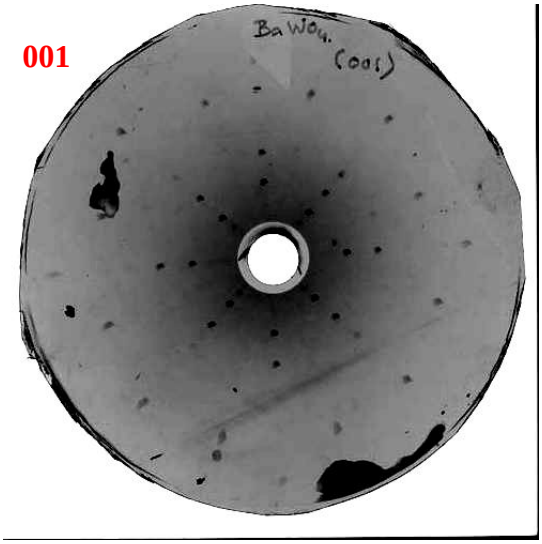


**Figure 5.1.** Laue diffraction of pattern of $BaWO_4$

the plane of $PbWO_4$ and $BaWO_4$ has been found as (001). Figure 5.1 shows the representative Laue diffraction pattern of $BaWO_4$. The frequency measurement from Brillouin shift allows the determination of the velocity propagation in the elastic waves. The frequency shift of Brillouin line is given by $\mathbf{\Delta\nu/\nu = \pm\ (V_s\ /c)\ (n_i^2 + n_s^2 - 2\ n_i\ n_s Cos\theta)^{1/2}}$ where $\Delta\nu$ - acoustic phonon frequency, $\nu$ -frequency of incident light, $V_s$ – sound velocity of scattered phonon, c – light velocity, $n_i$ , $n_s$ – incident and scattered light refractive index, $\theta$ - light scattering angle [28]. The sound velocity of the acoustic phonon is related to the elastic moduli $C_{ij}$ through $\mathbf{V_s = \sqrt{(X/\rho)}}$ where $\rho$ is the density of crystal and X is the appropriate combination of elastic constants $C_{ij}$ obtained by solving the equation of motion for a specific propagation direction. The calculation of elastic constants have been obtained for tetragonal crystal classes 4mm, 422, 42m, 4/mmm using above relation [29-31] and listed in Table 5.1 for certain direction of propagation.

**TABLE 5.1** Relation between Elastic constants and sound velocity

| Direction cosines of propagation vector | Mode | Polarization direction | Velocity | Elastic constants |
|---|---|---|---|---|
| 0,0,1 | Pure longitudinal | [001] | $\upsilon_1$ | $C_{33} = \rho\upsilon_1^2$ |
| 0,0,1 | Pure shear | [100] | $\upsilon_2$ | $C_{44} = \rho\upsilon_2^2$ |

## 5.4. Results

Figure 5.1 shows, the polarization dependent Brillouin spectra of $PbWO_4$ and $BaWO_4$ at ambient conditions. The high frequency mode at 28 GHz is a longitudinal acoustic (LA) mode, mode at 11 GHz is the transverse acoustic (TA) mode and the 14 GHz is a acoustic phonon mode due to $PbO_2$ impurity. Similarly, for $BaWO_4$, the high frequency mode at 26 GHz is LA mode and the mode at 10 GHz is TA mode of $BaWO_4$ and another sharp mode at 13 GHz is related to the $WO_3$ impurity. The Brillouin

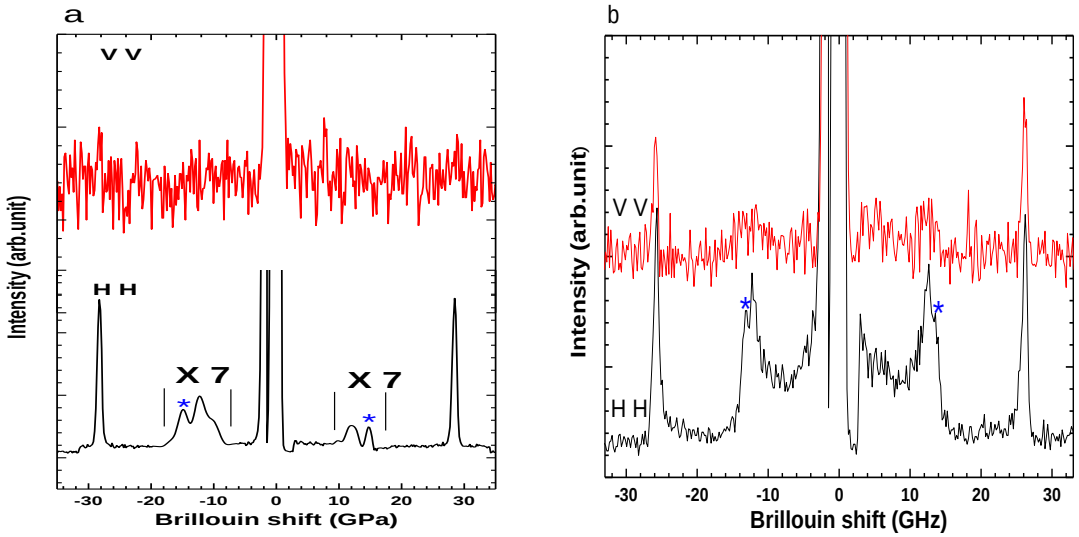


**Figure 5.2.** shows Polarization dependent Brillouin Spectra of a) $PbWO_4$ and b) $BaWO_4$ at ambient conditions. The blue color star symbol indicates the modes due to impurity for both the compounds.

spectra of $PbWO_4$ and $BaWO_4$ at different temperature are shown fig. 5.3. It is clear from the fig. 5.3. that the impurity modes ( namely 14 GHz and 13 GHz) for both $PbWO_4$ and $BaWO_4$, are not affected by the temperature.

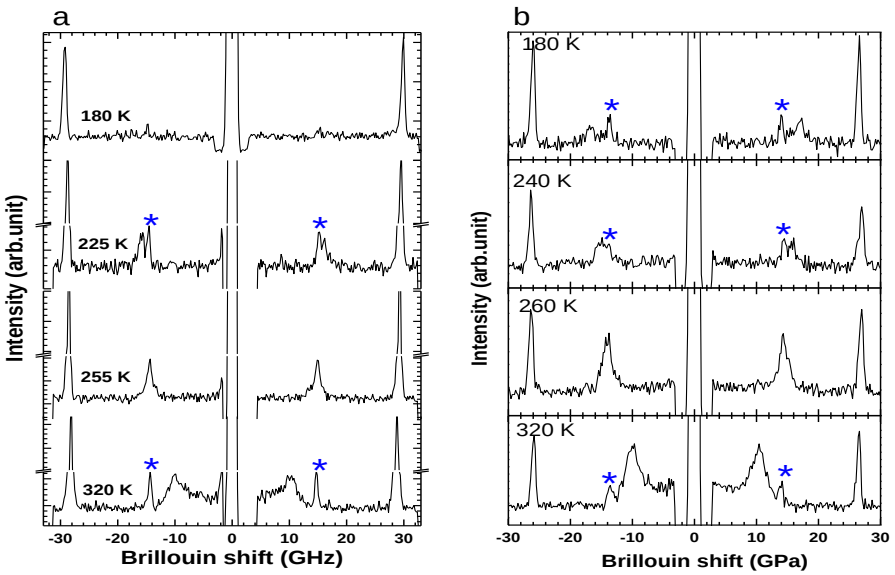


**Figure 5.3.** Shows low temperature Brillouin Spectra of a) $PbWO_4$ and b) $BaWO_4$.The blue color star symbol indicates the modes due to impurity for both the compounds.

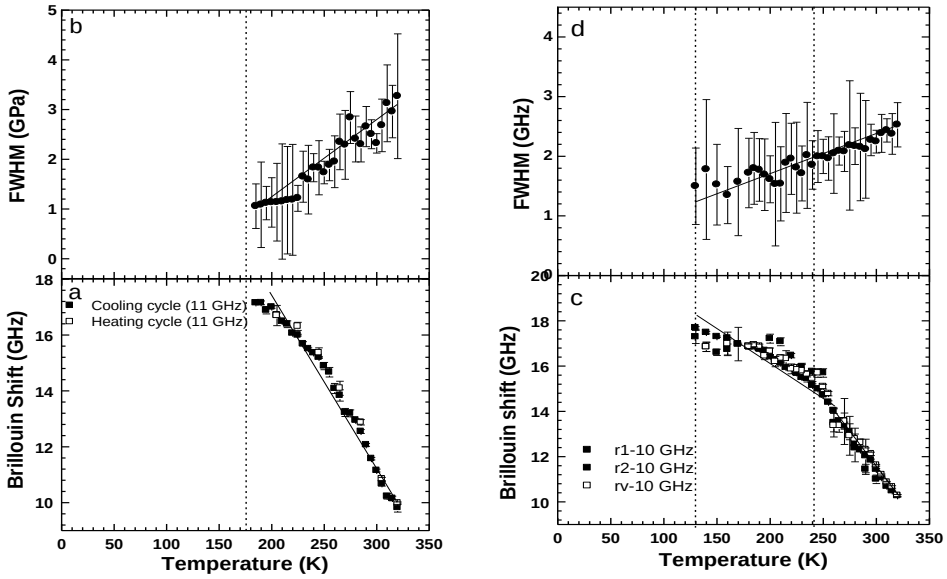


**Figure 5.4.** shows temperature dependence of the a) TA mode frequency, b) FWHM for $PbWO_4$. and c) TA mode frequency, d) FWHM for $BaWO_4$. Solid symbol represent cooling cycle and open symbol represent heating cycle. Solid line shows linear fit to the data. Vertical dotted line shows the phase transitions.

Figure 5.4 shows the temperature depence of the TA mode frequency and corresponding full width half maximum (FWHM) for both the tungstates. The TA mode frequency increases with decrease in FWHM upon lowering the temperature. It is important to note that in the case of $BaWO_4$, we observe a change in slopoe at 240 K, but no change in FWHM. It is necessary to look at the LA data and would be discussed later.

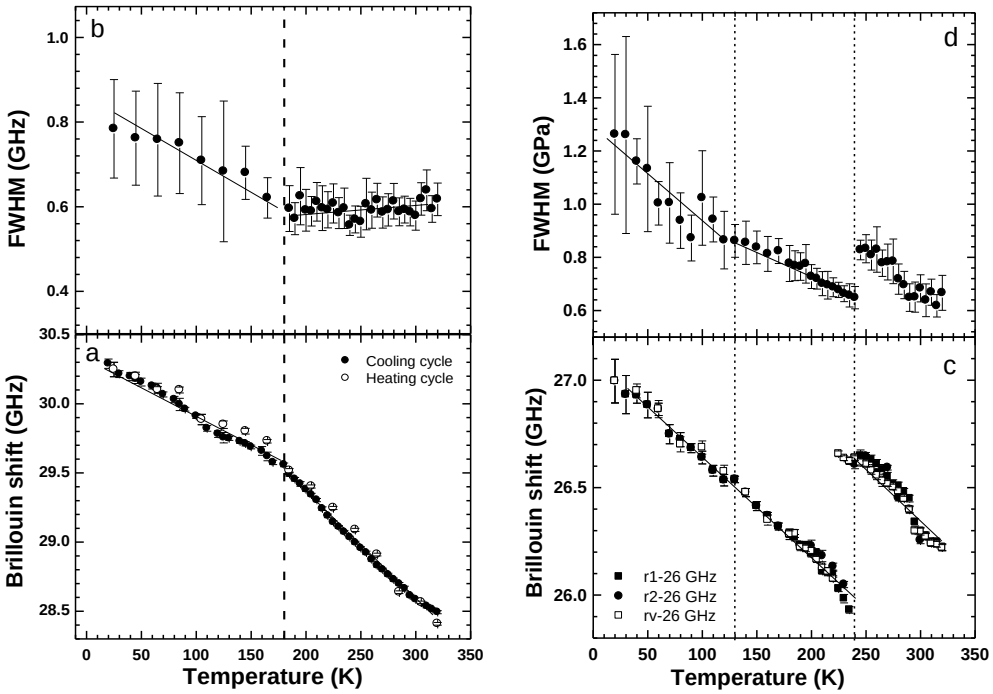


**Figure 5.5.** shows temperature dependence of the a) LA mode frequency, b) FWHM for $PbWO_4$. and c) LA mode frequency, d) FWHM for $BaWO_4$. Solid symbol represent cooling cycle and open symbol represent heating cycle. Solid line shows linear fit to the data. Vertical dotted line shows the phase transitions.

Figure 5.5 shows the temperature dependence of LA mode frequency and corresponding FWHM for both $PbWO_4$ and $BaWO_4$. in both the case the Brillouin frequency increases with decrease in temperature. But the FWHM shows anomaly. At very low temperature FWHM of LA mode increases. This is anomalous and is observed in both the cases 180 K for $PbWO_4$ and 130 K for $BaWO_4$. In the case of $BaWO_4$, we find a discontinuity around 240 K in the mode frequency. It is interesting to note that we do not observe no hystersis around 180 K or 130 K transition for the tungstates,

suggesting the transition to be second order in nature. The significance of this transition will be discussed later.

**TABLE 5.2.** The measurement of sound velocities and elastic moduli from pure LA and TA modes of $PbWO_4$.

| Displacement direction | Propagation direction | Velocity m/sec ultrasonic measuremet Ref (26) | Velocity m/sec (present work) | Elastic constants $X10^{10}$ $Nm^{-2}$ ultrasonic measuremet Ref (26) | Elastic constants $X10^{10}$ $Nm^{-2}$ (present work) |
|---|---|---|---|---|---|
| (0,0,1) | (0,0,1) | 3355 | 3472 | $C_{33}$ = 9.3 | $C_{33}$= 10.4 |
| (0,0,1) | (1,0,0) | 1732 | 1770 | $C_{44}$ = 2.5 | $C_{44}$ = 2.7 |

**TABLE 5.3.** The sound velocity and elastic constants of $BaWO_4$

| Displacement direction | Propagation direction | Velocity m/sec ($BaWO_4$) (present work) | Elastic constants for $BaWO_4$ $X10^{10}$ $Nm^{-2}$ (present work) |
|---|---|---|---|
| (0,0,1) | (0,0,1) | 3758 | $C_{33}$ = 9.1 |
| (0,0,1) | (1,0,0) | 1879 | $C_{44}$ = 2.2 |

The room temperature elastic constants for both the compounds have been calculated as discussed earler. This has good agreement with previous reports [26, 32]. The respective velocities were calculated using the expression $(532*\Delta\upsilon)/2n*Sin(\Theta/2)$ where $\Delta\upsilon$ – Brillouin shift, n – refractive index, $\Theta$ - scattering angle. The refractive index [33] of $PbWO_4$ used was 2.19 and that of $BaWO_4$ is 1.84 [34].

**5.5. Discussion**

LIU Ting-Yu etal have made theoretical calculations on the absorption spectra corresponding to the electronic transitions in $PbWO_4$ [35]. The calculated results indicate that the absorption band of the perfect $PbWO_4$ crystal does not occur in the visible region. However, the $PbWO_4$ crystal containing vacancy in the Pb site $V_{Pb}^{2-}$ has two additional absorption bands in visible region. The two bands can be well decomposed into four Gaussian-shape bands peaking at 350 nm, 405 nm, 550nm and 670 nm respectively, which coincide well with the 350 nm, 420 nm, 550 nm and 680 nm absorption bands measured in $PbWO_4$ crystals. Therefore, it can be concluded that the 350 nm, 420 nm, 550 nm and 680 nm absorption bands are related to the existence of $V_{Pb}^{2-}$ in the $PbWO_4$ crystal. Many reports have confirmed that it is difficult to get perfect crystal experimentally and the defect is more important for having absorption bands in the visible region. This is true in our case too. We observed $PbO_2$ impurities in $PbWO_4$ and $WO_3$ impurity $BaWO_4$. The temperature dependent Raman studies tungstates show no changes in the internal modes ($WO_4$) but they do see some softening of the external mode [36]. Since acoustic phonons are long wavelength phonons unlike Raman vibrations, they are influenced by the network of atoms. Hence presence of impurity as well as the change of environment around the impurity would greatly modulate the acoustic phonons, hence we expect Brillouin spectra to be effected by the impurity.

In order to understand the differences in the behavior of $BaWO_4$ and $PbWO_4$ at relatively higher temperature, let us look at the polarize spectra of these tungstate shown in figure 5.2. The polarization spectra of $PbWO_4$ in figure 5.2 (a) show all the modes disappear with crossed polarization which is expected. But in the case of $BaWO_4$, the LA mode persist in crossed polarization in figure 5.2.(b) this suggests that there is a contribution from the excess $WO_3$ imprity to the LA mode. As one lowers the temperature one would find the difference in the temperature dependence of the LA modes due to the bulk and impurity. This is the reason for the 240 K transition in $BaWO_4$. Correspondingly we observe an influence on TA mode as well. Beyond 240 K the behavior of $BaWO_4$ and $PbWO_4$ are similar, hence we expect the reason to be same for the low temperature transition. As one lowers the temperature, the volume contracts around the vacancy we would observe large rearrangement. The disappearance of TA

mode signifies that there the crystal tends towards an isotropic solid. This is also associated with a slight increase in the FWHM of LA mode in both the cases. It is important to note that the increase in FWHM means a change in life time of the phonon. Since the vacancies are getting modulated, the electronic contribution are also getting modulated. Since LA mode is influence by the vacancies, there is an increase in electron-phonon coupling of the LA mode, leading to increase in lifetime and hence FWHM.

Such a transition is not structural in nature which is corroborated by the fact that the transition is reversible without hystersis. These results emphasis the need to look at the vacancies in cation sites and their implication on the applications of the materials. According to figure 5.2 (a-b) shows that the acoustic modes for $PbWO_4$ and $BaWO_4$ changes with lowering temperature but the modes due to impurities for both the compounds do not see any changes with temperature. This has been marked with blue color star symbol in the spectra. The increase in TA mode as well as their decrease in FWHM with lowering temperature in figure 5.3 (i (a-b) & ii (a-b)) shows stiffening of the bonds as well as the reduction of average spread in spring constant for both the compounds. These modes seize to exist below 180 K and 130 K for $PbWO_4$ and $BaWO_4$ respectively. This could be due to contraction of $WO_4$ bonds with low temperature for both compounds. According to LA mode behavior of $PbWO_4$ with temperature in figure 5.4(i-a), the mode frequency hardens with low temperature but around 180 K there is a change in slope. The behavior of FWHM with temperature in figure 5.4 (i-b) shows increase in line width below 180 K which is an anomalous behavior, this could be related to changes in environment around Lead vacancy ($V_{Pb}^{2-}$) due to contraction of the system with low temperature. This involves changes in electronic states. Since acoustic modes involve whole lattice vibration, there is a strong coupling between electronic states and phonon states. This reflects the change in phonon life time below 180 K. But in the case of $BaWO_4$, the hardening of frequency as well as increase in FWHM with lowering temperature in figure 5.4(ii (a-b)) could be related to decrease in penetration depth as a result conductivity increases. So the $WO_3$ impurity becomes more metallic. The sudden discontinuity at 240 K could be related to disappearance of $WO_3$ impurity in the system. This phase transition is insensitive for x-ray because Brilouin spectroscopy has high resolution as compared to x-ray. The change in slope of increase in FWHM at 130 K

could be related to changes in environment around tungsten vacancy. This is related to changes in electronic states in the system. Due to strong electron-phonon coupling, these changes reflect in acoustic phonon modes with low temperature. As a result, there is an anomalous behavior in FWHM with low temperature. This electronic phase transition could be same as that of $PbWO_4$. The reversibility of these modes clearly shows that this phase transition is second order transition. This shows that there is no structural transition for both the compounds.

### 5.6. Conclusion

In conclusion, we observe temperature induced phase transition for $PbWO_4$ and $BaWO_4$ using Brillouin scattering. The phase transition in these tungstates is due to changes in the environment around the cation vacancy Pb in the case of $PbWO_4$ and W in $BaWO_4$. The vacancy cannot be avoided in these crystals and are responsible for the presence of absorption in the visible range. The acoustic modes are linked with these electronic levels and hence show a strong electron-phonon interaction upon modulation of these impurities with temperature. There is an increase of life time of the phonon due to this. The transition is second order in nature and is observed at 130 K for $BaWO_4$ and 180 K for $PbWO_4$. The 240 K transition in $BaWO_4$ is due to $WO_3$ precipitation and since their contribution is minimal to the Brillouin spectra, One can study these systems in the presence of these impurities. It would be interesting to carry out temperature dependent absorption studies of these materials to see the effect of strong electron-phonon interaction.

### 5.7. Bibliography


1. Compact Muon Solenoid (CMS), Technical Proposal, CERN/LHC 93-98, 1994, P. 1.
2. Kobayashi. M; Ishi. M; Usuki. Y; Yahagi. H; Nucl. Instrum. Methods Phys. Res. A **333**, 429 (1993).
3. D. Errandonea, J. Pellicer-Porres, F. J. Manjan, A. Segura, Ch. Ferrer-Roca, R. S. Kumar, O. Tschauner, P. Rodriguez-Hernandez, J. Lopez-Solano, S. Radescu, A. Mujica, A. Munoz, G. Aquilanti. **72**, 174106 (2005).

4. S. P. S. Porto and J. F. Scott, Phys Rev **157,** 716 (1967).
5. Nicol,Malcolm; Durana,Jean F. J. Chem. Phys. **54**, 1436 (1971).
6. Ge,W.W.; Zhang,H.J.; Wang,J.Y.; Liu,J.H.; Xu,X.G.; Hu,X.B.; Jiang,M.H.; Ran,D.G.; Sun,S.Q.; Xia,H.R.; Boughton,R.I. J. Appl.Phys. **98**, 013542 (2005).
7. Gurmen,Erdogan; Daniels,Eugene; King,J.S. J. Chem. Phys. **55**, 1093 (1971).
8. Zalkin,Allan; Templeton,David H. J. Chem. Phys. **40**, 501 (1964).
9. Sawaguchi,Etsuro; Akishige,Yukikuni; Kobayashi,Masakazu. J. Phy. Soc. Jpn. **54**, 480 (1985).
10. Yamaguchi,Hirotaka; Yamada,Atsuo; Uwe,Hiromoto; Sakudo,Tunetaro. Phys.Rev. B. **43**, 4473 (1991).
11. Bell,R.O.; Rupprecht,G. Phys. Rev. **129**, 90 (1963).
12. Hirotaka Yamaguchi, Hiromoto Uwe, Tunetaro Sakudo and Etsuro Sawaguchi. J. Phy. Soc. Jpn. **57**, 147 (1988).
13. Sawada,Akikatsu; Udagawa,Masayuki; Nakamura,Terutaro. Phys. Rev. Lett. **39**, 829 (1977).
14. Keve,E.T.; Abrahams,S.C.; Bernstein,J.L. J. Chem. Phys. **54**, 3185 (1971).
15. Ganguly,B.N.; Ullman,F.G.; Kirby,R.D.; Hardy,J.R. Sol. Stat. Comm. **17**, 533 (1975).
16. V. Dvořák. Phys.Stat. Sol. (b). **46**, 763 (1971).
17. Robert M. Hazen, Larry W. Finger and Joseph W. E. Mariathasan. J. Phys. Chem.Solids. **46**, 253 (1985).
18. Depero,Laura E.; Sangaletti,Luigi; J. Solid. Stat. Chem. **129**, 82 (1997).
19. Zundu. L; Yindong. H; J. Phys. Condens. Matter. **6**, 3737 (1994).
20. Depero,Laura E.; Sangaletti,Luigi; J. Solid. Stat. Chem. **129**, 82 (1997).
21. M. Maczka, F. Jiang, S. Kojima and J. Hanuza. J. Mol. Struct. **563-564**, 365 (2001).
22. Kasprowicz,D.; Runka,T.; Szybowicz,M.; Drozdowski,M.; Majchrowski,A.; Michalski,E.; Zmija,J; J. Mol. Struct. **792-793**, 139 (2006).
23. Jayaraman A; Batlogg B; VanUitert L.G; Phys. Rev. B. **31**, 5423 (1985).
24. Lindsay S. M; Anderson M.W; Sandercock J.R; Rev. Sci. Instrum. **52**, 1478 (1981).

25. Gurmen,Erdogan; Daniels,Eugene; King,J.S. J. Chem. Phys. **55**, 1093 (1971).

26. Khatkevich A. G; Sov. Phys. Crystallogr. **6**, 561 (1962).

27. Gluyas,M.; Hughes,F.D.; James,B.W. J. Phys. D: Appl. Phys. **6**, 2025 (1973).

28. M. H. Grimditch and G.D. Holah, Phys. Rev. B, **12**, 4377 (1975).

29. Kobelev N. P; Soífer; Phys. Solid. Stat. **38**, 1956 (1996).

30. Farley,J.M.; Saunders,G.A. J. Phys. C: Solid State Phys. **5**, 3021 (1972).

31. Auld B. A; Acoustic fields and waves in solids, V-1, (1973).

32. Coquin,G.A.; Pinnow,D.A.; Warner,A.W. 42, 2162 (1971).

33. Lide D.R (ed.); CRC Handbook of Chemistry and Physics (CRC, 1990).

34. T. T. Basiev, A. V. Gavrilov, V. V. Osiko, S.N. Smetanin, A. V. Fedin. Quantum Electronics, **34**, 649 (2004).

35. LIU Ting-Yu; ZHANG Qi-Ren; ZHUANG Song-Lin; Chin.Phys.Lett. **22,** 442, (2005)

36. Jun SUDA; Tsutomu SATO; J. Phys. Soc. Japan, **66**, 1707, 1997.

# CHAPTER - VI

# Temperature dependent Brillouin scattering studies of $AgGaS_2$

**This chapter constitutes the work will be published in**

**G. Kavitha and Chandrabhas Narayana Physical Review B (submitted) 2008.**

## 6.1. Motivation

The silver thiogallate, $AgGaS_2$, crystallizes in the chalcopyrite structure, and belongs to I-III-$VI_2$ group of compounds. These have a very large nonlinear optical coefficient making them interesting non linear optical materials. These are also direct band gap materials with a band gap of 2.75 eV (blue) and have similar properties as the binary II-VI compounds with cubic sphalerite (zinc blende) structure [1]. Such materials are technologically important as they posses large linear coefficients and have properties such as wide transparency range, fast response and high damage threshold. Non-linear optic materials typically have a distinct crystal structure, which anisotropic with respect to electromagnetic radiation. However, being a ternary compounds having a non-cubic structure widens the possible range of application in the solar cell, light emitting diode (LED) [2]. In addition, the chalcopyrites, being uniaxial have birefringence and hence allow phase matching possibilities which are not available in isotropic GaAs. This compound has been used to generate tunable radiation from 4.6 to 12 μm [3]. $AgGaS_2$ has been phase-matched for second harmonic generation at 10.6 μm using a $CO_2$ laser. The non-linear devices for which silver thiogallate may be useful include optical parametric oscillators; sum and difference mixing of a fixed wave length laser. The difference mixing using a $CO_2$ laser and the spin-flip Raman laser should have a range which essentially covers the whole spectral region from zero wave number to a wave number determined by excessive lattice vibrational absorption. In practice a useful range could be from 100μm - 1000μm [4]. Due to the interesting applications and other inherent properties of these materials, it is essential to understand the temperature stability of the physical properties of $AgGaS_2$. Earlier temperature dependent x-ray studies did not reveal any changes in the lattice parameter [5], eventhough the reflectance studies showed changes in the bandgap at low temperature [6]. The advantage of Brillouin studies is that along with acoustic phonon studies, it can be used to study optical constants of the material. We have carried out Brillouin scattering studies on $AgGaS_2$ in the temperature range 20K to 300K. We observe a strong electron-phonon coupling between the acoustic modes which modulates the acoustic mode frequency 10 to 15%.

## 6.2. Chalcopyrite crystal structure

The semiconducting I-III-$VI_2$ compounds are isoelectronic with zinc blende II-VI compounds. They can be considered as mixed crystals where each divalent cation of the zinc blende structure is replaced alternatively by monovalent and trivalent cations. It has nearly the same arrangements of anions but differs in the ordered distribution of the cations which makes the unit cell tetragonal. The body-centered tetragonal structure of $AgGaS_2$, primitive cell contains two formula units with space group I42d. By doubling zinc blende unit cube along the z-axis, we derive the chalcopyrite structure where elongated z-axis becomes the c-axis [7]. In a chalcopyrite structure the c/a ratio should be equal to two [8]. But in most real chalcopyrite structure like $AgGaS_2$, the c/a ratio is less than two, since the structural correlation is not perfect and usually has slight tetragonal distortion. Most often, there is a compression along the c-axis, i.e., $2\text{-}c/a \geq 0$. For $AgGaS_2$ it is 0.2104 [9].

$AgGaS_2$ is a pale yellow color transparent crystals, and stable at ambient conditions. It transmits radiation in the wavelength region 0.5μm to 13μm. The refractive indices have been measured by sellmeir's equations, [1]

$$\mathbf{n_o^2 = 5.728 + 0.2410/(\lambda^2 - 0.0870) - 0.00210\lambda^2}$$

$$\mathbf{n_e^2 = 5.497 + 0.2026/(\lambda^2 - 0.1307) - 0.00233\lambda^2}$$

where the wavelength is expressed in μm. we have calculated this for the excitation source, namely, Nd-YAG laser of wavelength 0.532 μm. The calculated values of $n_0$ = 2.6375, $n_e$ = 2.6127 have good agreement with earler report [7].

## 6.3. Experimental details

Brillouin spectra were recorded in 180° - back scattering geometry with an incident angle of 45° with respect to the surface normal. The scattered light was analyzed with polarization using a selective JRS scientific instruments (3+3) pass tandem Fabry – Perot interferometer equipped with a photo-avalanche diode detector which has finesse greater than 100. The tandem Fabry-Perot [10] interferometer was used to record the spectra. Spectra presented in this work were recorded using a multi channel scalar with 512 channels and the typical accumulations times of 1000-10,000 passes with 0.768 sec

per pass. Temperature dependant measurements were carried out inside a closed cycle Helium cryostat (CTI Cryogenic, USA). The sample temperatures were measured with in an accuracy of ± 1K. The incident laser power was kept at 50 mW focused to a diameter of ~ 30 μm. The laser heating of the sample was found to be 20K, by measuring the intensity ratio of the Stokes and anti Stokes Raman lines which has been corrected in plotting the data. All the spectra are normalized with room temperature spectra for ease of comparison. The line shape parameters, namely, peak frequency, full-width at half maximum (FWHM) and area under the curve were extracted by non-linear least square fitting of the data with a lorentzian function with an appropriate baseline.

### 6.4. Elastic constants of chalcopyrite

In a Brillouin experiment one measures the frequency associated with an acoustic phonons. Using this ands with the knowledge of refractive index and the wave vector, one can determine the velocity of elastic waves which helps in determination of the elastic constants of the crystal. We would restrict ourselves to only the important relations here. The frequency shift of a Brillouin line is given by [7]

$$\Delta\nu/\nu = \pm\ (V_s/c)\,(n_i^2 + n_s^2 - 2\,n_i\,n_s\cos\theta)^{1/2}$$

where $\Delta\nu$ is the frequency shift of the Brillouin line, $\nu$ is the frequency of the incident light. $V_s$ is the sound velocity of phonon responsible for the scattering, c is the velocity of light; $n_i$ and $n_s$ the refractive indices for the incident and scattered light respectively and $\theta$ is the angle through which the light is scattered. The velocity of the acoustic phonon is related to elastic moduli $C_{ij}$ through $\mathbf{V_s = \sqrt{(X/\rho)}}$ where $\rho$ is the density of the sample and X is an appropriate combination of elastic constants obtained by solving equation of motion for a specific propagation direction [7, 11]. In the case of $AgGaS_2$ we are having the crystal cleaved along (111) plane, containing crystallographic direction [001] and [110]. We can elucidate three elastic constants using the following relations:

$$\mathbf{V^2 = C_{44} / \rho} \qquad \mathbf{(6.1)}$$

$$\mathbf{V^2 = C_{44} / \rho A} \qquad \mathbf{(6.2)}$$

$$\mathbf{V^2 = (3C_{11}+4C_{44}\,((A-1)/A)) / 3\rho} \qquad \mathbf{(6.3)}$$

where $\mathbf{A = 2C_{44}/ (C_{11}-C_{12})}$ is the anisotropy factor. The Cristoffel equations for isotropic and anisotropic tetragonal solids of symmetry 4mm, 422, -42m, 4/mmm are same as hexagonal crystals but with an arbitary $C_{66}$ [12].

## 6.5. Results

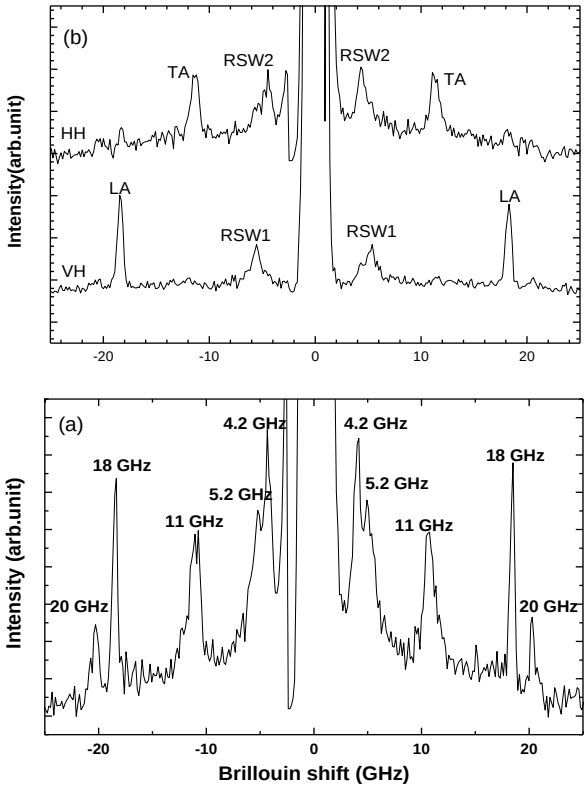


**Figure 6.1**. shows the a) unpolarized and b) polarized Brillouin spectrum of $AgGaS_2$ at ambient conditions. The H and V in (b) means horizontal and vertical polarization with respect to the scattering plane.

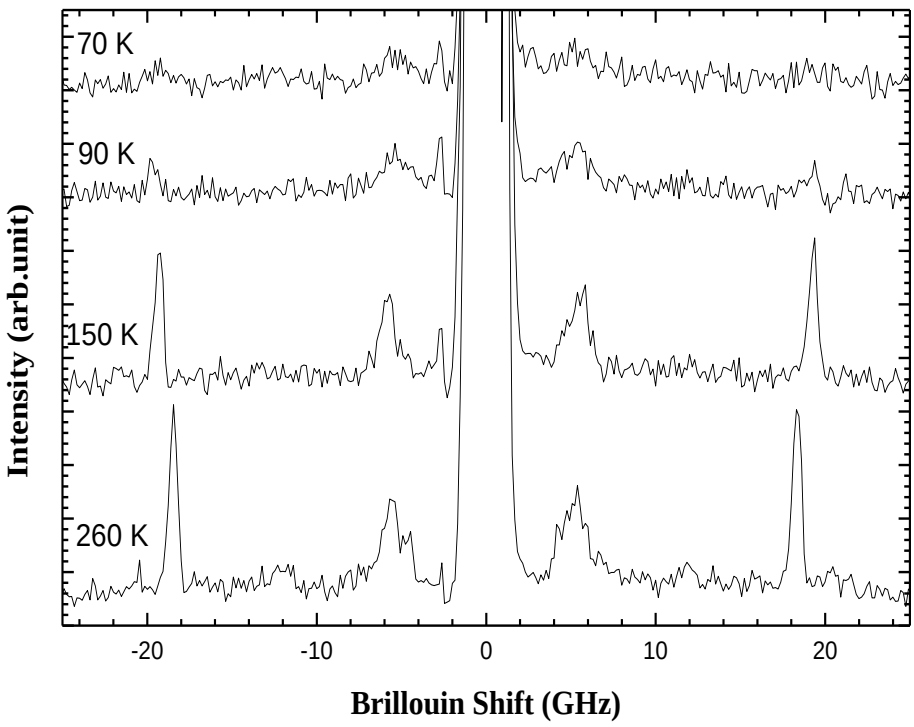


**Figure 6.2.** shows the one of the polarized Brillouin Spectrum at different temperatures

Figure 6.1(a&b) shows the unpolarized and polarized Brillouin spectra of $AgGaS_2$ at ambient conditions. The two spectra shown in fig 1(b) has different modes depending on the polarization. For crossed polarization (VH) the two modes are around 5.4, 18 GHz, labeled as RSW1, LA (longitudinal) modes and for parallel polarization (HH), we see the modes are around 4.5, 11 GHz labelled as RSW2, TA (transverse acoustic). Figure 6.2 shows representative temperature dependent Brillouin spectra for VH polarization. The line width of all the modes increases with lowering of temperature. This is an anomalous behavior and would be discussed later.

We now try to estimate the sound velocities for the surface modes. The component of the wave vector parallel to the surface is given by $\mathbf{q_{||} = (4\pi/\lambda)\ Sin\ \theta}$ [13]**.** The dispersion of RSW is shown in fig 6.3 using the relationship $\mathbf{2\pi\nu_R = V_R\ q_{||}}$. We deduce $V_R$ =2120 m $sec^{-1}$ for RSW1 mode and $V_R$ = 3603 m $sec^{-1}$ for RSW2 mode. In the case of LA and TA mode we have calculated the velocities for a particular q for $\theta = 45°$ $V_{LA}$ = 3689 $msec^{-1}$, $V_{TA}$ = 2451 $msec^{-1}$. Using the sound velocities one can calculate the

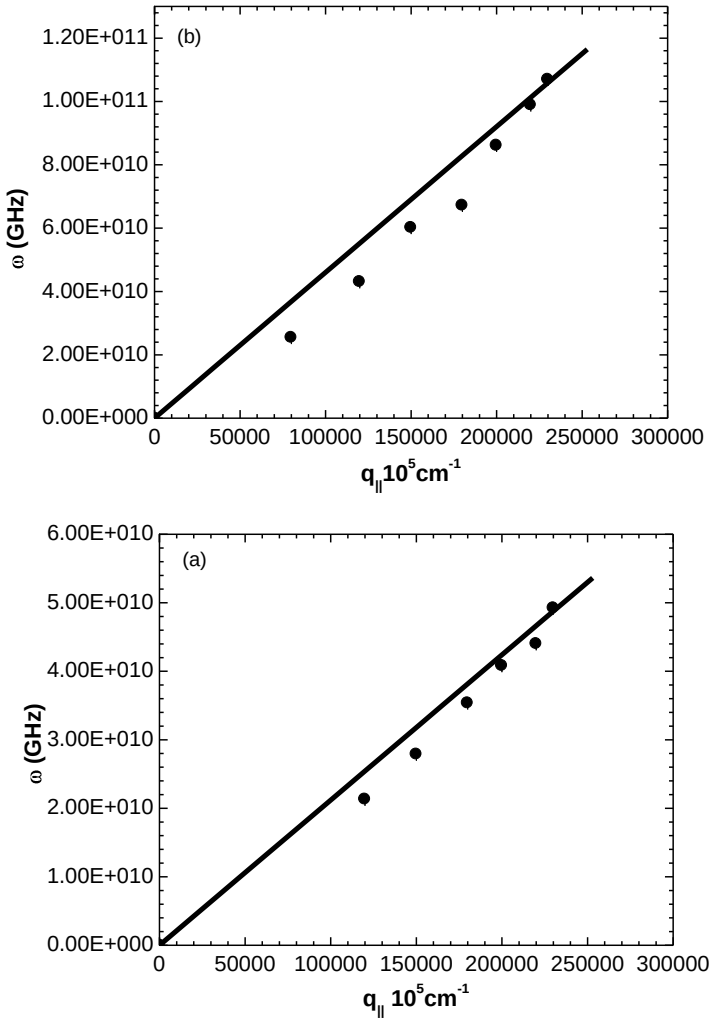


**Figure 6.3.** shows the dependence of RSW mode frequency ($\nu_R$) as a function of $q_{||}$. The solid line is a linear fit to $\mathbf{2\pi\nu_R = V_R\, q_{||}}$ which gives a) $V_R$ =2120 m sec$^{-1}$ for RSW1 mode and b) $V_R$ = 3603 m sec$^{-1}$ for RSW2 mode.

elastic constants for the different modes using the relation described in the section 6.4. Table 6.1 show the calculated elastic constants for $AgGaS_2$ and have been compared with earlier report [8]. It is in good agreement.

**TABLE 6.1.** Comparison of Elastic moduli of silver thiogallate (units are in$10^{10}$ N/m$^2$):

| Elastic moduli | $AgGaS_2$ (Ref.8) | $AgGaS_2$ (our data) |
|---|---|---|
| $C_{11}$ | 8.79 | 8.696 |
| $C_{12}$ | 5.84 | 3.073 |
| $C_{44}$ | 2.41 | 2.112 |

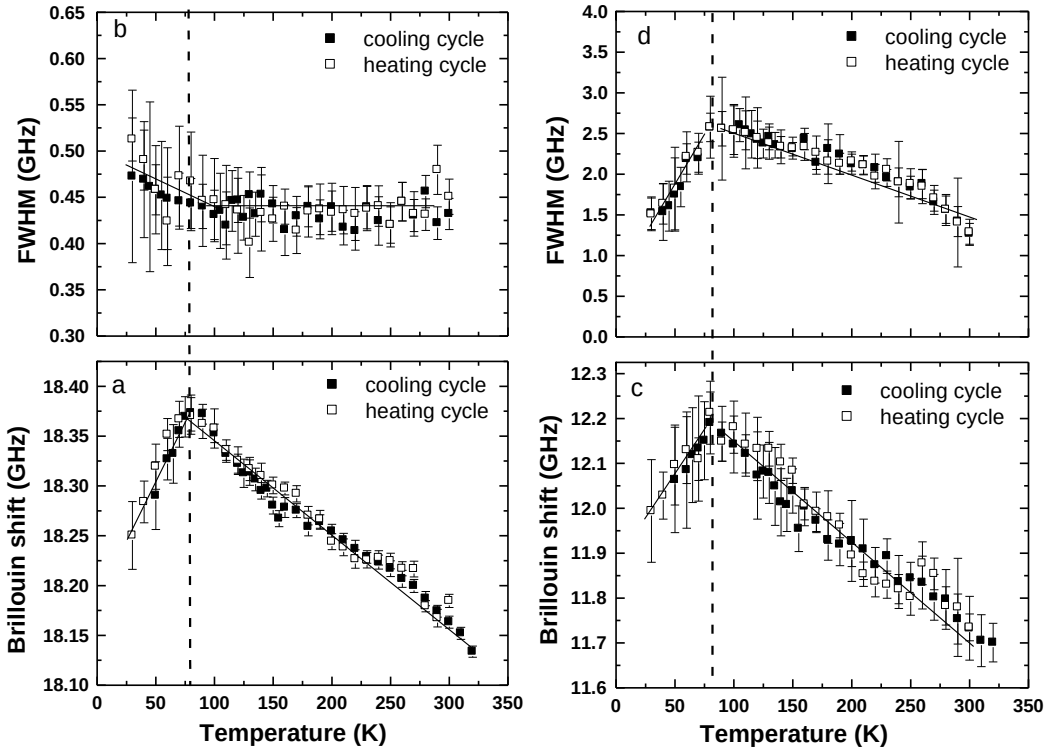


**Figure 6.4.** shows the temperature dependent behavior of (a) LA mode frequency, (b) its FWHM and (c) TA mode frequency and (d) its FWHM. Vertical dotted line shows the phase transition temperature. Solid symbol and open symbol represent the cooling and heating cycle respectively.

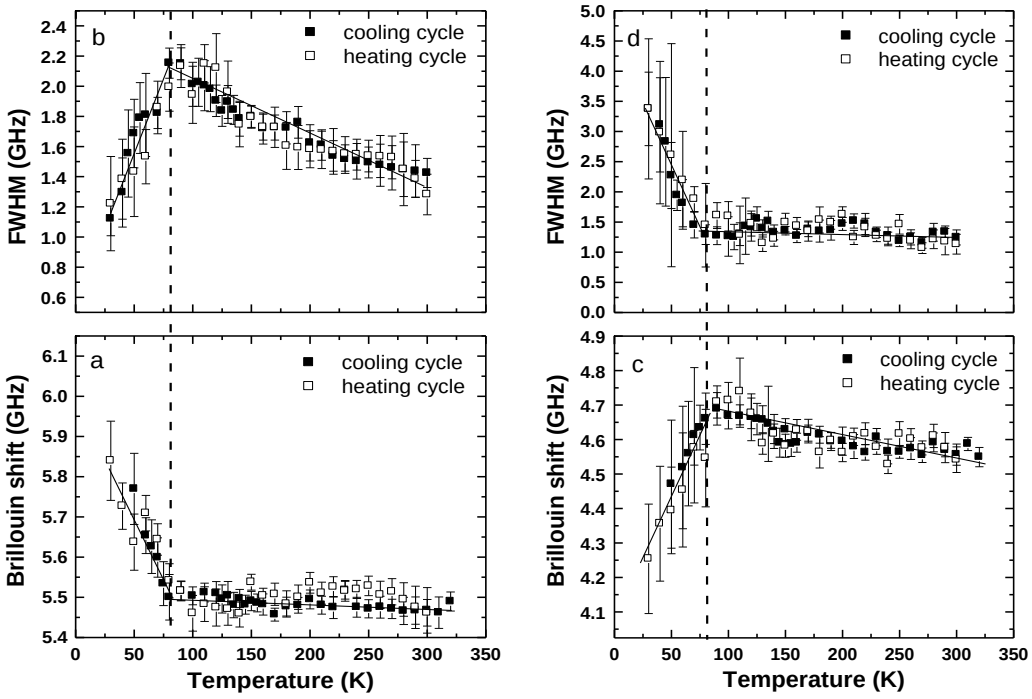


**Figure 6.5.** shows the temperature dependent behavior of (a) RSW1 mode frequency, (b) its FWHM, (c) RSW2 mode frequency, (d) its FWHM. Vertical dotted line shows the phase transition temperature. Solid symbol and open symbol represent the cooling and heating cycle respectively.

Figure 6.4 shows the temperature dependence of LA&TA mode frequency and FWHM. Both the mode frequencies show changes in mode behavior below 80 K, this an onset of a phase transition. This is accompanied with changes in FWHM or life time of the phonon. Similar observation is made in the case of RSW modes at the same temperature of 80 K which is shown in fig 6.5. This confirms that there is a phase transition at 80 K for $AgGaS_2$ . Since there is no hysteresis across this transition as seen from cooling and heating cycles, we expect this transition to be second order in nature.

### 6.6. Discussion

From the Fig. 1(b), we observe that LA and RSW1 are of similar symmetry and TA and RSW2 are of similar symmetry. This is due to the fact that they appear in similar polarizations. Now let us look at other experimental observation at 80 K. In the x-ray studies it is observed that the lattice constants **a** and **c** show a different behavior as a function of temperature [5, 14, 15]. Reflectivity studies show that the band gap of $AgGaS_2$ changes from direct to indirect bandgap below 80 K [16]. There are two reasons for this:

1. The thermal expansion effect, or what is often called as dilation contribution, accounts for the effect of the change of lattice constant on the energy gaps. This is expected since the electronic energy bands are formed because of the "over lappings" of electronic wave function, the extent of which is dependent upon the distances between neighboring atoms (ion) [16].
2. The major contribution however comes from electron-phonon interactions. The one-electron theory of electronic energy bands of a crystalline solid is based on the assumption that the crystal is perfect which is true only at absolute-zero degree temperatures. At finite temperatures, the energy of the electron is subject to change because of the interaction between electrons and phonons. This is reflected in the change of energy gap with temperature [16].

When we have an indirect band gap material there is a need of phonon for strong electron-phonon interaction. It is not necessary for all the phonons to couple with electronic states in an indirect band gap material, or couple in the same way. It is seen that LA, TA and RSW1 soften below 80 K with a corresponding increase in FWHM or life time of the phonon. When a strong electron-phonon coupling happens there is a strong interaction between electronic states and the phonon states, opening up a lot of channels for energy transfer. This increases the life time of the phonon and leads to an increase in FWHM, along side the phonon energy shifts to lower energy resulting in softening of the phonon. Hence we suggest that both the acoustic modes (LA&TA) including RSW1 are strongly coupled to the electronic states.

The difference in behavior of RSW2 is partly due to the fact that RSW2 is in different symmetry and does not couple with these electronic states, but would couple

with other states. The luminescence and absorption experiments [17-19] also support the electronic nature of 80 K transition.

### 6.7. Conclusion

In conclusion, the temperature dependent Brillouin studies on $AgGaS_2$ have been carried out. The direct – indirect band gap transition occurs below 80 K. There is a strong electron-phonon coupling between acoustic modes (LA&TA) and is seen from the anomalous behavior below 80 K. The electronic transition namely direct to indirect band gap is involving the lattice modes. The second order nature is due to lack of hysteresis which supports this picture.

### 6.8. Bibliography


[1]. D. S. Chemla, P. J. Kupecek, D.S. Robertson and R. C. Smith Opt. Commun. 3, 29 (1971).

[2]. J. Lazewski and K. Parlinski, J. Chem.Phys. 114, 6734 (2001)

[3]. D. C. Hanna, V. V. Rampal and R. C. Smith, Opt. Commun. 8, 151 (1973)

[4]. G. D. Holah Opt. Commun. 5, 10 (1972)

[5]. P. Kistaiah, Y. C. Venudhar, K. Sathya Narayana Murthy, Leela Iyengar and K. V. Krishna Rao, J. Mat. Sci, 16, 1417 (1980).

[6]. L. Artus and Y. Bertrand, solid. stat. Commun. 61, 733 (1987).

[7]. M. H. Grimditch and G.D. Holah, Phys. Rev. B, 12, 4377 (1975).

[8]. R. Asokamani, R. M. Amirthakumari, R. Rita and C. Ravi, Phy.stat.sol. (b), 213, 349 (1999).

[9]. S. C. Abrahams and J.L. Bernstein, J. Chem. Phys, 59, 1625 (1973).

[10]. Lindsay S. M; Anderson M.W; Sandercock J.R; Rev. Sci. Instrum. 52, 1478 (1981).

[11]. N. S. Orlova, Cryst. Res. Technol. 33, 87 (1998).

[12]. B. A. Auld, Acoustic fields and waves in solids, V-1, (1973).

[13]. Md. Motin Seikh, Chandrabhas Narayana, P. A. Metcalf, J. M. Honig, and A. K. Sood, Phys. Rev. B, 71, 174106, (2005).

[14]. P. Kistaiah, Y. C. venudhar, K. Sathya narayana murthy, Leela Iyengar and K. V. Krishna Rao, J. Phys. D: Appl. Phys. 14, 1311 (1981).

[15]. J. L. Shay, B. Tll, H. M. Kasper and L. M. Schiavone, Phys. Rev. B. 5, (1972).

[16]. Y. F. Tsay, B. Gong and S. S. Mitra, Phys. Rev. B, 6, 2330 (1972).

[17]. B. Tell and H.M. Kasper, Phys. Rev. B, 4, 4455 (1971).

[18]. G. Branelt, A. Rauber and J.Schneider, Solid.State. Commun, 12, 481 (1973).

[19]. B. Tell and J. L. Shay, Phys. Rev. B, 6, 3008 (1972).